Memoirs of the Faculty of Engineering, Nagoya University
Vol. 34, No. 1 (1982)

EFFECTS OF CONMPLICATED DEFORMATION HISTORY ON INELASTIC DEFORMATION BEHAVIOUR OF METALS

YOSHIO OHASHI

Department of Mechanical Engineering

(Received May 1, 1982)

Abstract

Since the main difficulty to solve non-linear differential equation has been eliminated with the provide of electronic computer, present attentions in performing precise inelastic deformation analysis of engineering structures are concentrated to establish constitutive equations with an accuracy suitable to that obtainable in the electronic computer.

The essentials in establishing the constitutive equations consist in the precise control of the optionally assigned system of combined loading or deformation applied to specimen and the precise measurement of the corresponding deformation or resistance, and the systematic description of the variation of deformation behaviours due to the effect of deformation history. Formerly, experimental results of this kind have been expressed in a form of empirical formula in which the history effect is not always reflected clearly. However, the necessary and sufficient conditions have been settled for the constitutive equation, and the method has been proposed to consider clearly the history effect in the equation, in the continuum mechanics.

In our laboratory, investigations to establish the constitutive equation in reflecting the history effects from the theoretical view point in the continunm mechanics have been developed since more than ten years ago, in accordance with the experimental results of plastic deformation behaviours of various metals under combined loadings or deformations obtained by using an automatic combined loading testing machine. The present paper summarizes the early results of the investigation.

CONTENTS

Chapter Ⅰ Introduction

Accurate analysis of inelastic deformation of metallic structures becomes more necessarily with the increasing severity in the condition under which structures are used. It has also a significant meaning to find more efficient and precise process of plastic working. For this purpose, it is necessary first of all to observe precisely the deformation behaviour of engineering materials under complicated loading systems, and to formulate the constitutive equation of the materials so as to express the results of observation as precisely as possible.

Complicated nonlinear phenomena accompanying the history effects due to the change of micro-structure in the material appear in the inelastic deformation of

real materials, and thus it has been very difficult to take into account these behaviours properly in the mathematical analysis of inelastic deformation.

However, these history effects in the inelastic behaviour described in the form of stress-strain curve have been regarded as the secondary ones. Thus, to avoid the difficulties mentioned above, an elegant "plastic flow theory" which is convenient for mathematical analysis has been formulated by neglecting the complicated history effect appearing in real materials, and used to solve engineering problems in a wide range. However, this simplified theory is able to approximate only a part of plastic behaviour of real materials and is found as insufficient to approximate the deformation behaviour of metals under complicated loading system. For this reason, various investigations[1~7] have been conducted to modify this theory so as to reflect the history effects. However, many problems are left unsolved theoretically and practically as well.

Nowaday, precise observation of deformation behaviour accompanying complicated history effect may be performed easily by using a full-automatic testing machine, and thus even the effect of tensorially nonlinear term in the stress-strain relation can be discussed experimentally. However, it is difficult to take into account such a nonlinear effect in the flow theory.

Since most of the difficulties in mathematical analysis have been eliminated by the introduction of electronic computer, it may be said that the accuracy in the result of deformation analysis depends mainly on the approximation in formulating the results of precise observation of deformation behaviour of real materials under complex loading systems.

In the field of continuum mechanics, a general form of constitutive equation has been constructed in terms of functionals concerning characteristics of deformation behaviour which the materials obtain by the history effect.[8] The general plastic theory in a five-dimensional vector space corresponding to the stress or strain deviator, proposed by Ilyushin[9] in formulating the plastic behaviour of metals under complex loading, also belongs in this category, and his "postulate of isotropy" and "principle of delay" seem to be useful approximations to simplify the infinite varieties of history effect. His theory has been discussed experimentally by Lensky,[10] who verified the validity of this theory for some metals under certain comlex loading systems. However, as Ivlev[11] and Novozhilov[12] have pointed out, the vector space used by Ilyushin cannot reflect explicitly some of the characteristics in the tensor space.

At present, the constitutive equation of metals under inelastic deformation are considered in more detail by taking account of a change in the micro-structure of metals due to deformation. A kind of constitutive equation is established in terms of the internal state variables together with the equation showing their evolution in the view point of irreversible thermodynamics.[13] Another kind of constitutive equation is constructed by taking into account an interaction between slip-systems in every crystal grain and the microscopic residual stress as well.[14]

As mentioned above, the investigation to clarify the inelastic deformation behaviour of metals under complicated loading system becomes more intensive in these days. Under such situations, a full-automatic complex-loading testing machine with high accuracy was constructed in our laboratory (1970) for measuring precisely the plastic behaviour of metals under combined loading at room temperature.[15] The same kind of apparatus also established two years later for measuring the inelastic behaviour of metals at elevated temperature. Ever since,

these equipments have been used to observe the inelastic behaviour of metals under some fundamental patterns of complex deformation history.

The present paper collects briefly the results of investigations performed at room temperature, concerning the history effects on the inelastic behaviour of metals under complex loading system.

Chapter Ⅱ Experimental Apparatus

2. 1. Testing machine at room temperature[15]

Figure 2. 1 shows the automatic complex-loading testing machine (Shimadzu IS-10-TS) specially constructed for observing the history effect affecting on the deformation behaviour. As shown in the figure, it consists of a loading apparatus ①, a pressure generator ② as well as recording and controlling panels for axial force ③, torque ④ and internal pressure ⑤. A thin-walled tubular specimen is subjected to combined action of these three kinds of load so that the specimen may deform along arbitrarily specified shape of strain trajectory. The value of load or deformation of each kind is applied independently to the specimen through a photo-reader which traces along a specified curve described on a sheet fed with a constant speed, and the corresponding response is recorded precisely.

Each kind of load is measured by the corresponding dynamometer. The loading capacities of the testing machine are 98 kN (10 tons) in axial load (tension/compression), 49 kN-cm (5000 kgf-cm) in torque (right/left) and 58. 8 MPa (600 kgf/cm^2) in pressure, respectively.

Measurement of deformation in the specimen may be performed by using either strain-gauge of electric resistance type or differential transformer for obtaining mean value directly over the gauge length. The out-put from the strain gauge of each kind is recorded by the corresponding panel through an amplifier.

When the differential transformer is used, measurement is performed as follows. Axial elongation over the gauge length of specimen is transmitted to a differential transformer in a measuring device shown in Fig. 2. 2 as a relative displacement between knife-edges of the specimen, and the out-put from the transformer is

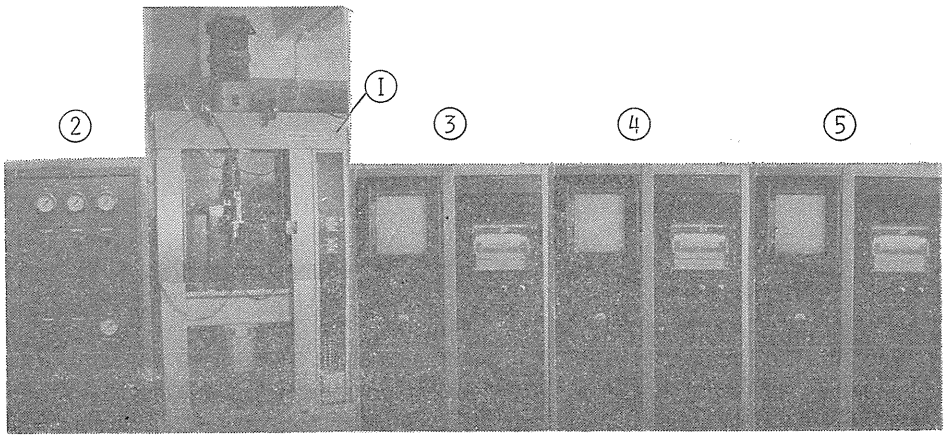

Fig. 2. 1 Automatic complex-loading testing machine.

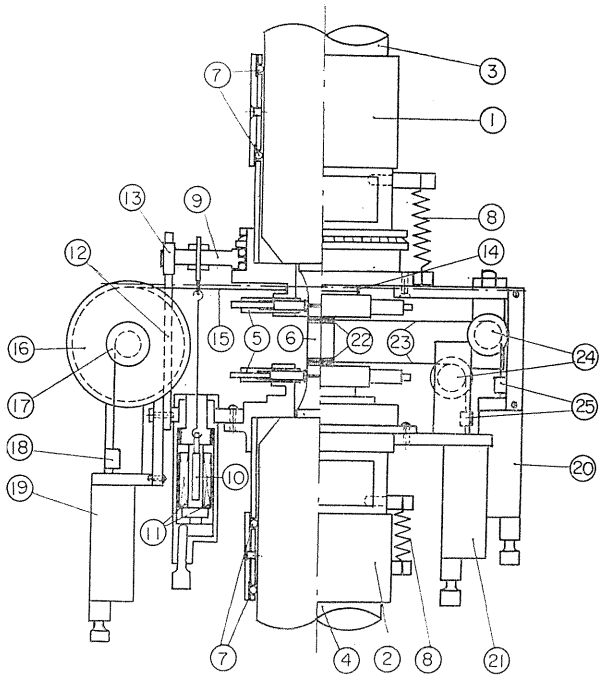

1 upper guide sleeve
2 lower guide sleeve
3 upper chuck
4 lower chuck
5 fastening pin (6 pieces)
6 specimen
7 ball
8 spring
9 arm
10 core of DTF
11 coil of DTF
12 tie rod
13 roller
14 guide groove
15 piano wire
16 larger guide disk
17 smaller guide disk
18 balance weight
19 differential transformer (DTF)
20 " "
21 " "
22 small roller (φ1 mm)
23 piano wire
24 guide roller
25 balance weight

Fig. 2. 2 Device for measuring deformation.

recorded on a sheet fed a constant speed in the recording panel ③. Torsional deformation appearing over the gauge length is converted into a relative movement between two fine piano-wires in the measuring device and recorded by the panel ④ through the differential transformer. Circumferential deformation of the specimen is measured through a very fine piano wire wound around the specimen at two locations where the mean value of deformation appears and is recorded by the panel ⑤ through the differential transformer. The differential transformer has an accuracy up to 10^{-3}mm. The accuracy of measurement may attain as high as 1.4 MPa (0.15 kgf/mm^2) in stress or 0.005 percent in strain.

Chapter Ⅲ Specimen

3. 1. Geometry of specimen[15,16]

Thin-walled tubular specimens for room temperature whose geometries are shown in Figs. 3.1 a and 3.1 b were machined from a bar of each material. Outer and inner surfaces over the gauge length were finished very smoothly with tolerances 21 ± 0.01mm and $19^{+0.01}_{0}$mm in diameters, respectively.

Measurement of deformation was performed by using either the electric resistance strain gauge or the differential transformer. In usual procedure, strain components in the specimen are measured by the strain gauge attached to the central part of the specimen. However, this does not always seem suitable to obtain proper mean value of strain over the gauge length, because the strain may

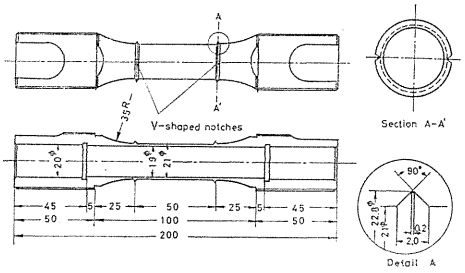

Fig. 3.1 a Geometry of specimen (dimension in mm).

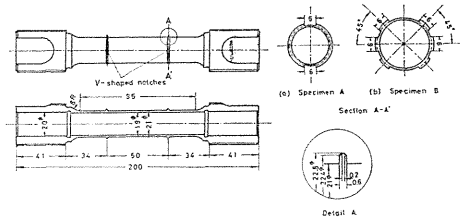

Fig. 3.1 b Geometry of specimen (for internal pressure, dimension in mm).

be obtained only over the range where the gauge is attached when the strain distribution is not uniform over the gauge length in the deformation within the range of yield step of mild steel for example. In such a case, the deformation state due to axial force or torque is preferable to be estimated as a mean value over the gauge length from the relative displacement between knife-edges at both ends.

In order to measure the circumferential strain, a variation in diameter at the center of gauge length is usually considered. However, the value is also affected by the local deformation state. In order to avoid the error due to circumferential irregularity in deformation state, a very fine piano-wire was used in winding around the specimen together with a row of small rollers arranged around the specimen. The circumferential relative displacement may be measured by the differential transformer as a movement at both ends of the wire. In order to avoid the effect on the uniformity of deformation state due to the restriction of knife-edge at both ends, the knife-edges are reduced to the only parts necessary to hold the measuring device (Fig. 3.1 b).

The location where the mean value of circumferential deformation appears under internal pressure has been found by a preliminary test, and the fine wire is wound at two such locations within the gange length.

The specimen shown in Fig. 3.1 a was used for axial force and torque, aud that shown in Fig. 3.1 b was used when internal pressure was combined with them. The specimen without knife-edges was used when the strain of each kind was measured by using the strain gauge.

By the way, a comparison of the results obtained by using the differential transformer and the strain gauge has shown that both results agree well with each other if a sufficient number of strain gauges are used for each kind of strain component.

3. 2. Materials of specimen

3. 2. 1. Mild steel[15]

Chemical components of mild steel S10C and S15C used are shown in Tables 3.1 a and 3.1 b. In order to obtain the state of initial isotropy, a bar of 36 mm diameter as-recieved was annealed carefully (furnace cooled after soaking at 880℃ for 1

Table 3. 1 (a) Chemical composition of mild steel S10C

Constituent	C	Si	Mn	S	P	Fe
Content (%)	0.10	0.24	0.44	0.009	0.018	Balance

Table 3. 1 (b) Chemical composition of mild steel S15C

Constituent	C	Si	Mn	S	P	Fe
Content (%)	0.12	0.23	0.48	0.035	0.021	Balance

hour). Since an effect of mean area of crystal grains on the mechanical property was recognized to be significant for this kind of measurement, the effect was taken into account to secure the reliable experimental results.

3. 2. 2. Brass[17]

The chemical composition of brass BsBM2 used is shown in Table 3. 2. For obtaining the initial isotropy, a bar of 36 mm diameter of brass was carefully annealed (furnace cooled after soaking at 580℃ for 8 hours). The optimum annealing condition was determined by preliminary test to obtain the isotropy in mechanical property as well as in grain configuration. The isotropy in mechanical property after annealing was examined by comparing the result of uniaxial tension test and that under internal pressure without axial restraint. The reproducibility of the mechanical property of specimen was confirmed on each piece sampled out from every lot annealed together.

Table 3. 2 Chemical composition of brass BsBM2

Constituent	Cu	Pb	Fe	Sn	Zn
Content (%)	54.85	3.03	0.03	0.02	Balance

3. 2. 3. Aluminum alloy[18]

The specimen was machined from a bar of 40 mm diameter of aluminum alloy 5056 whose chemical composition is shown in Table 3. 3.

Result of test on the bar in as-received state is shown in Fig. 3. 2. In the stress-strain curve shown in the figure, the difference between the stress values in the radial and axial directions of the bar at 4 % strain is only 1.7%, and the material may be regarded as almost isotropic. However, because the grain was elongated in the axial direction, the

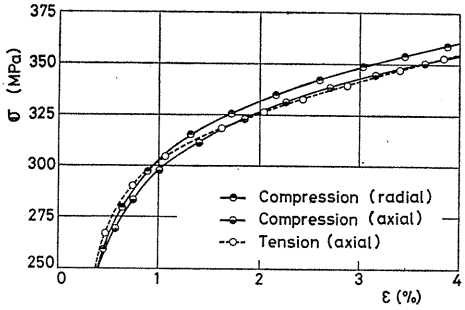

Fig. 3. 2 Stress-strain curve of aluminum alloy 5056 in as-received state.

Table 3. 3 Chemical composition of aluminum alloy 5056

Constituent	Cu	Si	Fe	Mg	Cr	Zn	Al
Content (%)	0.01	0.09	0.14	4.60	0.06	0.005	Balance

specimen was annealed in vacuum (furnace cooled after soaking at 340° for 20 minutes). Though the grain configuration became isotropically and the isotropy in mechanical property was improved, a slight yield step appeared after annealing on the experimental results at room temperature.

Chapter Ⅳ Tensor and Vector Spaces

4. 1. General relation beetween deviatoric tensors[19]

In the consideration of deformation properties of materials with regard to stress and strain or strain-increment as tensorial quantities, the properties may be expressed by the functional relations between these tensors. Moreover, as the relation between their spherical parts may be regarded as elastic for metals, the inelastic properties of metals may be discussed as the relation between their deviators.

The resulting variation in deformation properties after various plastic deformations of initially isotropic materials, that is the history effects on the deformation properties, may be formulated in a form of tensorial functional relation between the above-mentioned deviators in the isotropic deviatoric space. Thus the experimental results will be discussed in a form of the above-mentioned relation.

In order to formulate the experimental results in the most general form, the relation between a stress deviator $\boldsymbol{D}_\sigma(=s_{ij}\boldsymbol{e}_i\boldsymbol{e}_j;\ i,\ j=1,\ 2,\ 3)$ and a strain-increment deviator $\boldsymbol{D}_{de}(=de_{ij}\boldsymbol{e}_i\boldsymbol{e}_j;\ i,\ j=1,\ 2,\ 3)$ is derived, for example, where $\boldsymbol{e}_i(i=1,\ 2,\ 3)$ denote the base vectors which prescribe the space, $\boldsymbol{e}_i\boldsymbol{e}_j$ denote the corresponding base tensors, and s_{ij} and de_{ij} are the corresponding components. When a set of orthonormal base vectors concerning the principal directions of $\boldsymbol{D}_\sigma$ is selected as $\boldsymbol{e}'_i(i=1,\ 2,\ 3)$, the trigonometric form of $\boldsymbol{D}_\sigma$ may be expressed as

$$\boldsymbol{D}_\sigma=s_{ij}\boldsymbol{e}_i\boldsymbol{e}_j=(2/\sqrt{3})\zeta_\sigma\{\cos\alpha_\sigma\boldsymbol{e}'_1\boldsymbol{e}'_1-\cos(\alpha_\sigma+\pi/3)\boldsymbol{e}'_2\boldsymbol{e}'_2 -\cos(\alpha_\sigma-\pi/3)\boldsymbol{e}'_3\boldsymbol{e}'_3\},\tag{4.1a}$$

$$\zeta_\sigma^2=\mathrm{tr}(\boldsymbol{D}_\sigma^2)/2=I_2(\boldsymbol{D}_\sigma),$$

$$\cos 3\alpha_\sigma=(3\sqrt{3}/2)I_3(\boldsymbol{D}_\sigma)/I_2(\boldsymbol{D}_\sigma)^{3/2}=(3\sqrt{3}/2)I_3(\boldsymbol{D}_\sigma)/\zeta_\sigma^3,$$

$$I_3(\boldsymbol{D}_\sigma)=\mathrm{tr}(\boldsymbol{D}_\sigma^3)/3,\tag{4.1b}$$

where $I_2(\boldsymbol{D}_\sigma)$ and $I_3(\boldsymbol{D}_\sigma)$ denote the second and third invariants of the stress deviator $\boldsymbol{D}_\sigma$, respectively, and α_σ denotes an angle expressing the stress state (Fig. 4. 1).

In terms of three deviatoric base tensors with respect to the stress deviator

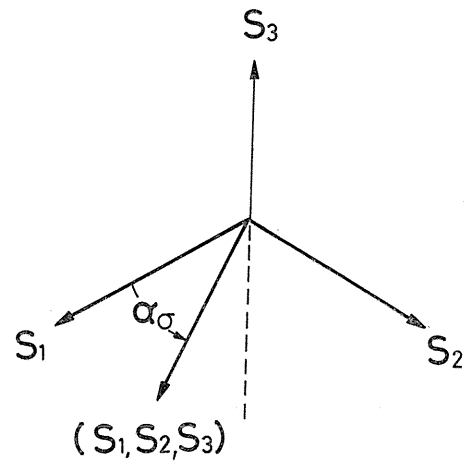

Fig. 4. 1 Plane Π of stress deviator $\boldsymbol{D}_\sigma$: $s_i(i=1, 2, 3)$ denote the principal values of $\boldsymbol{D}_\sigma$.

$$\boldsymbol{G}_1=\sqrt{2/3}\,\delta_{ij}\boldsymbol{e}'_i\boldsymbol{e}'_j \quad (i,\ j=1,\ 2,\ 3),\quad \boldsymbol{G}_2=(1/\sqrt{3})(2\boldsymbol{e}'_1\boldsymbol{e}'_1-\boldsymbol{e}'_2\boldsymbol{e}'_2-\boldsymbol{e}'_3\boldsymbol{e}'_3),$$

$$\boldsymbol{G}_3=\boldsymbol{e}'_2\boldsymbol{e}'_2-\boldsymbol{e}'_3\boldsymbol{e}'_3, \tag{4. 2}$$

which are mutually orthonormal, the expression (4.1 a) may be rewritten in the following form:

$$\boldsymbol{D}_\sigma=\zeta_\sigma(\cos\alpha_\sigma\boldsymbol{G}_2+\sin\alpha_\sigma\boldsymbol{G}_3). \tag{4. 3}$$

In the same way, the strain-increment deviator $\boldsymbol{D}_{de}$ may be expressed in terms of a set of orthonormal base vectors $\boldsymbol{d}_i(i=1, 2, 3)$ along the principal directions of $\boldsymbol{D}_{de}$ in the following form;

$$\boldsymbol{D}_{de}=\zeta_{de}(\cos\alpha_{de}\boldsymbol{H}_2+\sin\alpha_{de}\boldsymbol{H}_3),$$

$$\zeta^2_{de}=\mathrm{tr}(\boldsymbol{D}^2_{de})/2=I_2(\boldsymbol{D}_{de}), \tag{4. 4a}$$

$$\cos 3\alpha_{de}=(3\sqrt{3}/2)I_3(\boldsymbol{D}_{de})/I_2(\boldsymbol{D}_{de})^{3/2}=(3\sqrt{3}/2)I_3(\boldsymbol{D}_{de})/\zeta^3_{de},$$

$$I_3(\boldsymbol{D}_{de})=\mathrm{tr}(\boldsymbol{D}^3_{de})/3, \tag{4. 4b}$$

where $I_2(\boldsymbol{D}_{de})$ and $I_3(\boldsymbol{D}_{de})$ denote the second and third invariants of the strain-increment deviator $\boldsymbol{D}_{de}$, respectively, and α_{de} denotes an angle expressing the strain-increment state.

$$\boldsymbol{H}_1=\sqrt{2/3}\,\delta_{ij}\boldsymbol{d}_i\boldsymbol{d}_j \quad (i,\ j=1,\ 2,\ 3),\quad \boldsymbol{H}_2=(1/\sqrt{3})(2\boldsymbol{d}_1\boldsymbol{d}_1-\boldsymbol{d}_2\boldsymbol{d}_2-\boldsymbol{d}_3\boldsymbol{d}_3),$$

$$\boldsymbol{H}_3=\boldsymbol{d}_2\boldsymbol{d}_2-\boldsymbol{d}_3\boldsymbol{d}_3 \tag{4. 5}$$

are designated as base tensors along the principal directions of the strain-increment deviator $\boldsymbol{D}_{de}$, which are orthonormal with each other.

Since the principal directions of $\boldsymbol{D}_\sigma$ and $\boldsymbol{D}_{de}$ are not always coaxial in general

plastic deformation, the above-mentioned two sets of base tensors $\boldsymbol{G}_i$ and $\boldsymbol{H}_i (i=1, 2, 3)$ may differ from each other. Since the functional relation between the deviators $\boldsymbol{D}_\sigma$ and $\boldsymbol{D}_{de}$ should be derived on common bases, the deviator $\boldsymbol{D}_{de}$ is expressed with respect to the base $\boldsymbol{G}_i$ of $\boldsymbol{D}_\sigma$.

By introducing a rotation tensor $\boldsymbol{L}$ of orthonormal system such as

$$\boldsymbol{e}'_i=\boldsymbol{L}\boldsymbol{d}_i \quad (i=1, 2, 3) \tag{4.6}$$

and using the relation

$$\boldsymbol{e}'_i\boldsymbol{e}'_j=\boldsymbol{L}\boldsymbol{d}_i\boldsymbol{d}_j\boldsymbol{L}^{-1} \text{ or } \boldsymbol{d}_i\boldsymbol{d}_j=\boldsymbol{L}^{-1}\boldsymbol{e}'_i\boldsymbol{e}'_j\boldsymbol{L},$$

the following relation is obtained:

$$\boldsymbol{H}_i=\boldsymbol{L}^{-1}\boldsymbol{G}_i\boldsymbol{L} \quad (i=1, 2, 3). \tag{4.7}$$

By substituting the relation (4.7) into (4.4 a), a form is obtained in which $\boldsymbol{D}_{de}$ is expressed with respect to the orthonormal base tensor $\boldsymbol{G}_i$ for the deviator $\boldsymbol{D}_\sigma$ as follows:

$$\boldsymbol{L}\boldsymbol{D}_{de}\boldsymbol{L}^{-1}/\zeta_{de}=\cos\alpha_{de}\boldsymbol{G}_2+\sin\alpha_{de}\boldsymbol{G}_3. \tag{4.8}$$

In order to construct the base tensors $\boldsymbol{G}_2$ and $\boldsymbol{G}_3$ as two tensors with respect to $\boldsymbol{L}\boldsymbol{D}_{de}\boldsymbol{L}^{-1}/\zeta_{de}$, a quadratic deviator of $\boldsymbol{L}\boldsymbol{D}_{de}\boldsymbol{L}^{-1}/\zeta_{de}$

$$\begin{aligned}(\boldsymbol{L}\boldsymbol{D}_{de}\boldsymbol{L}^{-1}/\zeta_{de})^2-\sqrt{2/3}\boldsymbol{G}_1&=\boldsymbol{L}\boldsymbol{D}_{de}^2\boldsymbol{L}^{-1}/\zeta_{de}^2-\sqrt{2/3}\boldsymbol{G}_1\\&=(1/\sqrt{3})(\cos 2\alpha_{de}\boldsymbol{G}_2-\sin 2\alpha_{de}\boldsymbol{G}_3)\end{aligned} \tag{4.9}$$

may be selected as the simplest normarized tensor which is not coaxial with $\boldsymbol{L}\boldsymbol{D}_{de}\boldsymbol{L}^{-1}/\zeta_{de}$. In this respect, the relation between the orthonormal base tensors

$$\begin{aligned}&\boldsymbol{G}_2\boldsymbol{G}_2=\sqrt{2/3}\boldsymbol{G}_1+(1/\sqrt{3})\boldsymbol{G}_2, \quad \boldsymbol{G}_2\boldsymbol{G}_3=\boldsymbol{G}_3\boldsymbol{G}_2=-(1/\sqrt{3})\boldsymbol{G}_3,\\&\boldsymbol{G}_3\boldsymbol{G}_3=\sqrt{2/3}\boldsymbol{G}_1-(1/\sqrt{3})\boldsymbol{G}_2\end{aligned} \tag{4.10}$$

found from the relation (4.2) were used.

The following expressions are derived from Eqs. (4.8) and (4.9):

$$\begin{aligned}\sin 3\alpha_{de}\boldsymbol{G}_3&=\cos 2\alpha_{de}(\boldsymbol{L}\boldsymbol{D}_{de}\boldsymbol{L}^{-1}/\zeta_{de})\\&\quad-3\cos\alpha_{de}(\boldsymbol{L}\boldsymbol{D}_{de}^2\boldsymbol{L}^{-1}/\zeta_{de}^2-\sqrt{2/3}\boldsymbol{G}_1),\\\sin 3\alpha_{de}\boldsymbol{G}_2&=\sin 2\alpha_{de}(\boldsymbol{L}\boldsymbol{D}_{de}\boldsymbol{L}^{-1}/\zeta_{de})\\&\quad+3\sin\alpha_{de}(\boldsymbol{L}\boldsymbol{D}_{de}^2\boldsymbol{L}^{-1}/\zeta_{de}^2-\sqrt{2/3}\boldsymbol{G}_1).\end{aligned} \tag{4.11}$$

In the case of $\sin 3\alpha_{de}\neq 0$, the following relation between stress and strain-increment deviators may be obtained by substituting $\boldsymbol{G}_2$ and $\boldsymbol{G}_3$ from Eq. (4.11) into Eq. (4.3):

$$\begin{aligned}\boldsymbol{D}_\sigma/\zeta_\sigma=(1/\sin 3\alpha_{de})\{&\sin(2\alpha_{de}+\alpha_\sigma)\boldsymbol{L}\boldsymbol{D}_{de}\boldsymbol{L}^{-1}/\zeta_{de}\\&+\sqrt{3}\sin(\alpha_{de}-\alpha_\sigma)(\boldsymbol{L}\boldsymbol{D}_{de}^2\boldsymbol{L}^{-1}/\zeta_{de}^2-\sqrt{2/3}\boldsymbol{G}_1)\}.\end{aligned} \tag{4.12}$$

When the deviators $\boldsymbol{D}_\sigma$ and $\boldsymbol{D}_{de}$ are coaxial, the rotation tensor is reduced to the unit tensor $\boldsymbol{I}$ and the well-known relation[20] is obtained as follows:

$$\boldsymbol{D}_\sigma/\zeta_\sigma=(1/\sin 3\alpha_{de})\{\sin(2\alpha_{de}+\alpha_\sigma)\boldsymbol{D}_{de}/\zeta_{de} + \sqrt{3}\sin(\alpha_{de}-\alpha_\sigma)(\boldsymbol{D}_{de}^2/\zeta_{de}^2-\sqrt{2/3}\boldsymbol{G}_1)\}. \tag{4.13}$$

In the case of $\alpha_\sigma=\alpha_{de}$ in Eq. (4.13), the relation between $\boldsymbol{D}_\sigma$ and $\boldsymbol{D}_{de}$ is reduced to the linear relation corresponding to the St.Venant-Levy-Mises Law used conventionally:

$$D_\sigma=(\zeta_\sigma/\zeta_{de})\boldsymbol{D}_{de}. \tag{4.14}$$

In the case of $\sin 3\alpha_{de}=0$, the following relation is obtained from Eq. (4.11):

$$\pm\boldsymbol{L}\boldsymbol{D}_{de}\boldsymbol{L}^{-1}/\zeta_{de}=3(\boldsymbol{L}\boldsymbol{D}_{de}^2\boldsymbol{L}^{-1}/\zeta_{de}^2-\sqrt{2/3}\boldsymbol{G}_1).$$

Thus the quadratic deviator cannot be used as the base tensor. In such a case, the deviator $\boldsymbol{D}_\sigma$ may be expressed in the following form by selecting $\boldsymbol{L}\boldsymbol{D}_{de}\boldsymbol{L}^{-1}/\zeta_{de}$ and $\boldsymbol{G}_3$ as base tensors, for example,

$$\boldsymbol{D}_\sigma=\zeta_\sigma\{\cos\alpha_\sigma(\boldsymbol{L}\boldsymbol{D}_{de}\boldsymbol{L}^{-1}/\zeta_{de})+\sin\alpha_\sigma\boldsymbol{G}_3\}. \tag{4.15}$$

4. 2. Deviatoric strain vector space and deviatoric stress vector space

As shown in Eqs. (4.1 b) and (4.4 b), each third invariant depends on the angle α_σ or α_{de}. The angle α_σ or α_{de} expresses the state of $\boldsymbol{D}_\sigma$ or $\boldsymbol{D}_{de}$, i. e., the relation between the elements of the deviator. For convenience, this relation may be expressed geometrically in the corresponding vector space. Since geometric representation is very effective in discussing the history effect on the deformation behaviour of materials, the behaviours are expressed in the vector space corresponding to the deviatoric tensor space. In this respect, a special care must be taken in expressing experimental results, because the first and third invariants of the tensor cannot be expressed explicitly whereas the second one can be expressed in the isotropic vector space.

A strain deviator $\boldsymbol{D}_e=e_{ij}\boldsymbol{e}_i\boldsymbol{e}_j$ $(i,\ j=1,\ 2,\ 3)$ may be expanded as follows:

$$\boldsymbol{D}_e=e_k\boldsymbol{A}_k\quad(k=1,\ 2,\ \cdots,\ 5) \tag{4.16}$$

with respect to five orthonormal base tensors:

$$\boldsymbol{A}_k=A_{ij}^k\boldsymbol{e}_i\boldsymbol{e}_j\quad(k=1,\ 2,\ \cdots,\ 5;\ i,\ j=1,\ 2,\ 3).$$

The scalar coefficients e_k have the following relation in connection with e_{ij}:

$$e_{ij}=e_kA_{ij}^k\quad(i,j=1,\ 2,\ 3;\ k=1,\ 2,\ \cdots 5). \tag{4.17}$$

The relation

$$e_{ij}e_{ij}=e_ke_k\quad(i,j=1,\ 2,\ 3;\ k=1,\ 2,\ \cdots,\ 5) \tag{4.18}$$

together with

$$\sqrt{3/2}\,e_{mm}=B_{mk}e_k \quad (m=1,\ 2,\ 3 \text{ are not summed};\ k=1,\ 2),$$
$$\sqrt{2}\,e_{12}=e_3,\quad \sqrt{2}\,e_{23}=e_4,\quad \sqrt{2}\,e_{31}=e_5 \tag{4.19}$$

is designated between the second invariant in the deviatoric tensor space and the invariant in the corresponding vector space, wher B_{mk} are scalar coefficients.

The following relations hold between e_k and e_{ij}:

$$e_1=\sqrt{2}\{e_{11}\cos(\gamma+\pi/6)-e_{22}\cos\gamma\},$$
$$e_2=\sqrt{2}\{e_{11}\sin(\gamma+\pi/6)+e_{22}\cos\gamma\},$$
$$e_3=\sqrt{2}\,e_{12},\quad e_4=\sqrt{2}\,e_{23},\quad e_5=\sqrt{2}\,e_{31}. \tag{4.20}$$

On the other hand, the following expressions are obtained for the base tensors $\boldsymbol{A}_k$ $(k=1,\ 2,\ \cdots,\ 5)$,

$$\boldsymbol{A}_1=\sqrt{2/3}\{\cos\gamma\,\boldsymbol{e}_1\boldsymbol{e}_1-\sin(\gamma+\pi/6)\boldsymbol{e}_2\boldsymbol{e}_2+\sin(\gamma-\pi/6)\boldsymbol{e}_3\boldsymbol{e}_3\},$$
$$\boldsymbol{A}_2=\sqrt{2/3}\{\sin\gamma\,\boldsymbol{e}_1\boldsymbol{e}_1+\cos(\gamma+\pi/6)\boldsymbol{e}_2\boldsymbol{e}_2-\cos(\gamma-\pi/6)\boldsymbol{e}_3\boldsymbol{e}_3\},$$
$$\boldsymbol{A}_3=\sqrt{2/3}\cos(\pi/6)(\boldsymbol{e}_1\boldsymbol{e}_2+\boldsymbol{e}_2\boldsymbol{e}_1),\quad \boldsymbol{A}_4=\sqrt{2/3}\cos(\pi/6)(\boldsymbol{e}_2\boldsymbol{e}_3+\boldsymbol{e}_3\boldsymbol{e}_2),$$
$$\boldsymbol{A}_5=\sqrt{2/3}\cos(\pi/6)(\boldsymbol{e}_3\boldsymbol{e}_1+\boldsymbol{e}_1\boldsymbol{e}_3), \tag{4.21}$$

where γ is an arbitrary parameter. From Eq. (4.21), the base tensors $\boldsymbol{A}_k$ are found to be orthonormal.

From Eqs. (4.16), (4.20) and (4.21), the state of deviatoric strain corresponding to $\boldsymbol{D}_e$ may be expressed by the coefficients e_i $(i=1,\ 2,\ \cdots,\ 5)$ by using the base tensors $\boldsymbol{A}_k$ constructed from a set of suitably prescribed orthonormal base vectors $\boldsymbol{e}_i$. Thus the deviatoric strain vector

$$\boldsymbol{e}=e_k\boldsymbol{n}_k \quad (k=1,\ 2,\ \cdots,\ 5;\ \boldsymbol{n}_k : \text{orthonormal base vectors}) \tag{4.22}$$

may be introduced for the state of deviatoric strain corresponding to $\boldsymbol{D}_e$, if a five-dimensional vector space V_{5e} of deviatoric strain

$$[e_1,\ e_2,\ \cdots,\ e_5]=[\sqrt{2}\{e_{11}\cos(\gamma+\pi/6)-e_{22}\sin\gamma\},$$
$$\sqrt{2}\{e_{11}\sin(\gamma+\pi/6)+e_{22}\cos\gamma\},\ \sqrt{2}\,e_{12},\ \sqrt{2}\,e_{23},\ \sqrt{2}\,e_{31}] \tag{4.23}$$

is used. This vector space has been introduced by Ilyushin.[9]

By an approximation that the plane stress state appears in the tubular specimen, if the axis-3 is selected in the radial direction of the specimen, the components of stress $\sigma_{i3}(i=1,\ 2,\ 3)$ and strain $\varepsilon_{i3}(i=1,\ 2)$ vanish, and thus the axis-3 becomes a fixed principal axis for the stress deviator $\boldsymbol{D}_\sigma$ or strain deviator $\boldsymbol{D}_e$. Then, $\boldsymbol{D}_e$ may be expressed as follows for $\gamma=0$:

$$\boldsymbol{D}_e=\sqrt{3/2}\,[e_{11}\{\sqrt{2/3}(\boldsymbol{e}_1\boldsymbol{e}_1-\boldsymbol{e}_2\boldsymbol{e}_2/2-\boldsymbol{e}_3\boldsymbol{e}_3/2)\}+(2/\sqrt{3})(e_{11}/2$$
$$+e_{22})\{\sqrt{1/2}(\boldsymbol{e}_2\boldsymbol{e}_2-\boldsymbol{e}_3\boldsymbol{e}_3)\}+(2/\sqrt{3})e_{12}\sqrt{1/2}(\boldsymbol{e}_1\boldsymbol{e}_2+\boldsymbol{e}_2\boldsymbol{e}_1)]$$
$$=e_k\boldsymbol{A}_k \quad (k=1,\ 2,\ 3). \tag{4.24}$$

Accordingly, the state of deviatoric strain corresponding to $\boldsymbol{D}_e$ given in Eq. (4.24) may be expressed by a strain vector

$$\boldsymbol{e}=e_{11}\boldsymbol{n}_1+(2/\sqrt{3})(e_{11}/2+e_{22})\boldsymbol{n}_2+(2/\sqrt{3})e_{12}\boldsymbol{n}_3 \tag{4.25}$$

in a three-dimensional vector space V_{3e}

$$[e_1,\ e_2,\ e_3]=[e_{11},\ (2/\sqrt{3})(e_{11}/2+e_{22}),\ (2/\sqrt{3})e_{12}]. \tag{4.26}$$

The history of deviatoric strain may be expressed by a hodograph of the strain vector $\boldsymbol{e}$(strain trajectory) in the vector space V_{3e}.

The state of deviatoric stress at an arbitrary point on the strain trajectory may be expressed by a deviatoric stress vector

$$\boldsymbol{\sigma}=(3/2)\{s_{11}\boldsymbol{n}_1+(2/\sqrt{3})(s_{11}/2+s_{22})\boldsymbol{n}_2+(2/\sqrt{3})s_{12}\boldsymbol{n}_3\} \tag{4.27}$$

in a local vector space $V_{3\sigma}$ established at that point

$$[\sigma_1,\ \sigma_2,\ \sigma_3]=[(3/2)s_{11},\ \sqrt{3}(s_{11}/2+s_{22}),\ \sqrt{3}s_{12}], \tag{4.28}$$

corresponding to the deviatoric stress, where $s_{ij}(i,\ j=1,\ 2,\ 3)$ are components of $\boldsymbol{D}_\sigma$, and $\sigma_k(k=1,\ 2,\ 3)$ denote the components introduced for $\boldsymbol{D}_\sigma$ in the same way as in the relation (4.26).

In the representation (4.24), if the base vector $\boldsymbol{e}_1$ and $\boldsymbol{e}_2$ rotate orthogonally around the base vector $\boldsymbol{e}_3$ corresponding to the fixed principal axis of $\boldsymbol{D}_e$, the components e_{11}, e_{22} and e_{12} of $\boldsymbol{D}_e$ vary so as to correspond to the basis after rotation, and the strain vector $\boldsymbol{e}$ also rotate around the origin in the space V_{3e}. Thus, a history of a deviatoric strain state given in the space established with the base tensor $\boldsymbol{A}_k(k=1,\ 2,\ 3)$ may correspond to a set of strain trajectories in the isotropic space V_{3e}. In other words, the strain trajectories in such a set may be equivalent to each other nevertheless these have different orientations in that space. On the other hand, the strain trajectories which are tensorially equivalent may be confirmed to have an identical geometry in the space V_{3e}.

The magnitude $|\boldsymbol{e}|$ and direction $(\phi_e,\ \theta_e)$ of the deviatoric strain vector $\boldsymbol{e}$ in the space V_{3e} and the magnitude $|\boldsymbol{\sigma}|$ and direction $(\phi_\sigma,\ \theta_\sigma)$ of the deviatoric stress vector $\boldsymbol{\sigma}$ in the local space $V_{3\sigma}$ appearing in (4.25) through (4.28) are expressed as:

$$|\boldsymbol{e}|=(e_1^2+e_2^2+e_3^2)^{1/2}=\{e_{11}^2+(4/3)(e_{11}/2+e_{22})^2+(4/3)e_{12}^2\}^{1/2},$$

$$\tan\phi_e=e_2/e_1=(e_{11}+2e_{22})/\sqrt{3}e_{11},\ \cos\theta=\boldsymbol{e}\cdot\boldsymbol{n}_3/|\boldsymbol{e}|=2e_{12}/\sqrt{3}|\boldsymbol{e}|, \tag{4.29}$$

$$|\boldsymbol{\sigma}|=(\sigma_1^2+\sigma_2^2+\sigma_3^2)^{1/2}=(3/2)\{s_{11}^2+(4/3)(s_{11}/2+s_{22})^2+(4/3)s_{12}^2\}^{1/2},$$

$$\tan\phi_\sigma=\sigma_2/\sigma_1=(s_{11}+2s_{22})/\sqrt{3}s_{11},\ \cos\theta_\sigma=\boldsymbol{\sigma}\cdot\boldsymbol{n}_3/|\boldsymbol{\sigma}|=\sqrt{3}s_{12}/|\boldsymbol{\sigma}|. \tag{4.30}$$

As found from Eqs. (4.29) and (4.30), the magnitudes $|\boldsymbol{e}|$ and $|\boldsymbol{\sigma}|$ agree with the equivalent strain and the equivalent stress, respectively.

4. 3. Distributions of the first and third invariants in the three-dimensional vector space

Since the second invariant $I_2(\boldsymbol{D})$ of the deviatoric tensor is maintained in the

corresponding vector space introduced in the provious section, the magnitude of $I_2(\boldsymbol{D})$ is kept constant at every point on the spherical surface around the origin in the vector space. On the contrary, values of the third invariant $I_3(\boldsymbol{D})$ of the deviator and the first invariant $I_1(\boldsymbol{T})$ of the tensor are not constant but functions of orientation in the vector space. Thus, the distributions of $I_3(\boldsymbol{D})$ and $I_1(\boldsymbol{T})$ on the surface of unit sphere in the vector space are discussed in the following.

A reduced value $\bar{I}_3(\boldsymbol{D}_e)$ of the third invariant of the strain deviator $\boldsymbol{D}_e$ by means of the second invariant $I_2(\boldsymbol{D}_e)$ may be expressed in terms of the components $e_i(i=1, 2, 3)$ of the deviatoric strain vector $\boldsymbol{e}$ as follows:

$$\bar{I}_3(\boldsymbol{D}_e)=\{e_1(e_1^2-3e_2^2)+(3/2)(e_1+\sqrt{3}e_2)e_3^2\}/(e_1^2+e_2^2+e_3^2)^{3/2}$$
$$=\sin\theta_e\{\sin^2\theta_e\cos 3\phi_e+3\cos^2\theta_e\cos(\phi_e-\pi/3)\}. \qquad (4.31)$$

As found from Eq. (4.31), a distribution of $\bar{I}_3(\boldsymbol{D}_e)$ in the space V_{3e} depends only on the orientation and may be expressed by the curves on the unit sphere in Fig. 4.2 obtained as an intersection of Eq. (4.31) and the surface of the unit sphere $e_1^2+e_2^2+e_3^2=1$.

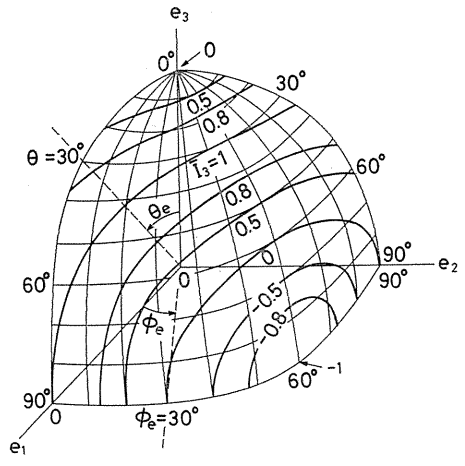

Fig. 4.2 Distribution of $\bar{I}_3(\boldsymbol{D}_e)$ in the space V_{3e}.

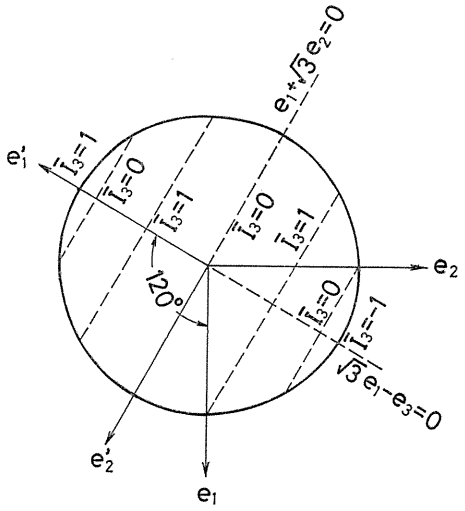

Fig. 4.3 Projection of the curves $\bar{I}_3(\boldsymbol{D}_e)=$ const on the plane e_1e_2.

Projections of these curves $\bar{I}_3(\boldsymbol{D}_e)$ onto the plane e_1e_2 become a set of straight segments shown in Fig. 4.3 with the dashed lines in the range $-1\leq e_1+\sqrt{3}e_2\leq 1$, and may be expressed by one of the solutions of the following cubic equation obtained by eliminating e_3 from $e_1^2+e_2^2+e_3^2=1$ and Eq. (4.31):

$$(e_1+\sqrt{3}e_2)^3-3(e_1+\sqrt{3}e_2)+2\bar{I}_3(\boldsymbol{D}_e)=0.$$

The solution of this equation satisfying the condition $-1\leq e_1+\sqrt{3}e_2\leq 1$ is found as follows:

$$e_1+\sqrt{3}e_2=-2\cos(2\pi/3-\alpha_e),$$

where

$$\alpha_e=(1/3)\arccos\{\bar{I}_3(\boldsymbol{D}_e)\}. \tag{4.32}$$

On the other hand, the curves $\bar{I}_3(\boldsymbol{D}_e)$ on the spherical surface are projected as a set of concentric circles on the plane $e_1+\sqrt{3}e_2=0$.

In the same manner, a reduced value $\bar{I}_3(\boldsymbol{D}_\sigma)$ of the third invariant of the stress deviator $\boldsymbol{D}_\sigma$ may be expressed by the components $\sigma_i(i=1, 2, 3)$ of the deviatoric stress vector $\boldsymbol{\sigma}$ as follows:

$$\begin{aligned}\bar{I}_3(\boldsymbol{D}_\sigma)&=3\sqrt{6}I_3(\boldsymbol{D}_\sigma)/I_2(\boldsymbol{D}_\sigma)^{3/2}\\&=\{\sigma_1(\sigma_1^2-3\sigma_2^2)+(3/2)(\sigma_1+\sqrt{3}\sigma_2)\sigma_3\}/(\sigma_1^2+\sigma_2^2+\sigma_3^2)^{3/2}\\&=\sin\theta_\sigma\{\sin^2\theta_\sigma\cos 3\phi_\sigma+3\cos^2\theta_\sigma\cos(\phi_\sigma-\pi/3)\}.\end{aligned} \tag{4.33}$$

A distribution of $\bar{I}_3(\boldsymbol{D}_\sigma)$ may be expressed by a set of dashed curves on the surface of unit sphere as shown in Fig. 4.4, as the intersection of $\sigma_1^2+\sigma_2^2+\sigma_3^2=1$ and Eq. (4.33).

The first invariant $I_1(\boldsymbol{T}_\sigma)$ of the stress tensor $\boldsymbol{T}_\sigma=\sigma_{ij}\boldsymbol{e}_i\boldsymbol{e}_j(i, j=1, 2, 3)$ is expressed as follows:

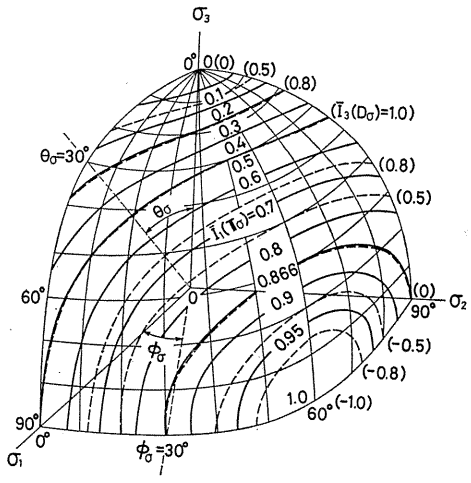

Fig. 4. 4 Distributions of $\bar{I}_3(\mathrm{D}_\sigma)$ and $\bar{I}_1(\boldsymbol{T}_\sigma)$ in the space $\mathrm{V}_{3\sigma}$.

$$I_1(\boldsymbol{T}_\sigma)=\mathrm{tr}(\boldsymbol{T}_\sigma)=\sigma_{11}+\sigma_{22}+\sigma_{33}. \tag{4.34}$$

Since the plane stress state ($\sigma_{33}=0$) may be assumed in the thin-walled tubular specimen, $I_1(\boldsymbol{T}_\sigma)$ may be approximated as follows in considering Eq. (4.28):

$$I_1(\boldsymbol{T}_\sigma)=\sigma_{11}+\sigma_{22}=\sigma_1+\sqrt{3}\sigma_2. \tag{4.35}$$

A dimensionless value $\bar{I}_1(\boldsymbol{T}_\sigma)$ reduced by the second invariant $I_2(\boldsymbol{D}_\sigma)$ is expressed as

$$\begin{aligned}\bar{I}_1(\boldsymbol{T}_\sigma)&=(1/2)I_1(\boldsymbol{T}_\sigma)/\{3I_2(\boldsymbol{D}_\sigma)\}^{1/2}=(\sigma_1+\sqrt{3}\sigma_2)/(2|\boldsymbol{\sigma}|)\\&=\sin\theta_\sigma\cos(\phi_\sigma-\pi/3).\end{aligned} \tag{4.36}$$

A distribution of $\bar{I}_1(\boldsymbol{T}_\sigma)$ in the space $\mathrm{V}_{3\sigma}$ may be expressed by a set of solid

curves on the surface of the unit sphere as shown in Fig. 4.4. The following relation is obtained from Eqs. (4.33) and (4.36) for $\bar{I}_3(\boldsymbol{D}_\sigma)$ and $\bar{I}_1(\boldsymbol{T}_\sigma)$ in the space $V_{3\sigma}$.

$$\bar{I}_3(\boldsymbol{D}_\sigma)=-4\bar{I}_1(\boldsymbol{T}_\sigma)\{\bar{I}_1(\boldsymbol{T}_\sigma)+\sqrt{3}/2\}\{\bar{I}_1(\boldsymbol{T}_\sigma)-\sqrt{3}/2\}. \qquad (4.37)$$

It is found from Eq. (4.37) that the values $\bar{I}_1(\boldsymbol{T}_\sigma)=0,\ \pm\sqrt{3}/2$ correspond to $\bar{I}_3(\boldsymbol{D}_\sigma)=0$, and the value $\sqrt{3}/2$ is close to the extreme value $\bar{I}_1(\boldsymbol{T}_\sigma)=1$. As shown in Fig. 4.4, the following conditions exist:

$$\begin{aligned}&\bar{I}_1(\boldsymbol{T}_\sigma)=\sqrt{3}/2,\ \bar{I}_3(\boldsymbol{D}_\sigma)=0 \quad \text{along the axis-}\sigma_2,\\ &\bar{I}_1(\boldsymbol{T}_\sigma)=0, \qquad \bar{I}_3(\boldsymbol{D}_\sigma)=0 \quad \text{along the axis-}\sigma_3. \end{aligned} \qquad (4.38)$$

As found from Fig. 4.2, there is a regular distribution of $-1\leq\bar{I}_3(\boldsymbol{D}_e)\leq 1$ in the space V_{3e}, and the distribution of $\bar{I}_3(\boldsymbol{D}_\sigma)$ is also governed by the same regularity, as shown in Fig. 4.4. Especially, in the plane-$\sigma_1\sigma_3$, $\bar{I}_3(\boldsymbol{D}_\sigma)$ varies monotonously in the whole range from the value 1 along the axis-σ_1 to -1 along the axis-$(-\sigma_1)$ through the value 0 along the axis-σ_3. Accordingly, the most suitable tests for discussing the effect of $\bar{I}_3(\boldsymbol{D}_\sigma)$ on the deformation behaviour of materials are those using the proportional deformation in the plane-$\sigma_1\sigma_3$. Such tests may be performed by applying combined loads of axial force and torque to the thin-walled tubular specimen.

Chapter V Experimental Procedure

Experiments were performed on the proportional deformation and the deformation along orthogonal bi-linear and tri-linear strain trajectories by applying combined load of axial force (tension/compression), torque and internal pressure to the thin-walled tubular specimen, with the use of the automatic combined-loading testing machine IS-10-TS. An increasing rate of strain intensity along the trajectory was set mainly at $ds/dt=3\times10^{-6}/sec$ (t: time in second), which has been ascertained to affect little the stress-strain curve obtained for the plastic deformation of metals at room temperature.

Special care was paid to strain control in the experiment performed under internal pressure. In applying internal pressure to the tubular specimen, automatic control based on strain is disturbed just after the upper yield point by a sudden change of deformation state of specimen made of mild steel. Since the plastic deformation of mild steel develops at its lower yield stress, the strain may increase smoothly under strain control when the decrease of pressure due to an increase of volume inside the tubular specimen is recovered by a supply of oil so as the lower yield stress to be kept. However, such a smooth supply of oil is disturbed by a delay of response to the instantaneous defomation of tubular specimen just after the upper yield point, because of the compressibility of pressurized oil inside the specimen and pipe system connecting up with the oil pump and the elasticity of the pipe system as well. In other words, the stress value cannot decrease to the lower yield stress for the delay of response. Thus a large plastic strain, which is somewhat larger than the maximum yield strain, appears instantaneously for the stress value close to the upper yield point. In order to avoid this, the volume

inside the tubular specimen was kept as small as possible by the use of a close-fitting core within the specimen. Moreover, the effect of the elasticity of pipe system was eliminated by throttling an oil feed from the pipe system by means of an adjustable cock located very close to the specimen. These precautions enabled smooth strain control to be achieved.

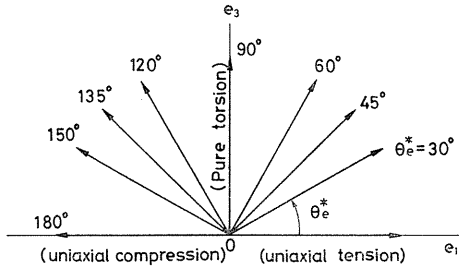

Fig. 5. 1 Deviatoric strain vector space V_{2e} for combined loads of axial force and torque.

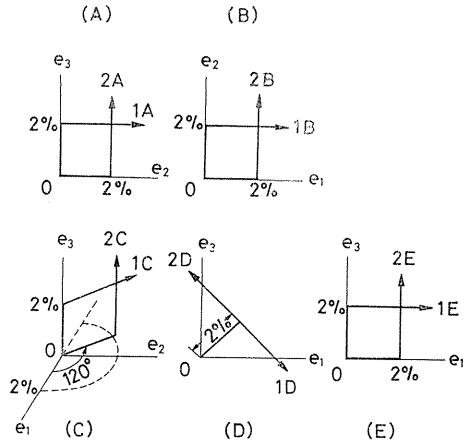

Fig. 5. 2 Orthogonal bi-linear strain trajectories in the space V_{3e}.

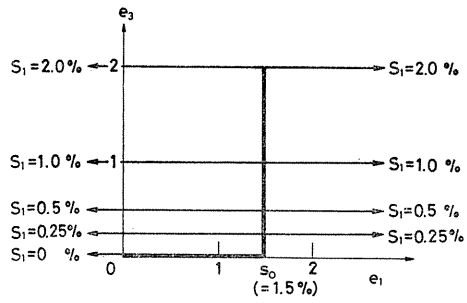

Fig. 5.3 a Orthogonal tri-linear strain trajectories in the space V_{2e}.

5. 1. *Proportional deformation*

The proportional deformation test was performed along the strain trajectories starting from the zero-strain point in V_{2e} (Fig. 5. 1) or V_{3e} (Fig. 4. 2). The trajectories may be specified by angular directions θ_e^* or ϕ_e and θ_e.

5. 2. *Orthogonal bi-linear strain trajectory*

Figure 5. 2 shows the strain trajectories consisting of two straight branches intersecting normally for which experiments were performed. For convenience of comparison between the experimental results, the pre-strain was mainly set at 2 percent for every case. These experiments were performed for discussing the validity of the "postulate of isotropy".

5. 3. *Orthogonal tri-linear strain trajectory*

Figure 5. 3 shows the orthogonal tri-

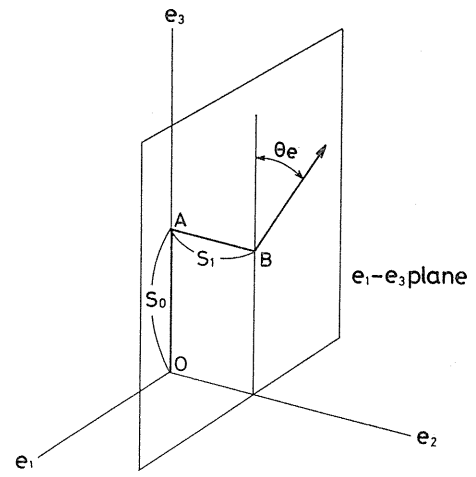

Fig. 5.3 b Orthogonal tri-linear strain trajectories in the space V_{3e}.

linear strain trajectories in the spaces V_{2e}(Fig. 5.3 a) and V_{3e}(Fig. 5.3 b). These experiments were performed for discussing the interaction between the effects of the first and second corners on the strain trajectory.

5. 4. Estimation of stress and strain components

In estimating the stress components from experimental data on the thin-walled tubular specimen, the stress components σ_z, σ_ϕ, τ_z were estimated as mean values by taking into account the effect due to the variation of size in the specimen owing to large deformation. Especially, the radial stress component σ_r due to internal pressure, which is neglected in general for the thin-walled tubular specimen, was taken into account for discussing precisely the history effect in plastic deformaiton because the radial stress is contained in the deviatoric stress components. The radial stress component was estimated as a mean value of the distribution of $\sigma_r(r)$ over the tube thickness under internal pressure calculated by the conventional method[21] of plastic analysis of thick tube. The error in neglecting σ_r amounted at most to 5 percent of $|\boldsymbol{\sigma}|$.

In the experiment, the circumferential strain component ε_ϕ of the specimen was estimated from the relative displacement measured on its outer surface. However, ε_ϕ of the tube under internal pressure is not uniform exactly over the wall thickness. Thus, a ratio of the mean value of ε_ϕ taken over the thickness to the value of ε_ϕ estimated on the outer surface was found by using the conventional method[21] of plastic analysis, and a mean value over the thickness was estimated from the value on the outer surface obtained by the experiment. The strain components ε_z, γ_z were estimated directly from the experimental data as mean values.

The components σ_z, σ_ϕ, τ_z and ε_z, ε_ϕ, γ_z estimated from the experimental data correspond to the above-mentioned components σ_{11}, σ_{22}, σ_{12} and ε_{11}, ε_{22}, $2\varepsilon_{12}$, respectively. The differences between the values of strain components and their deviatoric parts were negligibly small in the range where the deformation behaviour was discussed.

Chapter Ⅵ Experimental Results

6. 1. Experimental results for proportional deformation

6. 1. 1. Proportional deformation in the plane-e_1e_3 (V_{2e} for $\phi_e=0$)

Figure 6.1 shows the relation between $|\boldsymbol{\sigma}|$ and s^p† obtained for the mild steel S10C by the experiment on the proportional deformation along the trajectories shown in the inserted figure. As found from the figure, the curve for pure torsion ($\theta_e^*=90°$, $\bar{I}_3(\boldsymbol{D}_e)=0$) appears lowest and the curves become higher with an increase of the axial strain (or stress) component, and the corresponding curves in the hardening region are close to each other for each pair of strain trajectories which are symmetric with respect to the axis-e_3, although the curves on the compression

† Superfix p denotes hereafter the plastic part of the corresponding value obtained by subtracting the elastic part under an assumption of the constant elastic moduli during plastic deformation.

side ($90°\leq\theta_\varepsilon^*\leq180°$) appear a little higher than those on the tension side ($0°\leq\theta_\varepsilon^*\leq 90°$) and the trend is more pronounced on the yield step.

The angles θ_σ^* and θ_ε^* are expected to agree with each other for every proportional deformation. However, the experimental results proved that these angles did not always do so. They agree for $\theta_\varepsilon^*=0°$ and 180°, but the angle θ_σ^* is smaller than on the tension side and larger on the compression side than the angle θ_ε^*. As shown in Fig. 6.2, the values of $|\theta_\varepsilon^*-\theta_\sigma^*|$ remain almost constant at less than 5°.

Figure 6.3 shows the same curves obtained for brass BsBM2 for the trajectories shown in the inserted figure[22]. Since

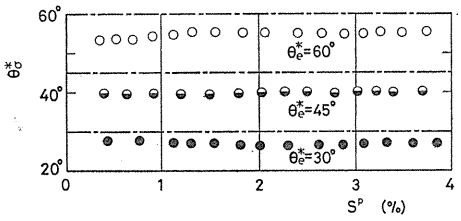

Fig. 6. 2 Relation between the angles θ_σ^*, θ_ε^* and s^p of mild steel S10C.

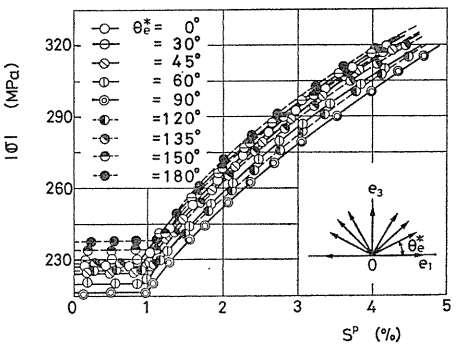

Fig. 6. 1 $|\boldsymbol{\sigma}|\sim s^p$ curves for proportional deformation of mild steel S10C under combined loads of axial force and torque.

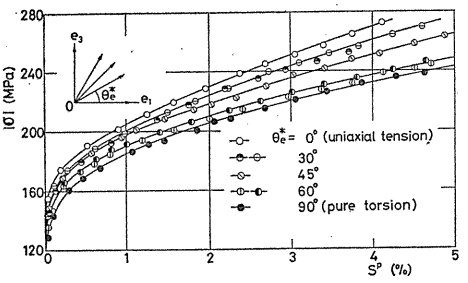

Fig. 6. 3 $|\boldsymbol{\sigma}|\sim s^p$ curves for proportional deformation of brass BsBM2 under combined loads of axial force and torque.

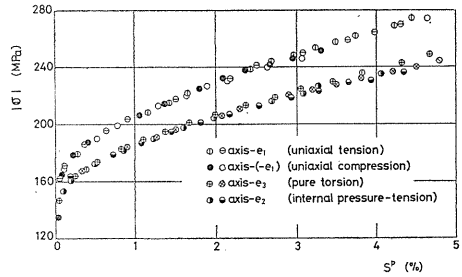

Fig. 6. 4 Results of proportional deforamtion along each axis in the space $V_{3\varepsilon}$.

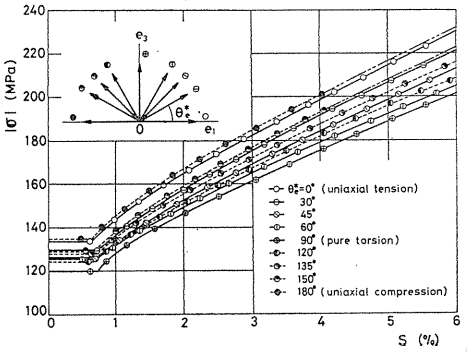

Fig. 6. 5 $|\boldsymbol{\sigma}|\sim s$ curves for proportional deformation of aluminum alloy 5056 under combined loads of axial force and torque.

the curves for uniaxial tension (e_1-axis) and compresssion ($-e_1$-axis) agree almost completely for brass, the curves are shown only for the tension side. The curve for each axis in strain space is shown in Fig. 6.4.

Figure 6.5 shows the curves for aluminum alloy 5056 for the trajectories shown in the inserted figure[18]. As found from Figs. 6.3 and 6.5, the curves for pure torsion appears lowest and the curves become higher with increase of axial strain component. Besides, the curves on the compression side appear a little higher than those on the tension side. These trends are the same as that appeared on the mild steel. In Fig. 6.4, the curve for the deformation along e_3-axis($\bar{I}_1(\boldsymbol{T}_e) \simeq \bar{I}_1(\boldsymbol{T}_\sigma)=0$, $\bar{I}_3(\boldsymbol{D}_e)\simeq\bar{I}_3(\boldsymbol{D}_\sigma)=0$) and that along e_2-axis($\bar{I}_1(\boldsymbol{T}_e)\simeq\bar{I}_1(\boldsymbol{T}_\sigma)=\sqrt{3}/2$, $\bar{I}_3(\boldsymbol{D}_e)\simeq\bar{I}_3(\boldsymbol{D}_\sigma)=0$) agree with each other almost completely. The trend mentioned above on the mild steel between the angles θ_e^* and θ_σ^* were recognized also for brass and aluminum alloy.

6. 1. 2. Proportional deformation in the space V_{3e}

Figure 6.6 shows the relation between $|\boldsymbol{\sigma}|$ and $|\boldsymbol{e}|$ in a plane e_2e_3 obtained for the mild steel S10C, where various symbols indicate the experimental results. As seen from the figure, the two experimental results obtained for each of the assigned trajectories agree well, and thus the solid curve is entered as an average thereof. The result of uniaxial tension ($\phi_e=0$, $\theta_e=90°$) is also entered for comparison. The curves $|\boldsymbol{\sigma}| \sim |\boldsymbol{e}|$ for the trajectories ($\phi_e=30°$, $\theta_e=30°$) and ($\phi_e=30°$, $\theta_e=60°$) are shown in Fig. 6.7 together with the curve for pure torsion ($\theta_e=0$) for comparison. These curves also differ from each other with the values of ϕ_e and θ_e, but the ordinate differences stay almost constant at large values of $|\boldsymbol{e}|$.

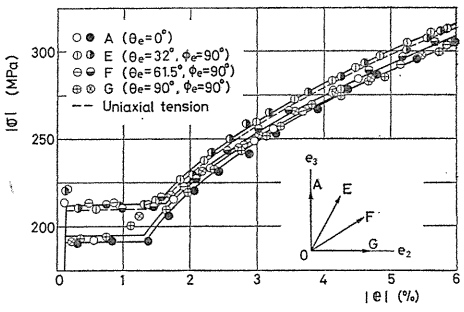

Fig. 6. 6 Relation between $|\boldsymbol{\sigma}|$ and $|\boldsymbol{e}|$ obtained from experiments A, E, F, G.

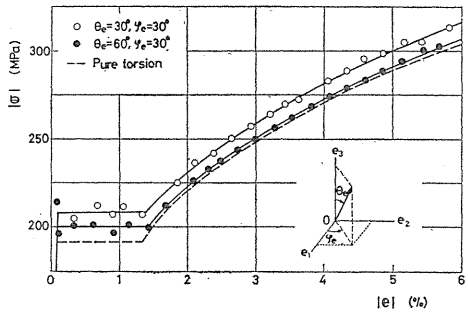

Fig. 6. 7 Relation between $|\boldsymbol{\sigma}|$ and $|\boldsymbol{e}|$ obtained from experiments.

6. 1. 3. Equi-strain curves

For the proportional deformation, $|\boldsymbol{e}|$ may be expressed as a scalar function of stress invariants:

$$|\boldsymbol{e}|=|\boldsymbol{e}|\{\bar{I}_1(\boldsymbol{T}_\sigma),\ |\boldsymbol{\sigma}|,\ \bar{I}_3(\boldsymbol{D}_\sigma)\}.$$

Thus, the solution of the above equation for $|\boldsymbol{\sigma}|$ is

$$|\boldsymbol{\sigma}|=|\boldsymbol{\sigma}|\{\bar{I}_1(\boldsymbol{T}_\sigma),\ |\boldsymbol{e}|,\ \bar{I}_3(\boldsymbol{D}_\sigma)\}. \tag{6.1}$$

It follows from (6.1) that the relation $|\boldsymbol{\sigma}| \sim |\boldsymbol{e}|$ is affected by $\bar{I}_1(\boldsymbol{T}_\sigma)$ and $\bar{I}_3(\boldsymbol{D}_\sigma)$. In order to make clear the effect of $\bar{I}_3(\boldsymbol{D}_\sigma)$ and to discuss that of $\bar{I}_1(\boldsymbol{T}_\sigma)$, equi-strain curves are described from the experimental results. Figure 6.8 shows an example of the equi-strain curves for mild steel S10C. In the figure, the small circles corresponding to the experimental results are connected by the solid curves. The dashed curves show Mises' circle passing through the experimental points in pure torsion ($\bar{I}_3(\boldsymbol{D}_\sigma)=0$) which correspond to the equi-strain curve without the effect of $\bar{I}_3(\boldsymbol{D}_\sigma)$.

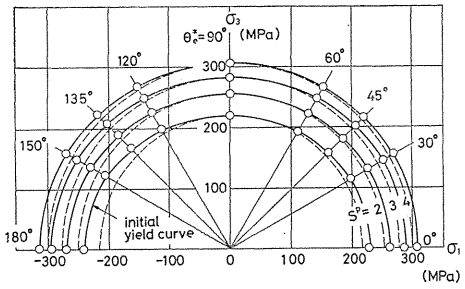

Fig. 6.8 Equi-strain curves for mild steel S10C.

These equi-strain curves may be approximated with high accuracy by the following ellipce:

$$\{\sigma_{11}(s)/\sigma(s)\}^2+[\sqrt{3}\sigma_{12}(s)/\{\sqrt{3}\tau(s)\}]^2=1. \tag{6.2}$$

By introducing a modifying coefficient

$$R_0=\sqrt{3}\tau(s)/\sigma(s), \tag{6.3}$$

the expression (6.2) is rewritten as follows:

$$\{R_0(s)\sigma_{11}(s)\}^2+\{\sqrt{3}\sigma_{12}(s)\}^2=\{\sqrt{3}\tau(s)\}^2, \tag{6.4}$$

where $\sigma(s)$ denotes the magnitude of the stress vector for uniaxial tension as a function of the arc length of the strain trajectory when the stress vector is in the first quadrant of the plane (σ_1, σ_3) and for the compression when the stress vector is in the second one, and $\sqrt{3}\tau(s)$ denotes that for the pure torsion.

Equation (6.4) expresses a circle in a modified space with coordinate axes $R_0(s)\sigma_{11}(s)$ and $\sqrt{3}\sigma_{12}(s)$, whose radius corresponds to a modified magnitude $|\boldsymbol{\sigma}^*|$ of the deviatoric stress vector. In the modified space, every curve $|\boldsymbol{\sigma}| \sim s$ obtained in the experiment may be reduced to a curve $|\boldsymbol{\sigma}^*| \sim s$ corresponding to pure torsion irrespective of the angle θ^*_σ. In other words, by eliminating the effect of $\bar{I}_3(\boldsymbol{D}_\sigma)$ from the experimental results, the deformation behaviour may be discussed as the relation between the second invariants of stress and strain deviators.

By expressing the modified magnitude $|\boldsymbol{\sigma}^*|$ as $R|\boldsymbol{\sigma}|$, the coefficient R is expressed as follows:

$$\begin{aligned} R=|\boldsymbol{\sigma}^*|/|\boldsymbol{\sigma}| &= \{(R_0\sigma_{11})^2+3\sigma_{12}^2\}^{1/2}/(\sigma_{11}^2+3\sigma_{12}^2)^{1/2} \\ &= \{1+(R_0^2-1)\sin^2\theta_\sigma\}^{1/2}. \end{aligned} \tag{6.5}$$

In the plane $(\sigma_{11}, \sqrt{3}\sigma_{12})$ with $\phi_\sigma=0°$, a solution of (4.33) satisfying the condition $-1\leq\bar{I}_3(\boldsymbol{D}_\sigma)\leq 1$ is obtained as follows:

$$\sin\theta_\sigma=-2\cos\{2\pi/3-(1/3)\arccos\bar{I}_3(\boldsymbol{D}_\sigma)\}. \tag{6.6}$$

By substituting (6.6) into (6.5), the following relation is obtained:

$$R=[1+4(R_0^2-1)\cos^2\{2\pi/3-(1/3)\arccos \bar{I}_3(\boldsymbol{D}_\sigma)\}]^{1/2}. \tag{6.7}$$

In the three-dimensional space $V_{3\sigma}$, the following expression is obtained by substituting (4.33) into (6.7):

$$R=[1+4(R_0^2-1)\cos^2[2\pi/3-(1/3)\arccos\{\sin^3\theta_\sigma\cos 3\phi_\sigma +3\sin\theta_\sigma\cos^2\theta_\sigma\cos(\phi_\sigma-\pi/3)\}]]^{1/2}, \tag{6.8}$$

where

$$R_0=\begin{cases} R_t=a(s)/b(s) & (0\leq \bar{I}_3(\boldsymbol{D}_\sigma)\leq 1), \\ R_c=a(s)/c(s) & (-1\leq \bar{I}_3(\boldsymbol{D}_\sigma)\leq 0), \end{cases}$$

and $a(s)$, $b(s)$ and $c(s)$ denote the values of stress vector for pure torsion, uniaxial tension and compression in relation to the arc length of the strain trajectory.

In the next, equi-strain curves in the deviatoric plane Π in the principal stress space are given in Fig. 6.9 on the basis of experimental results on mild steel S10C where the alphabetical symbols indicate the corresponding experiment shown in Table 6.1.

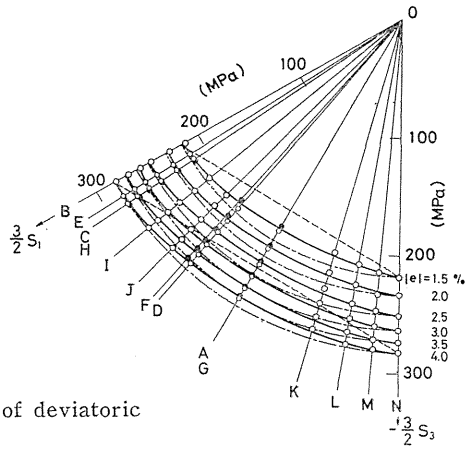

Fig. 6.9 Equi-strain curves in the plane Π of deviatoric stress.

Table 6.1 Directions of strain vector selected for experiment

Experiment	A	B	C	D	E	F	G	H	I	J	K	L	M	N
φ_e (deg.)	—	0	30	30	90	90	90	0	0	0	180	180	180	180
θ_e (deg.)	0	90	30	60	30	61.5	90	60	45	30	30	45	60	90

In the figure, the circles connected by solid curves show the experimental results, and the dash-dot curves (circular arcs) and the dashed ones (sides of normal hexagon) show the subsequent yield curves following the Mises and Tresca yield criteria, respectively. Figure 6.10 shows the relation between $\bar{I}_1(\boldsymbol{T}_\sigma)$ and $|\boldsymbol{e}|$ obtained from experimental results. In Fig. 6.9, the values of $|\boldsymbol{\sigma}|$ for experiments A and G($\bar{I}_3(\boldsymbol{D}_\sigma)=0$ for both cases) coincide well for the same values of $\bar{I}_3(\boldsymbol{D}_\sigma)$. On the other hand, the values of $\bar{I}_1(\boldsymbol{T}_\sigma)$ for experiments A and G given in Fig. 6.10 are quite different one another. Thus, it is clear that the relation between $|\boldsymbol{\sigma}|$ and $|\boldsymbol{e}|$ varies with $\bar{I}_3(\boldsymbol{D}_\sigma)$ but is little affected by $\bar{I}_1(\boldsymbol{T}_\sigma)$, and the systematic

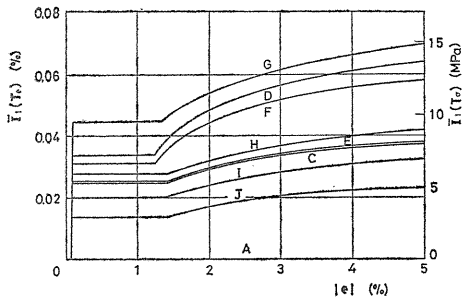

Fig. 6. 10 Relation between $\bar{I}_1(\boldsymbol{T}_\sigma)$ and $|\boldsymbol{e}|$.

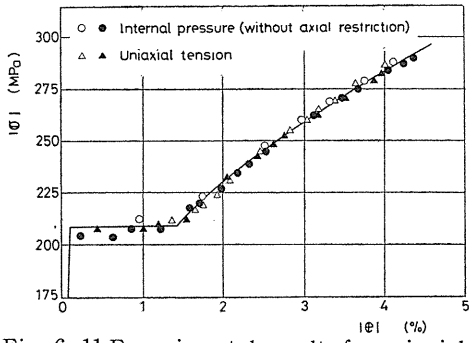

Fig. 6. 11 Experimental results for uniaxial tension and internal pressure (without axial restraint)

deviations of the experimental equi-strain curves from Mises' circle in Fig. 6.9 may be regarded as an effect due to $\bar{I}_3(\boldsymbol{D}_\sigma)$.

It may be concluded from Figs. 6.9 and 6.10 that the values of $\bar{I}_1(\boldsymbol{T}_\sigma)$ and $\bar{I}_3(\boldsymbol{D}_\sigma)$ in experiments C, E and H are closely similar although their principal stress directions are different. Consequently, the argument with $|\boldsymbol{\sigma}|$ for the same values of $|\boldsymbol{e}|$ in Fig. 6.9 serves to substantiate the initial isotropy of the material. On the other hand, the initial isotropy of the material used here has been ascertained already by experimental results for uniaxial tension and internal pressure (without axial restraint) on the specimen, the stress-strain curves agreeing well as shown in Fig. 6.11.

In Fig. 6.9, the equi-strain curves are located between the Mises' circle and the Tresca's hexagon, and the deviation from the latter increases with $|\boldsymbol{e}|$ whereas that from the former is almost constant irrespective of $|\boldsymbol{e}|$.

As an example of the modified results, adjusted values of the experimental results shown in Fig. 6.9 using (6.8) are shown with the open circles in Fig. 6.12, whereas the corresponding ones before modification are denoted with the solid circles. In the usual manner of expression applying in the plane II of the relation between the Mises and the Tresca yield criteria, the Mises circle passes through the vertices of the Tresca hexagon. On the other hand, remembering that the plastic behaviour is affected by $\bar{I}_3(\boldsymbol{D}_\sigma)$, both criteria should be related so that the Mises circle coincides with the Tresca hexagon at the center of each side of the latter where $\bar{I}_3(\boldsymbol{D}_\sigma)=0$, because the Mises circle corresponds everywhere to $\bar{I}_3(\boldsymbol{D}_\sigma)=0$, while the Tresca hexagon for which $\bar{I}_3(\boldsymbol{D}_\sigma)=0$ holds only at the center of each side, may be regarded as an extreme case of the effect of third invariant. Thus,

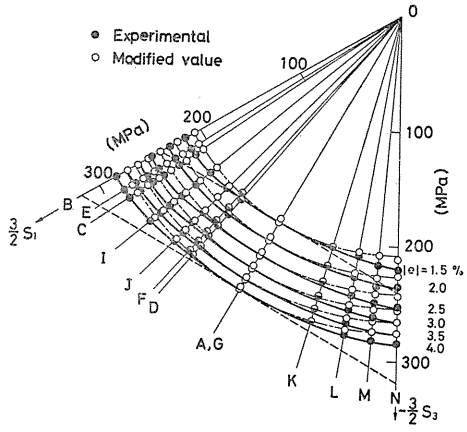

Fig. 6. 12 Modified results of experiments with parameter R.

unlike the conventional expression in Fig. 6.9, the Mises circle and the Tresca hexagon coincide at the center of each side of the latter in Fig. 6.12. Consequently, the fact that the experimental results indicated by the solid curve between the Mises circle and the Tresca hexagon are modified into the corresponding values shown with the open circles on the Mises circle may be regarded as an evidence that the effect of third invariant has been eliminated almost completely with the use of the coefficient R.

6. 2. Experimental results for orthogonal bi-linear strain trajectories

Bi-linear strain trajectory has been used most frequently for the experiment of complex loading, because it is the most fundamental case of the complex loading for which the history effect of deformation appears strongly just after the corner point. Here, the history effect just after the right-angled corner is discussed in detail for this case.

The plastic behaviour along the orthogonal bi-linear strain trajectory may be discussed in the three-dimensional local vector space of deviatoric stress $V_{3\sigma}$ shown in Fig. 6.13. In the figure, the length s_0 of the first branch corresponds to the pre-strain, $\Delta s(=s-s_0)$ shows a length of the second branch after the corner point, and $\boldsymbol{e}=e_i\boldsymbol{n}_i$, $d\boldsymbol{e}=de_i\boldsymbol{n}_i$ and $\boldsymbol{\sigma}=\sigma_i\boldsymbol{n}_i$ denote the strain, strain-increment and stress vectors, respectively.

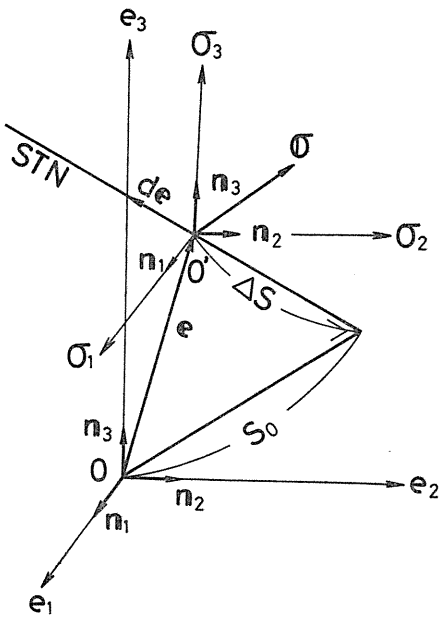

Fig. 6. 13 Local stress space $V_{3\sigma}(\sigma_1, \sigma_2, \sigma_3)$ on the orthogonal bi-linear trajectory in the space $V_e(e_1, e_2, e_3)$.

6. 2. 1. Experimental results for mild steel S10C

Experimental results are discussed for the deformations along the orthogonal bi-linear strain trajectories shown in Fig. 5.2 and Table 6.2, which are obtained by applying the combined loads of axial force, torque and internal pressure to the thin-walled tubular specimen of mild steel S10C. The pre-strain s_0 is fixed 2 percent, for which the history effect has been confirmed to be saturated sufficiently by

Table 6. 2 Orthogonal bi-linear strain trajectories ($s=2\%$)

Experiment		1A	2A	1B	2B	1C	2C	1D	2D	1E	2E
first branch	ϕ_e	0°	90°	90°	0°	0°	120°	0°	0°	0°	0°
	θ_e	0°	90°	90°	90°	0°	90°	45°	45°	0°	90°
second branch	ϕ_e	90°	90°	0°	90°	120°	120°	0°	0°	0°	0°
	θ_e	90°	0°	90°	90°	90°	0°	−45°	135°	90°	0°

preliminary tests. Strain rate is kept constant at $ds/dt=3\times10^{-6}/sec.$

6. 2. 1. 1. Curves $|\sigma| \sim \Delta s$

Curves obtained by the tests along the trajectories 1A and 2A through 1E and 2E are shown in Figs. 6. 14 through 6. 18. In these figures, the dashed and dash-dot

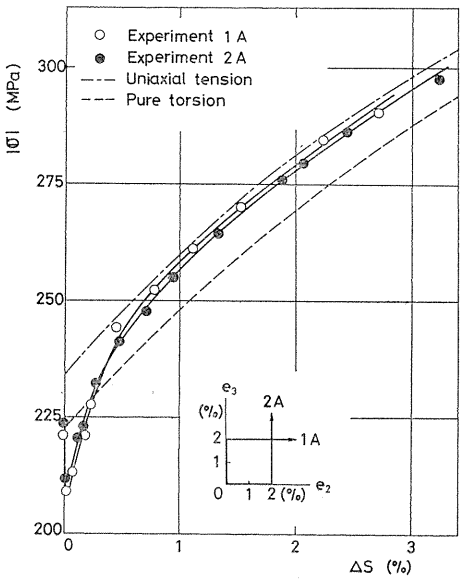

Fig. 6. 14 $|\sigma| \sim \Delta s$ curves obtained by 1A and 2A tests.

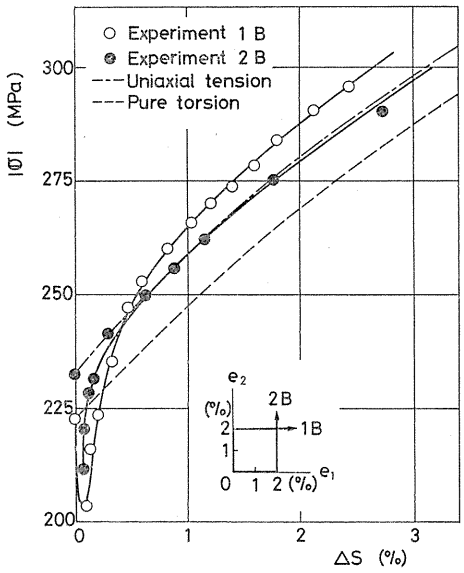

Fig. 6. 15 $|\sigma| \sim \Delta s$ curves obtained by 1B and 2B tests.

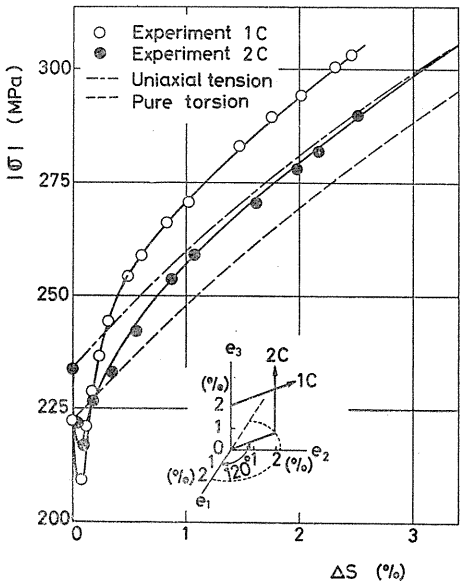

Fig. 6. 16 $|\sigma| \sim \Delta s$ curves obtained by 1C and 2C tests.

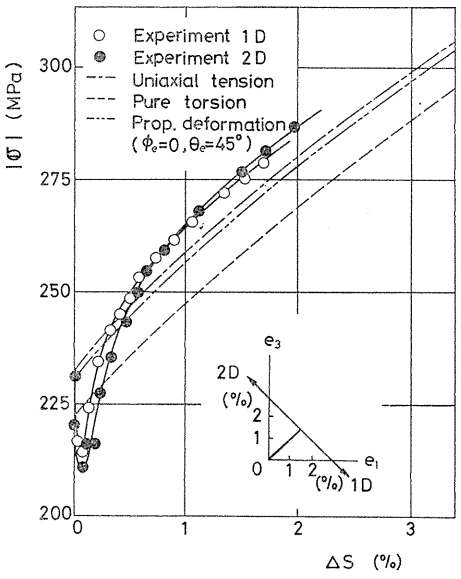

Fig. 6. 17 $|\sigma| \sim \Delta s$ curves obtained by 1D and 2D tests.

curves show the corresponding parts of the curves for torsion and tension, respectively. A sudden drop of $|\sigma|$ occurs just after the corner of trajectory in every experiment. This drop occurs for increasing strain at constant rate, and thus cannot be regarded as the so-called unloading which has been defined with decreasing strain in the quasi-static process. This might be attributable to a stress relaxation effect, because the strain at the corner due to the first branch persists, whereas the other strain component begins to increase along the second branch. However, when the second branch is not present, the decrease of stress has been ascertained to attain only about one-third of the total decrease obtained above. Moreover, from the results obtained for the bi-linear trajectory in e_2e_3-plane, this stress decrease may be found in the deformation in which the principal axes do not rotate through the first and second branches of trajectory. Therefore, this phenomenon may be ascribed to a microscopic instability of materials induced by a change in microscopic structures (release of dislocation piled up during pre-strain, for example) just after a sudden change in strain (or stress) state. In other words, the cummulative dislocation fixed during the deformation along the first branch is released due to the strain application in the direction of the second branch, and the resulting increase of plastic strain reduces the elastic part of the total strain which is increasing with constant rate. This may be related directly to the sudden drop of $|\sigma|$ mentioned above. The above-mentioned phenomenon may be regarded as a transient one and cannot be discussed by means of the flow rule on the premise of a quasi-static process. Such a phenomenon may be regarded as a similar one occuring just after the upper yield point of the mild steel.

As found from these figures, the curves $|\sigma| \sim \Delta s$ corresponding to the trajectories which are in the relation of mirror transformation in V_{3e} do not

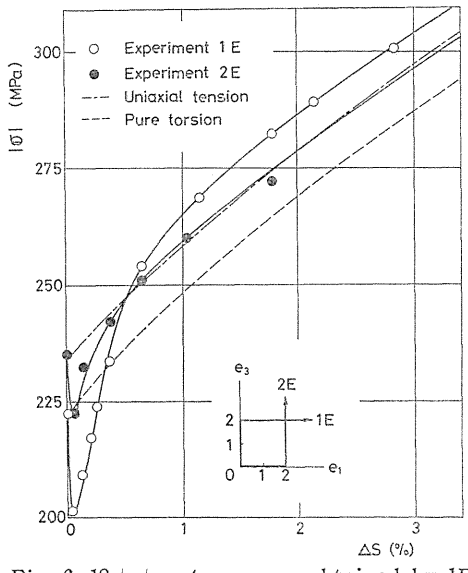

Fig. 6. 18 $|\sigma| \sim \Delta s$ curves obtained by 1E and 2E tests.

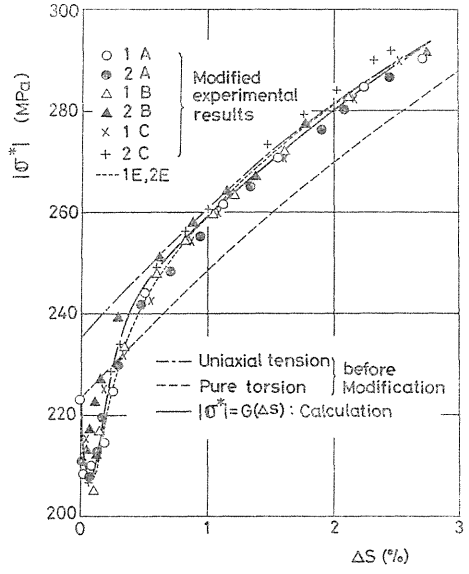

Fig. 6. 19 Modified curves $|\sigma^*| \sim \Delta s$ obtained by using the coefficient R for mild steel S10C.

always agree with each other. In line with the foregoing discussion, this may be attributed partly to the effect of $\bar{I}_3(\boldsymbol{D}_\sigma)$. For example, the curves for the second branch of trajectory agree well for the tests 1A and 2A along the axes e_2 and e_3 for which $\bar{I}_3(\boldsymbol{D}_\sigma)$ have the same value 0.

Figure 6.19 shows an example of the curve $|\sigma^*| \sim \Delta s$ modified by using the coefficient R in the previous section. As shown in Fig. 6.19, the remarkable difference observed between the curves for the trajectories in the relation of mirror transformation has disappeared and these curves may be reduced to an identical curve after modification.

6. 2. 1. 2. Angle θ between the strain-increment and stress vectors

In the results obtained by the tests of strain-controlled type, the direction of stress vector delays from that of the strain-increment vector $\boldsymbol{de}$ which coincide with the trajectory. An angle θ between the directions of $\boldsymbol{\sigma}$ and $\boldsymbol{de}$ is expressed by $\theta=\arccos(\boldsymbol{\sigma}\cdot\boldsymbol{de}/|\boldsymbol{\sigma}||\boldsymbol{de}|)$. The value of θ varies with increase of Δs. An example of the relation $\theta \sim \Delta s$ is shown in Fig. 6.20. As shown in the figure, the relation may be approximated by a unique curve for every trajectory.

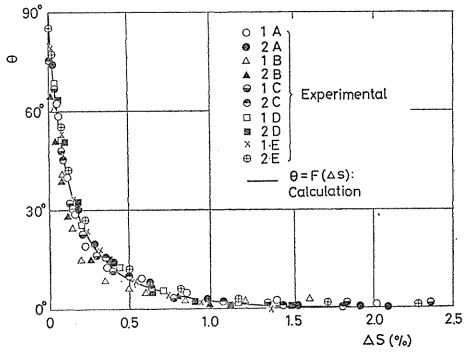

Fig. 6. 20 Relation between θ and Δs for mild steel S10C.

6. 2. 2. Experimental results for brass[22]

Figure 6.21 shows the curves $|\sigma| \sim s$ obtained by the tests along the bi-linear strain trajectories shown in the inserted figure. The tests A, B, C and D have pre-strains $s_0=0.66$, 1.165, 2.20 and 3.20 percent in total value, which correspond to the plastic pre-strain $s_0{}^p=0.5$, 1.0, 2.0 and 3.0 percent, respectively. The test C′ has a tajectory which is a mirror transformation of that for the test C. In the same figure, the curves $|\sigma| \sim s$ for tension and torsion are indicated by the dash-dot and dashed ones, respectively.

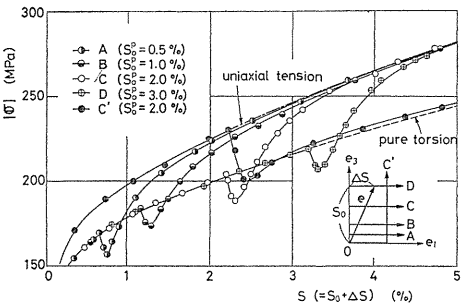

Fig. 6. 21 $|\sigma| \sim s$ curves for deformation along the orthogonal bi-linear strain trajectories A, B, C, D and C′.

As shown in the figure, stress value suddenly drops for brass after the corner and increases afterwards. As opposed to mild steel, after the recovery from the drop in $|\sigma|$, the curves $|\sigma| \sim s$ for brass tend to agree with the curve of proportional deformation corresponding to the stress state in the second branch. For example, the curves after the recovery in the tests A through D tend to agree with the curve of tension, while the curve after recovery in the C′ test almost tend to agree with that of torsion. Figure 6.22 shows the modified curves $|\sigma^*| \sim s$ obtained by using the parameter R from

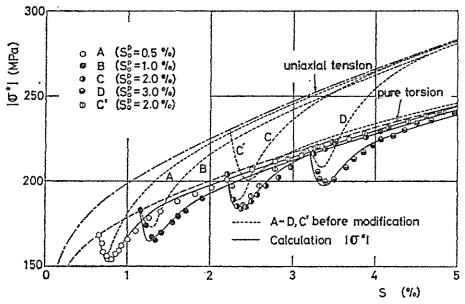

Fig. 6. 22 Modified curves $|\sigma^*| \sim s$ obtained by using the coefficient R for brass BsBM2.

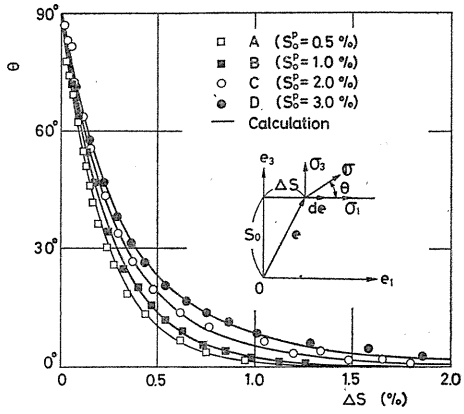

Fig. 6. 23 Relation between the angle of delay θ and Δs.

the curves $|\sigma| \sim s$ shown in Fig. 6.21. In the figure, the experimental curves before modification are shown with the dashed curves for the tests A through D and the test C′. As found from the figure, modified curves for the tests C and C′, whose trajectories are in the relation of mirror image, agree well with each other after modification.

In Fig. 6.23, the angle of delay θ in the direction of stress vector from that of strain-increment vector is shown in relation to the arc length Δs. The value of θ decreases to 0 at about 2 percent of Δs. The decreasing rate is small for a large value of pre-strain, but the effect of pre-strain is not so significant.

6. 2. 3. Experimental results for aluminum alloy[23]

Figures 6.24 and 6.25 show the curves $|\sigma| \sim s^p$ obtained by the tests of torsion after tension (T−S) and tension after torsion (S−T) for the deformations along orthogonal bi-linear trajectories in the plane-e_1e_3.

The value of plastic pre-strain $s_0{}^p$ corresponding to the corner is entered on the trajectories in the inserted figure. In these figures, the curves $|\sigma| \sim s^p$ for tension and torsion are shown with the dashed and dash-dot curves. In Fig. 6.24

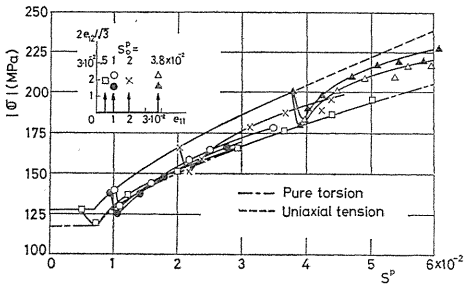

Fig. 6. 24 $|\sigma| \sim s^p$ curves of aluminum alloy 5056 for torsion after tension.

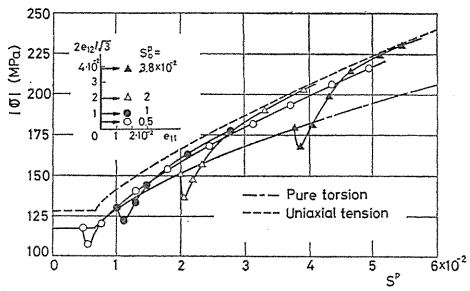

Fig. 6. 25 $|\sigma| \sim s^p$ curves of aluminum alloy 5056 for tension after torsion.

showing the curves $|\sigma| \sim s^p$ for T − S, the curve after the corner for $s_0{}^p=0.5$ percent almost agree with that for torsion after the recovery of sudden drop in $|\sigma|$. However, those curves for $s_0{}^p>1$ percent appear higher with increase of $s_0{}^p$ after recovery of sudden drop of $|\sigma|$. On the contrary, the curves $|\sigma| \sim s^p$ after the corner for S−T tend to a certain curve after the recovery, which is parallel with that for tensison, for every value of s^p (Fig. 6.25).

Modified curves $|\sigma^*| \sim s^p$ obtained from the curves $|\sigma| \sim s^p$ shown in Figs. 6.24 and 6.25 by means of the coefficient R are shown in Fig. 6.26 with the dashed curves (T−S) and solid curves (S−T). As shown in the figure, the above-mentioned difference in the history effect after the corner between the trajectories, which are mirror image with each other, still remains after eliminating the effect of $\bar{I}_3(\boldsymbol{D}_\sigma)$. In other words, for the geometry of trajectories, the history effect after the corner for aluminum alloy depends on the orientation of trajectory in the space V_{3e}.

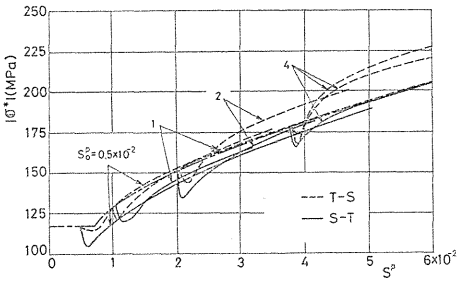

Fig. 6.26 Modified curves $|\sigma^*| \sim s^p$ for aluminum alloy.

Since the postulate of isotropy cannot be satisfied for aluminum alloy even after eliminating the effect of $\bar{I}_3(\boldsymbol{D}_\sigma)$, in order to formulate the deformation dehaviour of such materials under complex laoding accurately, it is necessary to take into account a parameter relating the orientation of strain trajectory in the space V_{3e}.

Judging from the above discussion for history effect, the material such as mild steel or brass may be classified as orientation-insensitive material and aluminum alloy as orientation-sensitive one in the space V_{3e}. These trends might be attributed to a difference in the aging effects due to the deformations along the trajectories T−S and S−T, which is remarkable for aluminum alloy.

6. 3. Experimental results for non-orthogonal bi-linear trajectories

The effect of corner angle θ_0 on the plastic behaviour is discussed. Figure 6.27 shows the curve $|\sigma| \sim s$ obtained for the deformation of the mild steel S10C along the trajectories shown in the inserted figure. It may be seen from the figure that $|\sigma|$ increases after the corner, initially departing from the hardening curve for torsion, but tending to be parallel to it at the last stage. By comparing the results of the corresponding deformation along the orthogonal bi-linear trajectories with these curves, it is found that the drop of stress value just after the corner does not appear significantly for $\theta_0<60°$. However, it should be noted that the curve for $\theta_0=-60°$ is higher than that for $\theta_0=-90°$ after recovery. Moreover, it is found that these curves coincide with each other for the same value of θ_0 irrespective of the value of s_0. This shows the saturation of the history effect for $s_0>2$ percent. Figure 6.28 shows the results obtained for the deformations along the trajectories shown in the inserted figure, which are in the relation of mirror images of those shown in Fig. 6.27. It may be seen from Fig. 6.28 that in this case $|\sigma|$ behaves in a similar fashion to that exhibited in Fig. 6.27. However, the increase of $|\sigma|$ are not as large as those of Fig. 6.27 and all curves coincide with a curve parallel to the one for tension, irrespective of the value of θ_0. These

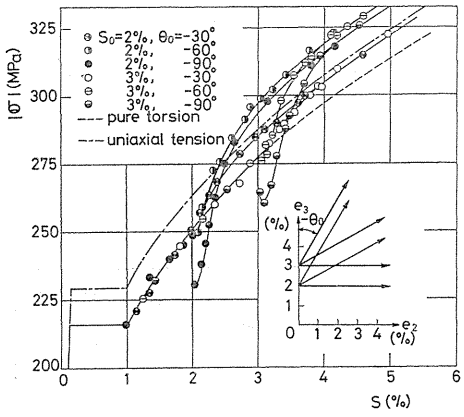

Fig. 6. 27 $|\sigma| \sim s$ curves of mild steel S10C for bi-linear trajectories with $\theta_0 = -30°$, $-60°$ and $-90°$.

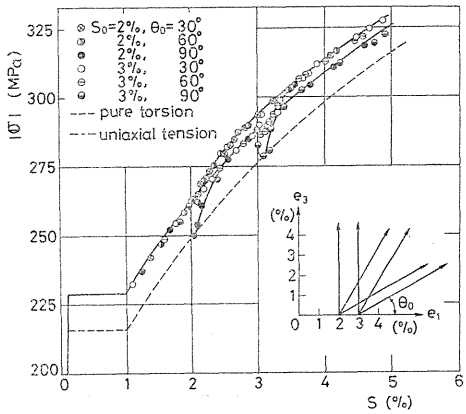

Fig. 6. 28 $|\sigma| \sim s$ curves of mild steel S10C for bi-linear trajectories with $\theta_0 = 30°$, $60°$ and $90°$.

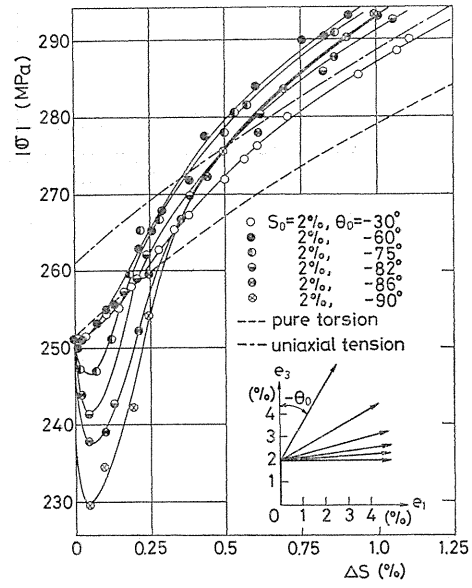

Fig. 6. 29 $|\sigma| \sim \Delta s$ curves of mild steel S10C for bi-linear trajectories with various values of $-\theta_0$.

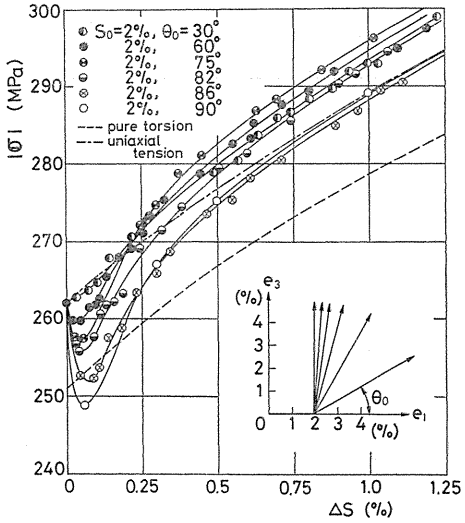

Fig. 6. 30 $|\sigma| \sim \Delta s$ curves of mild steel S10C for bi-linear trajectories with various values of θ_0.

results show that in this case, θ_0 only has a small effect on the hardening curve after the corner on the trajectory.

In order to clarify the effect of θ_0 on this behaviour of $|\sigma|$, relevant parts of Figs. 6. 27 and 6. 28 are again shown in Figs. 6. 29 and 6. 30 in detail, together with the results of supplementary tests. It may be seen from these figures that, although the drop of $|\sigma|$ is negligibly small for $|\theta_0| < 60°$, it increases with an

increase in θ_0 for $|\theta_0|>60°$.

Figure 6.31 shows the curves $|\sigma^*|\sim s$ obtained by modifying the results shown in Figs. 6.27 and 6.28 by means of the coefficient R_0. In the figure, the curves corresponding to the trajectories for the same value of $|\theta_0|$ in the inserted figure also coincide well, which appeared quite differently before modification. In other words, the different trends appeared on the deformations along the trajectories being mutually mirror images may be attributed to the effect of $\bar{I}_3(\boldsymbol{D}_\sigma)$ almost.

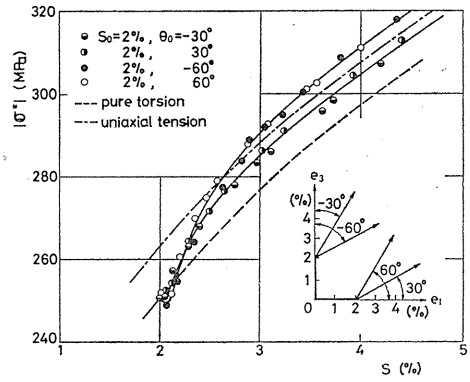

Fig. 6.31 Modified results $|\sigma^*|\sim \Delta s$ of mild steel S10C for bi-linear trajectories with $\theta_0=\pm30°$ and $\pm60°$.

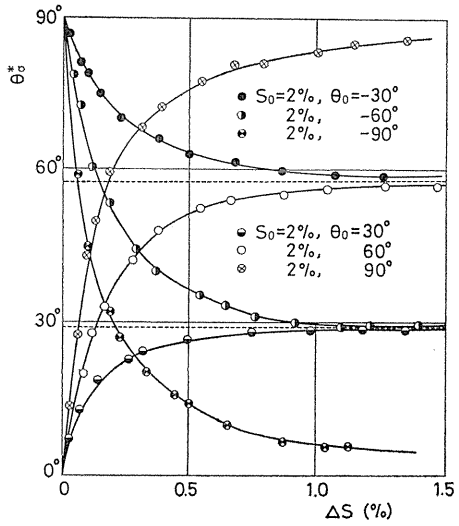

Fig. 6.32 Variation of modified angle of delay θ_σ^* after the corner.

Figure 6.32 shows the variation in the modified value θ_σ^* by using the coefficient R_0 after the corner. As found from the figure, the curves $\theta_\sigma^*\sim\Delta s$ for each pair of trajectories having the same values of θ_0 and $-\theta_0$ are symmetric with respect to the direction 45°, to within a high degree of accuracy. The dashed lines in the figure, showing $\theta_\sigma^*=57°$ and 29°, correspond to the directions of stress vector for proportional deformation with $\theta_e=60°$ and 30°.

It may be seen that for the cases $|\theta_0|=30°$ and 60°, θ_σ^* after the corner does not tend to θ_{de} in the corresponding proportional deformation, but to the angles 29° and 57°, respectively. These discrepancies are small, however, and if they are neglected, the relation between θ_σ^* and Δs in these experiments are sensibly symmetrical with respect to the direction 45°.

6. 4. Experimental results for orthogonal bi-linear strain trajectory with rounded corner[24]

Experiment investigating the history effect on the deformation behaviour along the orthogonal bi-linear strain trajectory with rounded corner was performed on the brass BsBM2.

The trajectories shown in Fig. 6.33 a consist of the first branch of tensile prestrain as much as $e_1=1.5$ percent and the second branch of trosional strain e_3

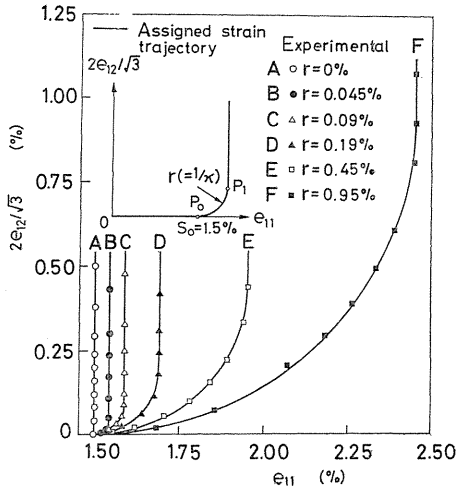

Fig. 6.33 a Strain trajectories with rounded corner in the space V_{2e}.

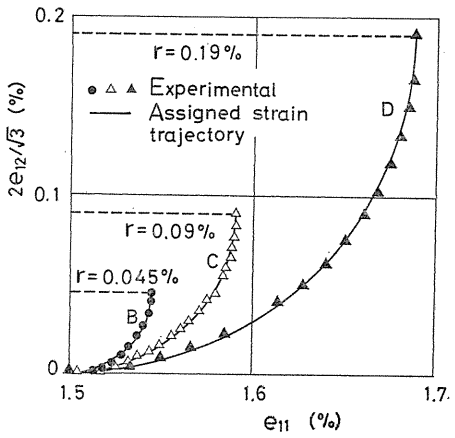

Fig. 6.33 b Details at the corner part in the trajectories B, C and D.

changing through a quarter circle in the vector space V_{2e}. Values of the radius of the quarter circle were selected as $r=0$, 0.045, 0.09, 0.19, 0.45 and 0.95 percent. The strain rate along the trajectory was selected also as $ds/dt=3\times10^{-6}$/sec.

For the procedure of controlling displacement along the rounded corner of the trajectory, curves showing the variation with time of the axial and angular displacements over the gauge length of specimen were described on each corresponding sheet around the drums rotating with constant speed respectively and traced by reading heads of photo-electronic type.

Experimental results concerning the geometry of the strain trajecotry are plotted in Fig. 6.33 a and compared with the corresponding curves showing the assigned geometries. Figure 6.33 b shows the relations between the experimental results and the assigned curves in more detail. From these figures, it may be seen that the assigned geometry of the strain trajecotry has been reproduced well in the experiment.

Figure 6.34 shows the curves $|\sigma^*|\sim\Delta s$ after the end-point P_0 of the first branch obtained by modifying the experimental results by means of the coefficient R_0 for eliminating the effect of $\bar{I}_3(\boldsymbol{D}_\sigma)$ for every radius of the rounded corner. In the figure, the dashed curve obtained under pure torsion of the specimen of this type is entered for comparison. According to the meaning of the modifying coefficient R_0, the curve under tension should coincide with the dashed curve after eliminating the effect of the third invariant. As found from this figure, the effect of curvature of trajectory on the relation $|\sigma^*|\sim\Delta s$ has

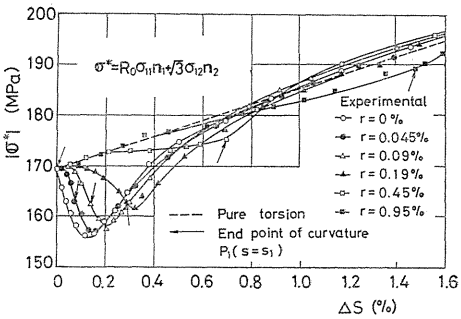

Fig. 6.34 Relations between $|\sigma^*|$ and the arc length after the beginning of rounded corner Δs.

the following features:

(i) A significant decrease of $|\sigma^*|$ with the increase of Δs at constant rate, which occured just after the corner point ($r=0$), also occurs even when the strain state changes continuously from tension to torsion through the rounded corner.

(ii) If the magnitudes of the stress vector for the deformation along the trajectory after the beginning of the rounded corner of radius r and the stress vector for that under torsion are expressed as $|\sigma^*|(\Delta s\,;\,r)$ and $|\sigma^*|(\Delta s\,;\,\infty)$ respectively, then the difference between them, viz.

$$\Delta|\sigma^*|(\Delta s\,;\,r)=|\sigma^*|(\Delta\,;\,\infty)-|\sigma^*|(\Delta s\,;\,r) \tag{6.9}$$

may be taken as a value for estimating the effect of the radius of curvature on the $|\sigma^*|(\Delta s\,;\,r)$. As found from Fig. 6.34, the maximum value of $\Delta|\sigma^*|(\Delta s\,;\,r)$ is the larger the smaller value of r, and the value of $\Delta|\sigma^*|(\Delta s\,;\,r)/|\sigma^*|(\Delta s\,;\,r)$ attains as much as 8 through 10 percent for the experimental results in the range $r\leq 0.19$ percent.

(iii) Though the maximum value $\Delta|\sigma^*|_{max}$ occurs after the end-point $P_1(s=s_1)$ of the rounded corner (shown by the arrow in the figure) for small value of r, the location where $\Delta|\sigma^*|_{max}$ occurs approaches the point P_1 with increase of r and almost coincides with the point P_1 for $r\geq 0.45$ percent.

(iv) The effect of curvature is not regarded as occuring for $\Delta|\sigma^*|=0$. According to the experimental results, though the value of $\Delta|\sigma^*|$ is different from zero even when the value of r is fairly large, the effect of curvature may be regarded as sufficiently small for $r=0.95$ percent since the value of $\Delta|\sigma^*|/|\sigma^*|$ reduces to less than 2 percent.

(v) The value of $\Delta|\sigma^*|$ may be regarded as tending to zero in every experiment for the development of deformation along the second branch after the rounded corner. This shows the decline of the effect of curvature on the subsequent deformation.

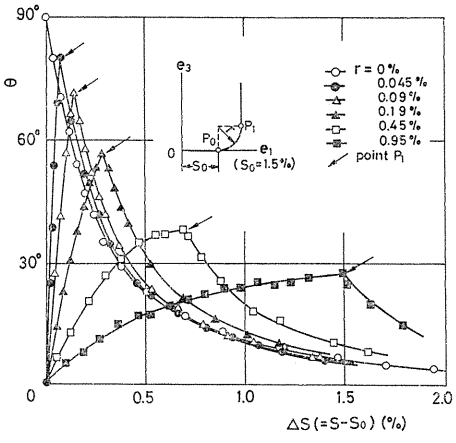

Fig. 6.35 Relation between θ and Δs.

Figure 6.35 shows the relation between the angle of delay $\theta(=\theta_{de}-\theta_\sigma)$ and Δs obtained from the experiment for every value of the radius of curvature r. The effect of curvature of the trajectory on the relation $\theta\sim\Delta s$ is found from Fig. 6.35 as follows.

The value of θ increases with the increase of Δs and attains a very large value for a small value of r, but decreases quickly at first and slowly afterwards after the end-point P_1 of the rounded corner, and tends to zero with the increase of Δs.

6. 5. Experimental results for orthogonal tri-linear strain trajectory

6. 5. 1. Strain trajectories in two-dimensional vector space[25]

Experiment was carried out to discuss the history effect and its fading feature

on the plastic deformation along orthogonal tri-linear strain trajectories. As the tri-linear trajectory may develop in two or three dimensional vector space, the experiment was performed at first for that contained in the two-dimensional one, for discussing the history effect of first corner on the second one leading to loading or unloading.

A series of complex loadings of axial force and torque were applied to a thin-walled tubular specimen of brass BsBM2. The specimen was finished from a bar of brass carefully annealed (furnace cooled after soaking at 650° for 8 hours) so that the material may have a sufficient isotropy.

Table 6.3 shows the configurations of strain trajectory used in the experiment, which correspond to Fig. 5.3 a.

Table 6. 3 Tri-linear strain trajectory

Strain trajec.	s_0 ($s_0{}^p$)	s_1 ($s_1{}^p$)	last load
F	1.5 % (1.32%) T		C
G	1.5 % (1.32%) T	0.25% (0.13%) S	T
H	1.5 % (1.32%) T	0.5 % (0.35%) S	T
I	1.5 % (1.32%) T	1.0 % (0.83%) S	T
J	1.5 % (1.32%) T	2.0 % (1.82%) S	T
K	1.5 % (1.32%) S	1.0 % (0.83%) T	S
L	2.38% (2.17%) S		T
M	3.35% (3.14%) S		T
N	1.5 % (1.32%) T	0.25% (0.13%) S	C
P	1.5 % (1.32%) T	0.5 % (0.35%) S	C
Q	1.5 % (1.32%) T	1.0 % (0.83%) S	C
R	1.5 % (1.32%) T	2.0 % (1.82%) S	C
U	1.5 % (1.32%) S	0.5 % (0.35%) T	S

In the table, s_0 or s_1 denotes the length of the first or second branch, and the symbols T, S and C express the tests under tension, torsion and compression, respectively. Moreover, the superscript p shows the plastic part of the corresponding quantity. The strain rate along the trajectory was kept constant at $ds/dt = 3\times10^{-6}$/sec.

The stress vector σ obtained from the experiments after the second corner of trajectories G through J and those N, P, Q and R shown in Table 6.3 are shown in Figs. 6.36 a and 6.36 b. In these figures, the solid lines, the short segments with arrow and the small solid circles with symbol represent the strain trajectories, the stress vectors and their starting points, respectively. Moreover, the dashed curves express the corresponding plastic strain trajectories obtained by subtracting the elastic part with the use of Hook's law from each strain component obtained by the experiment. The small open circles with symbol on these dashed curves correspond to the above-mentioned solid circles. The symbols attached to these small circles are ommited just after the corner for avoiding complication. As found from these figures, the direction of σ after the second corner tends quickly to the tangential direction of the strain trajectory along the third branch, and the effects

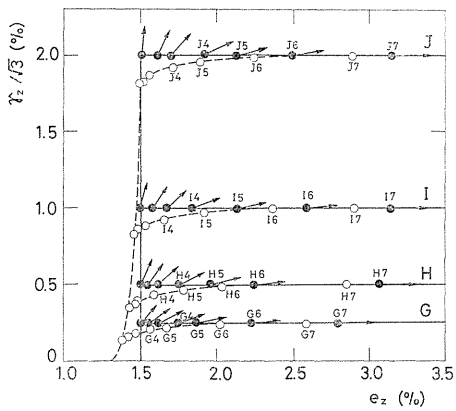

Fig. 6.36 a Variations of stress vector σ after the second corner (trajectories G through J).

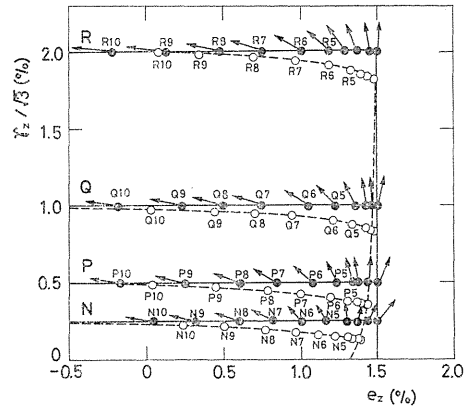

Fig. 6.36 b Variations of stress vector σ after the second corner (trajectories N, P. Q and R).

of two right-angled corners decline with the development of plastic deformation along the third branch. In what follows, the features of decline in history effect will be discussed on the magnitude $|\sigma|$ and the direction θ_σ of the stress vector in relation to the increase of strain after the second corner.

6. 5. 1. 1. Magnitude of stress vector

Figure 6.37 shows the relation between $|\sigma|$ and s^p obtained by the experiments for the plastic deformation along the trajectories G through M with various symbols. As shown in the inserted figure, the trajectory K is a mirror image of the trajectory I, and the trajectories L and M are the bi-linear trajectories corresponding to the trajectories I and J in which the length of each first branch corresponds to the sum of the lengths of the first and second branches of the trajectories I and J, respectively.

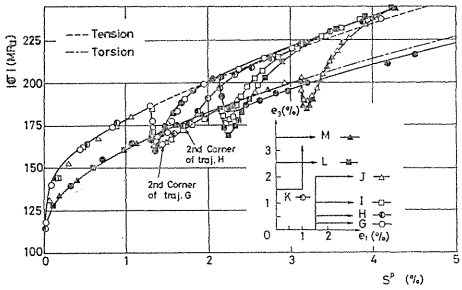

Fig. 6. 37 $|\sigma| \sim s^p$ curves of brass BsBM2 for the trajectories G through M.

In the experimental result along the trajectory J shown in the figure, the magnitude $|\sigma|$ decrease suddenly jusr after the first corner, but increases again and tends to lie on the curve under torsion with an increase of plastic arc length s^p. This trend may be related with the fact that the second branch develops under torsion, and it shows the decline in the effect of first corner on the magnitude $|\sigma|$ along the second branch.

As found from the experimental results along the trajectories G through J, each of the magnitude $|\sigma|$ after the second corner tends to lie on the curve under uniaxial tension with an increase of s^p. Such a trend may also be related with the fact that the third branch develops under uniaxial tension. To be more specific, the effect due to the two corners of trajectory on the magnitude $|\sigma|$ declines with

an increase of s^p after the second corner, and the magnitude $|\sigma|$ tends to lie on the curve under uniaxial tension. The state of decline in the effect of first corner on the plastic behaviour along the third branch may be understood in more detail by analysing the variation of magnitude $|\sigma|$ after the second corner. In the trajectory G or H having a short length of second branch s_1, a sudden decrease of $|\sigma|$ just after the second corner does not apper remarkably because the effect of first corner does not decline sufficiently. On the other hand, as found from the relation along the trajectory I or J, a sudden decrease of $|\sigma|$ after the second corner comes to appear with a decline in the effect of first corner accompanying the increase of s_1.

This feature becomes more clear from the comparison of the trajectories I, J and L, M. The sudden decrease of $|\sigma|$ after the second corner on the trajectory I is less remarkable than that on the trajectory L, and it shows that the effect of first corner on the trajectory I does not decline sufficiently even after the length of second branch $s_1=1$ percent ($s_1{}^p=0.83\%$). On the other hand, the sudden decrease of $|\sigma|$ just after the second corner on the trajectory J($s_1=2\%$, $s_1{}^p=1.82\%$) agree well with that just after the corner on the trajectory M. This may be taken as an experimental evidence that the effect of first corner on the magnitude $|\sigma|$ has vanished in the plastic behaviour along the third branch. Thus the variation of $|\sigma|$ along the third branch for a trajectory having the value $s_1=2$ percent ($s_1{}^p=1.82\%$) may be regarded as that of the bi-linear trajectory M having only the torsional pre-strain $s^p(=s_0{}^p+s_1{}^p)=3.14$ percent.

Though the trajectory K is a mirror image of the trajectory I, the relation along the third branch of the former differs from that of the latter, and thus it seems that the special postulate of isotropy does not hold in this case. This may be attributed to the effect of third invariant $\tilde{I}_3(\boldsymbol{D}_\sigma)$ discussed in Section 6.1.3. Then, the relation will be modified by using the coefficient R_0 for eliminating the effect of third invariant in the same way as in Section 6.1.3. The relation between the magnitude after the modification $|\sigma^*|$ and s^p are shown in Fig. 6.38. As found from the figure, the relations between $|\sigma^*|$ and s^p for the trajectories I and K agree well with each other. Thus, it may be concluded that the method of eliminating the effect of $\tilde{I}_3(\boldsymbol{D}_\sigma)$ from the experimental result by using the coefficient R_0 is available for tri-linear trajectory, and that the special postulate of

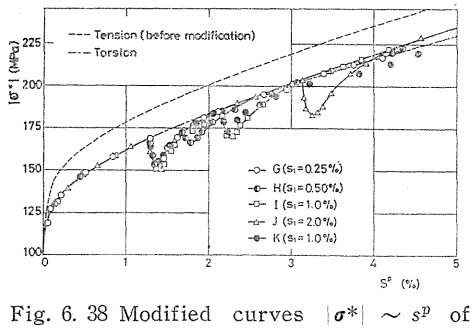

Fig. 6.38 Modified curves $|\sigma^*| \sim s^p$ of brass BsBM2 for the trajectories G through K.

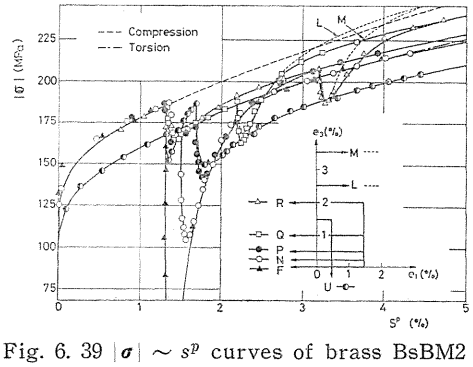

Fig. 6.39 $|\sigma| \sim s^p$ curves of brass BsBM2 for the trajectories F, N, P, Q, R and U.

isotropy holds also in this case with high accuracy after eliminating the effect of $\bar{I}_3(\boldsymbol{D}_\sigma)$ from experimental results.

Accordingly, it may be said that the relation $|\sigma^*| \sim s^p$ can be determined by the shape of trajectory within the range $s^p = 1.8$ percent preceding the point considered on the trajectory.

Figure 6.39 shows the relation $|\sigma| \sim s^p$ obtained from the experiments along the trajectories F, N, P, Q, R and U. As found from the figure, the sudden decrease of $|\sigma|$ just after the second corner, unlike in the above-mentioned example for the trajectories G through J, becomes less remarkable for larger value of s^p. Moreover, the magnitude $|\sigma|$ approaches that for the curve under uniaxial compression (this curve coincides with that under uniaxial tension) with an increase of s^p, but these values cannot be said to agree perfectly. This trend reflects the softening of material (Bauschinger effect) accompanying the unloading on the trajectory F with $\theta = 180°$.

On the trajectories N and P with a short length of the second branch s_1, the magnitude $|\sigma|$ does not agree with that for the curve under uniaxial compression, because the trajectories N and P are akin to the trajectory F and a sufficient strain hardening does not appear with an increase of arc length after the second corner. However, the effect of first corner declines with an increase of s_1, the softening effect becomes less remarkable, and the magnitude $|\sigma|$ after the second corner of these trajectories seems to approach that on the curve under uniaxial compression, just in the same way as for the bi-linear trajectories L and M.

As found from the figure, the magnitude $|\sigma|$ after the first corner almost agrees with the curve under torsion, and the behaviour of $|\sigma|$ after the second corner on the trajectory Q or R, in which the effect of first corner may be supposed to have vanished, approaches that of dashed curve of orthogonal bi-linear trajectory L or M, while the magnitude $|\sigma|$ for the former appears a little lower than that for the latter.

Judging from this trend, though the effect of the shape of trajectory on the magnitude $|\sigma|$ has vanished apparently after the first corner, something similar to Bauschinger effect may be said to persist more or less. In other words, when the direction of de is reversed on the trajectory such as on the trajectories N, P, Q and R, the above-mentioned principle of fading memory cannot be said to hold perfectly even for a sufficiently long s_1.

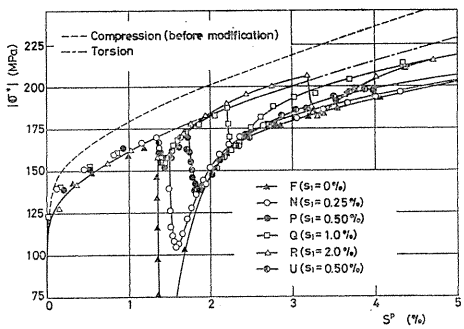

Fig. 6. 40 Modified curves $|\sigma^*| \sim s^p$ of brass BsBM2 for the trajectories F, N, P, Q, R and U.

Though the trajectories U and P lie in the relation of mirror image, the corresponding relations $|\sigma| \sim s^p$ are different from each other because of the effect of $\bar{I}_3(\boldsymbol{D}_\sigma)$. However, these relations may be modified by using the coefficient R_0 into an identical relation $|\sigma^*| \sim s^p$ shown in Fig. 6.40 with various symbols. From this result, it is found that the special postulate of isotropy may hold with high accuracy after eliminating the effect of $\bar{I}_3(\boldsymbol{D}_\sigma)$ from the experimental result by using the coefficient R_0 even when the direction of de is reversed on the trajectory.

6. 5. 2. Strain trajectory in three-dimensional vector space[26]

Plastic behaviours of mild steel S15C along the orthogonal tri-linear strain trajectories were examined as the most fundamental example of three-dimensional strain trajectories. Figure 6.41 shows the tri-liner trajectories in the three-dimensional vector space, where a length s_0 of the first branch was kept constant at s_0 $=2$ percent and the deformation along the third branch was realized under combined loadings of compression and torsion in the direction of an angle θ_e from the axis e_3 in the plane-e_1e_3 which is perpendicular to the second branch. Seven values of the angle $\theta_e(=0°, 30°, 60°, 90°, 120°, 150°$ and $180°)$ together with four lengths of the second branch $s_1(=0, 0.25, 0.5$ and 1.0%, s_1: a length along the second branch) were selected in the experiment. A strain rate along each of these trajectories was kept constant at $ds/dt=3\times10^{-6}$/sec.

Figures 6.42 through 6.44 show the curves $|\sigma^*|\sim s$ for $s_1=0$, 0.25 and 1.0 percent obtained by modifying the experimental results by means of the coefficient R. In these figures, the dash-dot and dashed curves show the results of compression and torsion tests before modification, respectively. In every figure, the magnitude $|\sigma^*|$ decreases suddenly just after the point B(point A for $s_1=0\%$). However, the decrease is recovered and

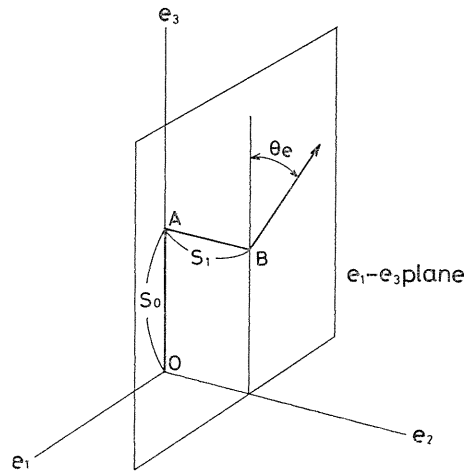

Fig. 6. 41 Orthogonal tri-linear strain trajectories in three-dimensional vector space V_{3e}.

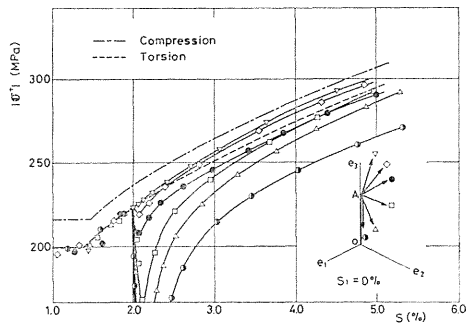

Fig. 6. 42 Modified curves $|\sigma^*|\sim s$ of mild steel S15C for $s_1=0\%$.

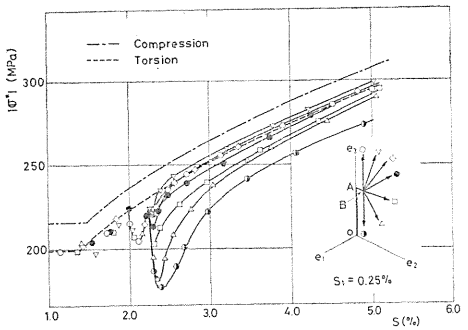

Fig. 6. 43 Modified curves $|\sigma^*|\sim s$ of mild steel S15C for $s_1=0.25\%$.

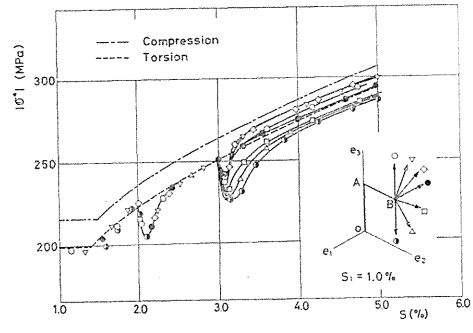

Fig. 6. 44 Modified curves $|\sigma^*|\sim s$ of mild steel S15C for $s_1=1.0\%$.

the curve tends to become parallel with the dashed one. Moreover, such a trend varies quantitatively in a wide range with respect to the values of angle θ_e.

In the case of $s_1=0$ percent, the magnitude $|\sigma^*|$ decreases little after the point A for $\theta_e=30°$. However, the decrease becomes to appear significantly with an increase of θ_e. Though every curve for $\theta_e<120°$ tends to lie on the dashed curve after the recovery, the curves for $\theta_e=150°$ and $180°$ tend to parallel with, but fairly lower than, the dashed one.

In the case of $s_1=0.25$ percent (Fig. 6.43), the starting point B of the third branch is situated on a way of recovery from the drop of $|\sigma^*|$ after the point A. Thus, though the drop of $|\sigma^*|$ just after the point B due to the effect of first branch differs fairly remarkably in relation to the angle θ_e, an extent of drop decreases in comparing with that after the point A for the case of $s_1=0$ percent, especially for $\theta_e>90°$. This shows a quick decline, in the early period of second branch, of the history effect of first branch on the deformation along the third one.

In Fig. 6.44 corresponding to the case of $s_1=1.0$ percent, the starting point B of the third branch lies on the dashed curve after the recovery of the drop of $|\sigma^*|$, and the effect of θ_e becomes sufficiently weak in comparing with the case of $s_1=0.25$ percent. In other words, the curve corresponding to each value of θ_e lies very close to that for $\theta_e=90°$.

As an index for estimating quantitatively the history effect, a ratio of deviation $r_1=(|\sigma^*|-|\sigma^*|_t)/|\sigma^*|_t$ of the magnitude $|\sigma^*|$ from the corresponding magnitude $|\sigma^*|_t$ on the dashed curve is shown in Table 6.4 at a point after the start of the last branch by 1.5 percent, for each value of θ_e.

Table 6.4 Values of $r_1(\%)$ at the points after the second corner by 1.5 percent

s_1 \ θ_e	0°	30°	60°	90°	120°	150°	180°
0 %	—	2.9	2.0	−1.3	−2.1	−5.0	−11.9
0.25%	0.3	1.5	0.3	−0.8	−2.8	−3.6	−7.3
0.5 %	1.1	2.4	1.1	0.1	−1.7	−1.6	−4.2
1.0 %	1.6	2.4	2.7	0.4	−1.3	−1.7	−2.2

As found from the table, the maximum deviation (for $\theta_e=180°$) in these curves for each value of s_1 from the dashed curve becomes less with an increase of s_1. Moreover, for $s_1=1.0$ percent, every curve may be regarded to agree with the dashed curve within an error of 3 percent. Such a trend shows that every curve tends to the dashed one with the increase of s_1.

As another index for estimating the fading property of history effect due to the second branch, relation between a ratio $r_2(=\Delta|\sigma^*|/|\sigma^*|_B)$ of the amount of drop $\Delta|\sigma^*|$ after the point B(point A for $s_1=0\%$) to the magnitude $|\sigma^*|_B$ at the point B(or A) and the length s_1 is shown in Fig. 6.45 for each value of θ_e.

As found in the figure, the ratio r_2 is affected little by s_1 for $\theta_e=90°$, but it decreases remarkably in the range of $s_1<0.25$ percent for $\theta_e>90°$. For the case of $\theta_e<90°$, the ratio r_2 increases slightly with the increase of s_1. In other words, if the third branch lies in an unloading situation even partially to the first one, the scalar effect of the latter on the deformation along the former decreases

quickly for the existence of the second branch, especially in its early period. In the case of $s_1=1.0$ percent, the ratio r_2 for the curves corresponding to $\theta_e>90°$ and $\theta_e<90°$ deviate from that for $\theta_e=90°$ almost symmetrically, and the ratio for every curve may be supposed to tend to that for $\theta_e=90°$ in such a manner thereafter.

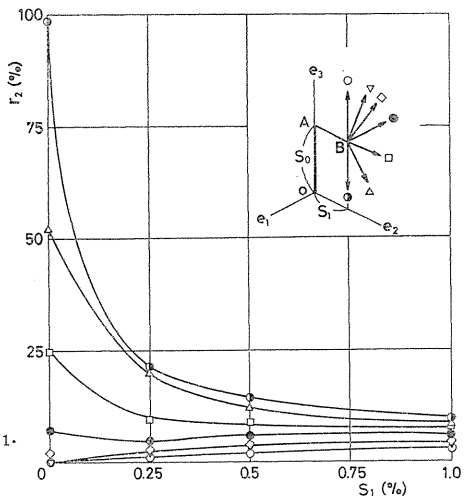

Fig. 6. 45 Relation between $r_2=\Delta|\sigma^*|/|\sigma^*|_B$ and s_1.

Chapter Ⅶ Formulation of the Experimental Results

In order to apply the results of experimental investigation to the deformation analyses, constitutive equation should be formulated from the results in a form of stress-strain relation. The effects due to the complex deformation history on the deformation behaviour of metals may be reflected as variations in the relation.

Concerning the method to formulate stress-strain relation from the experimental results, a method to formulate a stress-strain relation as a tensorial one has been introduced in Chapter Ⅳ. Another method to formulate stress-strain relation of integral type may be established according to a concept of the intrinsic time scale proposed by Valanis[27] in his endochronic theory.

These methods may be used to establish precise expressions of the history effect for deformation along each of complicated strain trajectories. However, the expressions of experimental results in these types may lead fairly complicated ones for complicated strain history.

On the other hand, if the stress drop just after the corner on the trajectory and the succeeding recovery would be negligible, the stress-strain curve may be approximated by the curve for the proportional deformation after modification. Judging from the experimental results, the stress drop just after the corner of bilinear trajectory does not appear significantly for the angle of corner less than 60°. Moreover, the drop decreases with the decrease of curvature of the corner for bilinear trajectory with rounded corner. Thus, this approximation may be useful for the deformation analyses of practical structure, because the strain trajectory in most of the element of engineering structures or materials under plastic processing may be expected as that of medium curvature.

The above-mentioned situation in mind, examples of these three methods will be considered in the following.

7. 1. Stress-strain relation in the form of tensorial equation[19]

From the discussion in Chapter Ⅳ and its experimental verification for special

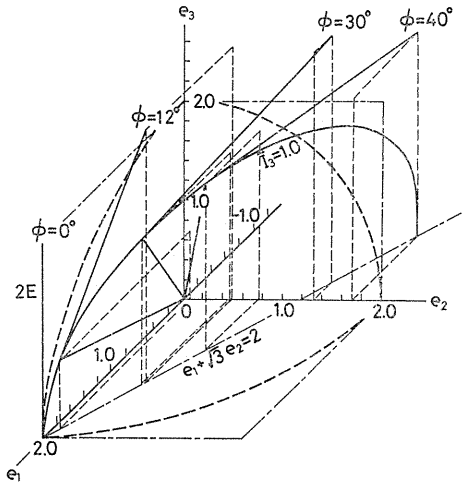

Fig. 7. 1 Orthogonal bi-linear strain trajectories equivaent to that for the test 2E.

case in Chapter Ⅵ, every strain trajectory oriented in the direction of $\bar{I}_3(\boldsymbol{D}_\sigma)=$ constant is tensorially equivalent, whereras the corresponding stress state may be different. For example, equivalent strain trajectories for the trajectory 2E shown in Table 6.1, obtained by rotating the coordinate axes established in the element by an angle ϕ around the axis-3 (radial direction of the specimen), are shown with the thick solid lines in Fig. 7.1. In other words, an orthogonal bi-linear trajectory having the right-angled corner at arbitrary point on the circle $\bar{I}_3(\boldsymbol{D}_\sigma)=$constant on the spherical surface, whose center lies at the origin, may represent all the trajectories having the corner point on the circle.

On the other hand, since the plane $\sqrt{3}e_1-e_2=0$ intersects with every circle mentioned above, as seen in Fig. 4.3, every trajectory having the corner on the spherical surface may be equivalent with either trajectory having it first branch in this plane. When a coordinate system $e_1'e_2'e_3'$ (Fig. 4.3) is introduced by rotating the system $e_1e_2e_3$ by 120° clockwise around the axis-3, the values of e_1', e_2' and e_3' may be expressed as follows:

$$e_1'=-(e_1+\sqrt{3}e_2)/2=-(e_{11}+e_{22}),\quad e_2'=(\sqrt{3}e_1-e_2)/2$$
$$=(e_{11}-e_{22})/\sqrt{3},\quad e_3'=e_3=2e_{12}/\sqrt{3}. \tag{7.1}$$

Since the plane $\sqrt{3}e_1-e_2=0$ is expressed by the plane-$e_1'e_3'$ in the system $e_1'e_2'e_3'$, every trajectory mentioned above may be replaced by a trajectory having its first branch in the plane-$e_1'e_3'$.

7. 1. 1. Stress-strain relation for orthogonal bi-linear strain trajectory whose first branch lies in the plane-$e_1'e_3'$

As shown in Fig. 7.2, an orthogonal bi-linear trajectory is considered in which the first branch makes an angle β to the axis-e_1' in the plane-$e_1'e_3'$, and the second branch makes an angle α to the plane-$e_1'e_3'$. Moreover, s_0 denotes the length of the first branch (pre-strain) and Δs denotes that of the second branch after the corner. When a local coordinate system $\sigma_1'\sigma_2'\sigma_3'$ whose axes are parallel with those of the previous system is established at a point on the second branch, the relation between σ_1', σ_2', σ_3' and σ_1, σ_2, σ_3 are expressed as follows:

$$\sigma_1'=-(\sigma_1+\sqrt{2}\sigma_2)/2=-3(s_{11}+s_{22})/2,$$
$$\sigma_2'=(\sqrt{3}\sigma_1-\sigma_2)/2=\sqrt{3}(s_{11}-s_{22})/2,$$
$$\sigma_3'=\sigma_3=\sqrt{3}s_{12}. \tag{7.2}$$

The direction of the vector de coincides with that of the second branch and the

direction of $\boldsymbol{\sigma}$ delays by an angle θ from that of $d\boldsymbol{e}$ in the plane of bi-linear trajectory. Therefore, in order to formulate the stress-strain relation in the form of Eq. (4.13), it is necessary to determine the orthogonal rotation tensor $\boldsymbol{L}$ as well as the angle of the stress state α_σ and the intensity ζ_σ of the stress deviator $\boldsymbol{D}_\sigma$.

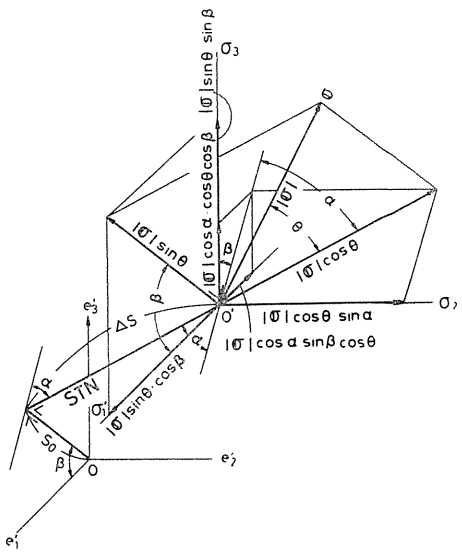

Fig. 7.2 Local stress space $V_{3\sigma}(\sigma_1'\ \sigma_2',\ \sigma_3')$ on the orthogonal bi-linear strain trajectory in the space $V_{3e}(e_1'\ e_2',\ e_3')$.

7. 1. 1. 1. Determination of angle α_σ or α_{de}

When the direction of $\boldsymbol{\sigma}$ delays from that of $d\boldsymbol{e}$ by the angle θ at the length Δs after the corner, the following relations are obtained from Fig. 7.2:

$$\sigma_1' = |\boldsymbol{\sigma}|(\sin\theta\cos\beta - \cos\theta\cos\alpha\sin\beta),$$

$$\sigma_2' = |\boldsymbol{\sigma}|\cos\theta\sin\alpha,\quad \sigma_3' = |\boldsymbol{\sigma}|(\cos\theta\cos\alpha\cos\beta + \sin\theta\sin\beta). \tag{7.3}$$

Moreover, the following relation is obtained from Eqs. (4.33) and (7.2):

$$\bar{I}_3(\boldsymbol{D}_\sigma) = \cos 3\alpha_\sigma = \sigma_1'(\sigma_1'^2 - 3\sigma_2'^2 - 3\sigma_3'^2)/(\sigma_1'^2+\sigma_2'^2+\sigma_3'^2)^{3/2}. \tag{7.4}$$

By substituting the relations (7.3) into (7.4), α_σ is expressed as follows:

$$\alpha_\sigma = (1/3)\arccos[(\sin\theta\cos\beta - \cos\theta\cos\alpha\cos\beta)\{(\sin\theta\cos\beta - \cos\theta\cos\alpha\sin\beta)^2 - 3\cos^2\theta\sin^2\alpha - 3(\cos\theta\cos\alpha\cos\beta + \sin\theta\sin\beta)^2\}]. \tag{7.5}$$

In the same way, as for the vector $d\boldsymbol{e}$, the following expressions are found from Fig. 7.2:

$$de_1' = -|d\boldsymbol{e}|\cos\alpha\sin\beta,\quad de_2' = |d\boldsymbol{e}|\sin\alpha,\quad de_3' = |d\boldsymbol{e}|\cos\alpha\cos\beta. \tag{7.6}$$

By substituting the relations (7.6) into the relation obtained from Eqs. (4.31) and (7.1), α_{de} is expressed as follows:

$$\alpha_{de} = (1/3)\arccos\{-\cos\alpha\sin\beta(\cos^2\alpha\sin^2\beta - 3\sin^2\alpha - 3\cos^2\alpha\cos^2\beta)\}. \tag{7.7}$$

7. 1. 1. 2. Determination of the orthogonal rotation tensor $\boldsymbol{L}$

There exist the following relations between the orthogonal rotation tensor

$\boldsymbol{L}(=L_{ij}\boldsymbol{e}_i\boldsymbol{e}_j;\ i,\ j=1,\ 2,\ 3)$ and the rotation vector $\boldsymbol{\omega}=\omega_k\boldsymbol{e}_k$:

$$\boldsymbol{L}=\exp(\omega\boldsymbol{\Omega})=\boldsymbol{I}+\sin\omega\boldsymbol{\Omega}+(1-\cos\omega)\boldsymbol{\Omega}^2,$$

$$\boldsymbol{L}^{-1}=\exp(-\omega\boldsymbol{\Omega})=\boldsymbol{I}-\sin\omega\boldsymbol{\Omega}+(1-\cos\omega)\boldsymbol{\Omega}^2 \tag{7.8a}$$

and

$$\boldsymbol{I}=\delta_{ij}\boldsymbol{e}_i\boldsymbol{e}_j,\ \boldsymbol{\Omega}=\Omega_{ij}\boldsymbol{e}_i\boldsymbol{e}_j,\ \Omega_{ij}=(\alpha_{ij}-\alpha_{ji})/2,\ \alpha_{ij}=e_{ijk}\alpha_k, \tag{7.8b}$$

where ω denotes the magnitude (rotation angle) of $\boldsymbol{\omega}$, and α_k denotes the direction of $\boldsymbol{\omega}$ (direction cosine of the axis of rotation).

Along the second branch of the orthogonal bi-linear trajectory, the magnitude ω is given as

$$\omega=\omega_\sigma-\omega_{de}, \tag{7.9a}$$

where

$$\tan 2\omega_\sigma=2s_{12}/(s_{11}-s_{22})=\sigma'_3/\sigma'_2=(\cos\theta\cos\alpha\cos\beta+\sin\theta\sin\beta)/\cos\theta\sin\alpha,$$

$$\tan 2\omega_{de}=2de_{12}/(de_{11}-de_{22})=de'_3/de'_2=\cos\alpha\cos\beta/\sin\alpha. \tag{7.9b}$$

Since the axis of rotation coincides with the axis-3 (radial direction in the specimen) of the coordinate system established in the element, the above-mentioned relations may be reduced to the case $\alpha_1=\alpha_2=0$, $\alpha_3=1$, and thus

$$\boldsymbol{\Omega}=\boldsymbol{e}_1\boldsymbol{e}_2-\boldsymbol{e}_2\boldsymbol{e}_1,\ \boldsymbol{\Omega}^2=-\boldsymbol{e}_1\boldsymbol{e}_1-\boldsymbol{e}_2\boldsymbol{e}_2. \tag{7.10}$$

By substituting Eqs. (7.9 a), (7.9 b) and (7.10) into (7.8 a), the orthogonal rotation tensor may be obtained.

7. 1. 1. 3. Determination of ζ_σ

The parameter ζ_σ expressing the intensity of $\boldsymbol{D}_\sigma$ is given in the following form:

$$\zeta_\sigma(\Delta s)=|\boldsymbol{\sigma}|(\Delta s)/\sqrt{3}=|\boldsymbol{\sigma}^*|(\Delta s)/\sqrt{3}R, \tag{7.11}$$

where R is given by Eq. (6.7). Since the expression $\{\arccos \bar{I}_3(\boldsymbol{D}_\sigma)\}/3$ in Eq. (6.7) corresponds to α_σ given in Eq. (7.5), if the functional form $\alpha_\sigma(\Delta s)$ in Eq. (7.5) is obtained from the experimental results, $\zeta_\sigma(\Delta s)$ may be found with the use of $|\boldsymbol{\sigma}^*|(\Delta s)$.

The relation between $\boldsymbol{D}_\sigma$ and $\boldsymbol{D}_{de}$ may be obtained by substituting these parameters into Eq. (4.13). From the relation thus obtained, the stress deviator $\boldsymbol{D}_\sigma$ may be calculated along the second branch of bi-linear trajectory whose first branch lies in the plane-$e_1'e_3'$.

7. 1. 2. Stress-strain relation for orthogonal bi-linear trajectory of arbitrary orientation

Stress-strain relation along the second branch of orthogonal bi-linear strain trajectory, whose first branch starts at the origin (state of zero strain), may be determined by selecting the corresponding angles α and β in Fig. 7.3 in the following manner.

If a strain vector on the first branch and a strain-increment vector on the second one are expressed by $\boldsymbol{e}_a=e_i^a\boldsymbol{n}_i'$ and $d\boldsymbol{e}_b=de_i^b\boldsymbol{n}_i'$, where $\boldsymbol{n}_i'$ denotes the base vector of the axis-e_i', respectively, the following condition holds:

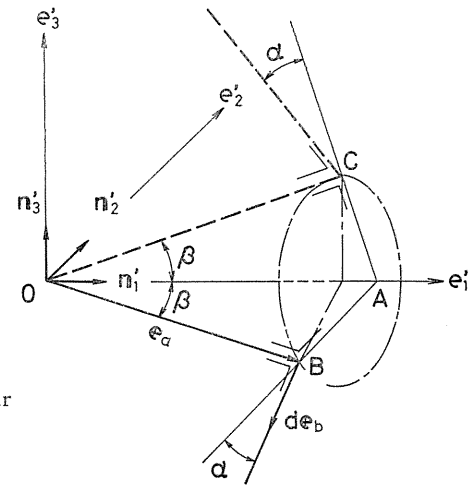

Fig. 7. 3 Equivalent orthogonal bi-linear trajectories in the space V_{3e}.

$$\boldsymbol{e}_a\cdot d\boldsymbol{e}_b=0. \tag{7.12}$$

One of the orthogonal bi-linear trajectories equivalent with the above-mentioned ones, whose first branch lies in the plane-$e_1'e_3'$, is shown in Fig. 7.3 with the dashed line. In the same figure, the relation

$$\cos\beta=\boldsymbol{n}_1'\cdot\boldsymbol{e}_a/|\boldsymbol{n}_1'||\boldsymbol{e}_a|=e_1/|\boldsymbol{e}_a| \tag{7.13}$$

may be found. From the relation $\mathbf{AB}=\boldsymbol{e}_a-\mathbf{OA}=\boldsymbol{e}_a-|\boldsymbol{e}_a|\boldsymbol{n}_1'/\cos\beta$, the following relation is obtained:

$$\cos\alpha=d\boldsymbol{e}_b\cdot\mathbf{AB}/|d\boldsymbol{e}_b||\mathbf{AB}|=-de_1/|d\boldsymbol{e}_b|\sin\beta. \tag{7.14}$$

These relations are expressed in tensor components as follows:

$$\cos\beta=-(e_{11}^a+e_{22}^a)/(2e_{ij}^ae_{ij}^a/3)^{1/2},$$

$$\cos\alpha=(de_{11}^b+de_{22}^b)/(2de_{ij}^bde_{ij}^b/3)^{1/2}\sin\beta. \tag{7.15}$$

7. 1. 3. Determination of the functional forms of $|\sigma^*|(\Delta s)$ and $\theta(\Delta s)$

On the second branch of the strain trajectory, the components of stress vector parallel and perpendicular to the trajectory are designated as $G_1(\Delta s)$ and $G_2(\Delta s)$. Since the component perpendicular to the trajectory decays with increase of Δs from the value at the corner, the functional form $G_2(\Delta s)$ may be obtained from Fig. 6.19 and 6.20 as follows:

$$G_2(\Delta s)=223\exp(-2.8\Delta s), \tag{7.16a}$$

where 223 MPa corresponds to the magnitude of the modified stress vector at the corner point.

On the other hand, the component of the stress vector parallel to the trajectory increases almost exponentially with the increase of Δs just after the corner, thus the form of $G_1(\Delta s)$ may be approximated by

$$G_1(\Delta s)=232.4\{1-\exp(-7.4\Delta s)\}+|35.58(\Delta s)^{0.7}-9.8|, \quad (7.16b)$$

where the second term on the right hand side modifies the function so that the experimental result may be approximated well for large value of Δs. This term does not affect significantly the value of $|\boldsymbol{\sigma}^*|(\Delta s)=G(\Delta s)$ at the corner ($\Delta s=0$) for the sufficiently large value of $G_2(\Delta s)$. Then, the functional form of $G(\Delta s)$ is obtained from the following relation:

$$G(\Delta s)=\{G_1^2(\Delta s)+G_2^2(\Delta s)\}^{1/2}. \quad (7.16c)$$

The functional form of $\theta(\Delta s)=F(\Delta s)$ obtained from the experimental result may be expressed as follows:

$$F(\Delta s)=30\{2\exp(-10\Delta s)+\exp(-2.5\Delta s)\}. \quad (7.17)$$

The results of $|\boldsymbol{\sigma}^*|$ and θ calculated by Eqs. (7.16) and (7.17) are shown in Figs. 6.19 and 6.20 with solid curves, respectively. As found in these figure, the functions (7.16) and (7.17) are close approximations of the experimental results, respectively.

7. 1. 4. Calculation of stress-strain relation and comparison with the experimental result

The calculation was carried out for the above-mentioned strain trajectories 2C and 2E (Figs. 6.16 and 6.18). These two trajectories are equivalent tensorially and correspond with the case of $\cos\alpha=0$ and $\cos\beta=-1/2$ as found from the relation (7.15). In this case, the angle α_σ expressing the stress state is obtained from (7.5) as follows:

$$\alpha_\sigma=(1/3)\arccos(\sin^3\theta+(3/2)\sin\theta\cos^2\theta). \quad (7.18)$$

As the relations

$$\tan 2\omega_\sigma=(\sqrt{3}/2)\tan\theta, \quad \tan 2\omega_{de}=0 \quad (7.19)$$

are obtained from (7.9b), the direction of principal axis is determined as follows:

$$\omega=(1/2)\arctan\{(\sqrt{3}/2)\tan\theta\}. \quad (7.20)$$

The orthogonal rotation tensor $\boldsymbol{L}$ is obtained from (7.8a), (7.10) and (7.20) as follows:

$$\begin{aligned}\boldsymbol{L}&=\cos[(1/2)\arctan\{(\sqrt{3}/2)\tan\theta\}](\boldsymbol{e}_1\boldsymbol{e}_1+\boldsymbol{e}_2\boldsymbol{e}_2)\\&\quad+\sin[(1/2)\arctan\{(\sqrt{3}/2)\tan\theta\}](\boldsymbol{e}_1\boldsymbol{e}_2-\boldsymbol{e}_2\boldsymbol{e}_1)+\boldsymbol{e}_3\boldsymbol{e}_3,\\\boldsymbol{L}^{-1}&=\cos[(1/2)\arctan\{(\sqrt{3}/2)\tan\theta\}](\boldsymbol{e}_1\boldsymbol{e}_1+\boldsymbol{e}_2\boldsymbol{e}_2)\\&\quad-\sin[(1/2)\arctan\{(\sqrt{3}/2)\tan\theta\}](\boldsymbol{e}_1\boldsymbol{e}_2-\boldsymbol{e}_2\boldsymbol{e}_1)+\boldsymbol{e}_3\boldsymbol{e}_3.\end{aligned} \quad (7.21)$$

From (7.11) and (6.7), the following relation is found:

$$\begin{aligned}&\zeta_\sigma=G(\Delta s)/\sqrt{3}R,\\&R=[1+4(R_0^2-1)\cos^2\{2\pi/3-(1/3)\arccos(\sin^3\theta+(3/2)\sin\theta\cos^2\theta)\}]^{1/2}.\end{aligned} \quad (7.22)$$

By substituting these relations into (4.12) and using the relation $\theta=F(\Delta s)$, components of $\boldsymbol{D}_\sigma$ may be expressed in relation to Δs as follows:

$$s_{ij}(\Delta s)=G(\Delta s)\left[\sin\{\pi/3+(1/3)\arccos\left[\sin^3\theta+(3/2)\sin\theta\cos^2\theta\right]\}\right.$$
$$\times L_{ik}de_{km}L_{mj}^{-1}/\zeta_\sigma+\sqrt{3}\sin\{\pi/6-(1/3)\arccos\left[\sin^3\theta+(3/2)\right.$$
$$\left.\times\sin\theta\cos^2\theta\right]\}\left[L_{ik}de_{km}de_{mn}L_{nj}^{-1}/\zeta_\sigma^2-\sqrt{2/3}\,\delta_{ij}\right]\Big)/\left[3+12(R_0^2-1)\right.$$
$$\left.\times\cos^2\{2\pi/3-(1/3)\arccos\left[\sin^3\theta+(3/2)\sin\theta\cos^2\theta\right]\}\right]^{1/2}$$
$$(i,\ j,\ k,\ m,\ n=1,\ 2,\ 3), \tag{7.23a}$$

where

$$L_{11}=L_{22}=L_{11}^{-1}=L_{22}^{-1}=\cos\left[(1/2)\arctan(\sqrt{3}\tan\theta/2)\right],$$
$$L_{12}=-L_{21}=-L_{12}^{-1}=L_{21}^{-1}=\sin\left[(1/2)\arctan(\sqrt{3}\tan\theta/2)\right],$$
$$L_{33}=L_{33}^{-1}=0,$$
$$L_{13}=L_{31}=L_{32}=L_{23}=L_{13}^{-1}=L_{31}^{-1}=L_{32}^{-1}=L_{23}^{-1}=0, \tag{7.23b}$$

and

$$R_0(s)=1-1/(21.48s^{0.26}),$$
$$G(\Delta s)=\left(\left[232.4\{1-\exp(-7.4\Delta s)\}+|35.58(\Delta s)^{0.7}-9.8|\right]^2\right.$$
$$\left.+\{223\exp(-2.8\Delta s)\}^2\right)^{1/2}, \tag{7.23c}$$
$$F(\Delta s)=30\{2\exp(-10\Delta s)+\exp(-2.5\Delta s)\},$$
$$s=\sqrt{3/2}\int_0^{e_{ij}}(de_{ij}de_{ij})^{1/2},\quad \Delta s=s-s_0,\quad s_0=2\,\%. \tag{7.23d}$$

The results of calculation are shown in Fig. 7.4 by the solid curves. In the figure, various symbols show the corresponding experimental results. These solid curves approximate the experimental results with high accuracy, and almost the same degree of approximation can be obtained for other experimental results. Therefore, it may be concluded that the tensorial equation (4.12) may approximate with high accuracy the stress-strain relation along the second branch of every

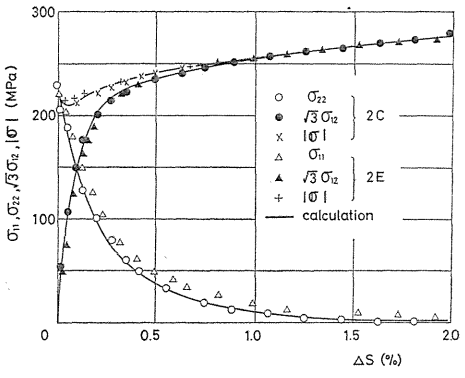

Fig. 7.4 Relation between stress components and Δs calculated by tensorial equation and the corresponding experimental results in the tests 2C and 2E for mild steel S10C.

trajectory in the set of orthogonal bi-linear strain trajectories of fixed geometry, if the deformation characteristics of the material are measured along anyone of them.

The above-mentioned history effects cannot be formulated by the conventional flow rule. However, in the range $\Delta s > 1.0$ percent, since such a complicated history effect declines sufficiently, the conventional stress-strain-increment relation may become a good approximation.

7. 2. Stress-strain relation of integral type according to the concept of intrinsic time scale[28]

In the vector space corresponding to the strain deviator, a geometrical concept of deformation history may be secured by drawing curves in the space. When the curve is assigned, if closely adjacent two points are taken arbitrarily on the curve, the stress increment between these two points depends on the corresponding strain increment through the following form:

$$d\boldsymbol{\sigma} = \boldsymbol{K}' d\boldsymbol{e}.$$

The coefficient $\boldsymbol{K}'$ plays a role of influence function operating on the strain-increment. If the deformation property does not vary completely, $\boldsymbol{K}'$ may be expressed in terms of a matrix having constant elements and is independent of the geometry of the curve. This situation corresponds to the elastic deformation. When the history dependence appears, the influence function varies at each point on the curve according to its geometry. The coefficient of $d\boldsymbol{e}$ at the preceding point contributing the stress-increment $d\boldsymbol{\sigma}$ at a point considered on the curve may be a function of arc length together with the geometric parameter (curvature, torsion and others) of the curve. Accordingly, the stress state at a certain point (s) on the curve may be expressed by an integral form

$$\boldsymbol{\sigma}(s) = \int_0^s \boldsymbol{K}(\kappa_i;\ s,\ s')\, d\boldsymbol{e}(s') \quad 0 \leq s' \leq s \tag{7.24}$$

of the stress-increment taken at every preceding point (s'), where s and s' denote the arc length of the curve up to the corresponding points, and $\kappa_i(s')$ are the geometric parameters. Ilyushin[9] proposed another integral form:

$$\boldsymbol{\sigma}(s) = \int_{s-h}^s \boldsymbol{K}(\kappa_i;\ s,\ s')\, d\boldsymbol{e}(s') \quad s-h \leq s' \leq s, \tag{7.25}$$

restricting the range of integration to a finite arc length h ($s-h \leq s' \leq s$) preceding the point (s) instead of of $0 \leq s' \leq s$, by taking into account the fading memory which appears in real materials. The arc length h is called "trace of delay". This hypothesis is called Ilyushin's "principle of delay". According to this principle, the expression of the history effect may be remarkably simplified, since the effect may be considered by taking account of the geometry of the curve only in a finite range preceding the point considered.

In the linear viscoelastic theory, for the stress-strain relation of history dependent materials, the stress components at a certain instant in the real time scale during the deformation process have been expressed in the following form:

$$\sigma_{ij}(t)=\int_0^t K_{ijmn}(t,\ \tau)\,d\varepsilon_{mn}(\tau) \quad 0\leq\tau\leq t. \tag{7.26}$$

In this form, since the stress-strain relation is expressed in terms of real time as a parameter, the influence coefficient may be understood as a function of real time. That is, the deformation property may be understood to vary according to real time. However, since the deformation property of real materials depends not on time but essentially on deformation history, the concept expressed in the form (7.26) is not always accurate because it may express definite deformation phenomena only when a certain relation between deformation history and time is given for the influence coefficient.

In the linear viscoelastic theory, the form

$$\sigma_{ij}(t)=\int_0^t K_{ijmn}(t-\tau)\,d\varepsilon_{mn}(\tau) \quad 0\leq\tau\leq t \tag{7.27}$$

is often used as a special case of (7.26) together with

$$K_{ijmn}(t-\tau)=\mu_{ijmn}e^{-\lambda(t-\tau)} \tag{7.28}$$

for convenience of calculation as well as for the consideration of fading memory. Such a coefficient of the difference type is a fairly strong limitation, since it is effective only for the deformation in which the influence function may always be described using Eq. (7.28) for arbitrary instant t.

Recently, Valanis[27] proposed an "endochronic theory" for materials with memory depending on deformation history. According to this theory, the relation between the stress deviator S_{ij} and the strain deviator e_{ij} is expressed in the following form:

$$S_{ij}=2\int_0^z K(z,\ z')\frac{de_{ij}}{dz'}dz'=2\int_0^\zeta K\{z(\zeta),\ z(\zeta')\}\frac{de_{ij}}{d\zeta'}d\zeta' \tag{7.29}$$

with the use of an intrinsic time scale z, where an intrinsic time measure ζ is defined as:

$$d\zeta^2=k^2de_{ij}de_{ij} \quad (k>0:\ \text{material parameter}). \tag{7.30}$$

The intrinsic time scale z, which expresses the sequence of variations of deformation behaviour of materials and does not necessarily correspond to real time, is defined as a monotonously increasing positive function of the intrinsic time measure ζ as follows:

$$dz(\zeta)=\frac{d\zeta}{f(\zeta)} \quad \text{or} \quad z(\zeta)=\int_0^\zeta\frac{d\zeta'}{f(\zeta')}, \quad dz/d\zeta>0. \tag{7.31}$$

It may be found from Eq. (7.30) that the intrinsic time measure ζ is a certain parameter expressing the deformation behaviour in relation to the deformation history of materials, and thus the measure is related with the state and intensity of deformation. As found from Eq. (7.31), if a converted time scale reflecting the history dependence is used for establishing a stress-strain relation, the formula (7.29) having the same form as Eq. (7.26) may be expressed in an analogous form as Eq. (7.27) together with Eq. (7.28). The corresponding influence coefficient of

difference type $K\{z(\zeta)-z(\zeta')\}$ is free from the above-mentionned limitation, according to which Eqs. (7.27) and (7.28) have been restricted. This is so because the value $z(\zeta)-z(\zeta')$ is not constant but is always a function of the corresponding value of ζ. In other words, the formula (7.29) may express non-linear effect of deformation history nevertheless it has a linear form with respect to the intrinsic time scale z, because the non-linear variation of deformation behaviour of material in the course of deformation may be separated in the function $f(\zeta)$. Consequently, the stress-strain relation may be formulated reasonably for plastic behaviour under arbitrary deformation history, if Valanis' endochronic theory is used together with Ilyushin's postulate of isotropy and principle of delay.

As an example of the application of this theory, Valanis calculated a plastic deformation under tension after torsion[27]. He expressed Eq. (7.30) in the form $d\zeta^2=k_1d\varepsilon^2+k_2d\eta^2$, used a linear function $f(\zeta)=1+\beta\zeta$ of ζ, and established a stress-strain relation by using the parameter $\zeta_0=k_2\beta$ showing torsional pre-strain as well as a cross-hardening parameter β. Moreover, the relation $\zeta=\zeta_0+k_1\varepsilon$ or $d\zeta=k_1d\varepsilon$ is assumed in the tensile deformation, and a new parameter $\beta_1=k_1\beta$ is determined under the assumption that the stress-strain curve under uniaxial tention, starting at the state where effect of pre-strain has vanished after pre-torsion, would tend to a linear form

$$\sigma=\frac{E_0}{\beta_1 n}(1+\beta_1\varepsilon), \tag{7.32}$$

for a sufficiently large value of tensile strain ε.

However, his method as quoted above was not found to be sufficient to approximate with high accuracy the experimental results of plastic deformation of brass under the severe history effect mentioned in Section 6.5.1. This may be attributable to the fact that the influence function and the intrinsic time scale z were not found in suitable forms to reflect reasonably the severe history effect.

In what follows, a method is proposed to formulate the experimental results of plastic deformation of brass having the severe history effect in the form of integral type, by selecting the influence coefficient and the intrinsic time scale z so as to reflect reasonably the history effect.

7.2.1. Fundamental equations

The history of strain deviator appearing in the thin-walled tubular specimen under torsion and axial force may be described as curves showing the strain trajectory in a vector plane of the strain deviator ($e_1=e_{11}$. $e_3=2e_{12}/\sqrt{3}$), where e_{11} and e_{12} denote the axial and shear components of the strain deviator calculated from the experimental results of the thin-walled tubular specimen, and the indices 1 and 2 correspond to the axial and circumferential directions of the specimen, respectively. As mentioned in Section 4.2, the states of the strain deviator and its increment at each point on the curve may be expressed by a strain vector $\boldsymbol{e}=e_{11}\boldsymbol{n}_1+(2/\sqrt{3})e_{12}\boldsymbol{n}_3$ ($|\boldsymbol{e}|$ is equal to the effective strain ε_{eq}) and $d\boldsymbol{e}=de_{11}\boldsymbol{n}_1+(2/\sqrt{3})de_{12}\boldsymbol{n}_3$, respectively. Moreover, the state of stress deviator may be expressed by a stress vector $\boldsymbol{\sigma}=\sigma_{11}\boldsymbol{n}_1+\sqrt{3}\sigma_{12}\boldsymbol{n}_3$ ($|\boldsymbol{\sigma}|$ is equal to the effective stress σ_{eq}) in a local vector spece of the stress deviator ($S_{11}=(2/3)\times\sigma_{11}=(2/3)\sigma_1$, $S_{12}=\sigma_{12}=\sigma_3/\sqrt{3}$), where σ_{11} and σ_{12} denote the axial and shear stress components. These components appear in the specimen, which are used

after modifying the effect of third invariant by means of the coefficient R_0 introduced in Section 6.1.3. The orthonormal base vectors $\boldsymbol{n}_1$ and $\boldsymbol{n}_3$ are used in the stress and strain vector spaces in common.

By using the components mentioned above, the formula (7.24) is expanded into the following forms:

$$\sigma_{11}=\int_0^s K_{11}(s,\ s';\ \kappa_i)de_{11}+\frac{2}{\sqrt{3}}\int_0^s K_{12}(s,\ s';\ \kappa_i)de_{12},$$

$$\sqrt{3}\sigma_{12}=\int_0^s K_{21}(s,\ s';\ \kappa_i)de_{11}+\frac{2}{\sqrt{3}}\int_0^s K_{22}(s,\ s';\ \kappa_i)de_{12}, \qquad (7.33)$$

where κ_i in the argument of the influence function in Eq. (7.33) are the geometric parameters of the strain trajectory expressing the deformaiton history of materials quantitatively. If the history effect including the effect appearing in the case of zero curvature is reflected in the functional relation $z(s)$ by putting $\zeta=s$, and the influence coefficients are expressed as $K_{ij}\{z(s),\ z(s')\}$, the above formula (7.33) may be transformed as follows:

$$\sigma_{11}=\frac{3}{2}S_{11}=\int_0^s K_{11}\{z(s),\ z(s')\}\frac{de_{11}}{ds'}ds'+\frac{2}{\sqrt{3}}\int_0^s K_{12}\{z(s),\ z(s')\}\frac{de_{12}}{ds}ds',$$

$$\sqrt{3}\sigma_{12}=\sqrt{3}S_{12}=\int_0^s K_{21}\{z(s),\ z(s')\}\frac{de_{11}}{ds'}ds'$$

$$+\frac{2}{\sqrt{3}}\int_0^s K_{22}\{z(s).\ z(s')\}\frac{de_{12}}{ds'}ds'. \qquad (7.34)$$

Valanis defined the intrinsic time measure ζ in relation to the feature of strain state and the response of the material to that state in the material parameter k in Eq. (7.30). He also determined the influence coefficient in the form of the scalar function according to the proportional deformation by assuming a simple scalar relation between the intrinsic time measure and the intrinsic time scale. However, his method is not suitable to formulate reasonably the deformation behaviour along the strain trajectory with a corner. On the other hand, in order to reflect the experimental fact in which the response of materials is affected essentially by the existence of corners, the influence coefficients and the functions $z(s)$ and $z(s')$ in Eq. (7.34) are assumed to have different characters before and after the corner.

7. 2. 2. Stress-strain relation of brass for the deformation along orthogonal tri-linear strain trajectory in two-dimensional vector space

The experimental results discussed in Section 6.5.1 along the orthogonal trilinear trajectories in two-dimensional vector space are formulated by using Eq. (7.34).

As shown in Fig. 7.5, the experimental results have been obtained along the strain trajectory consisting of the first branch ($de_{11}>0$, $de_{12}=0$, $0\leq s\leq s_0$), the second branch ($de_{11}=0$, $de_{12}>0$, $s_0\leq s\leq s_1$) and the third branch ($de_{11}\neq 0$, $de_{12}=0$, $s_1\leq s$), and thus the stress-strain relation will be formulted in relation to each branch.

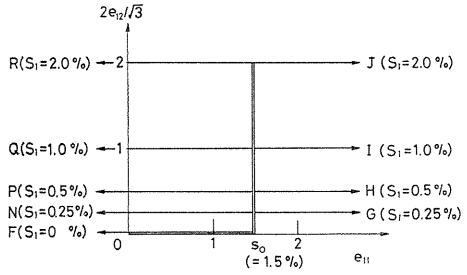

Fig. 7. 5 Orthogonal tri-linear strain trajectories in the space V_{2e}.

7. 2. 2. 1. First branch ($0 \leq s \leq s_0$)

Since $de_{11}>0$, $de_{12}=0$ and there is no shear stress ($\sigma_{12}=0$) in this branch, the stress-strain relation may be established from Eq. (7.34), by using K_a and $z_a(s)$ as the influence coefficient K and the intrinsic time scale $z(s)$, as follows:

$$S_{11}(s)=\frac{2}{3}\int_0^s K_a\{z_a(s),\ z_a(s')\}\frac{de_{11}}{ds'}ds'. \tag{7.35}$$

If a function of the difference type

$$K_a\{z_a(s),\ z_a(s')\}=\mu_a \exp\left[-\{z_a(s)-z_a(s')\}\right],\quad \mu_a=\text{const} \tag{7.36}$$

is used as the influence coefficient, then the contribution of the strain increment de at the preceding instant of the intrinsic time scale $z_a(s')$ to the stress increment $d\sigma$ at the instant $z_a(s)$ decreases from a constant amount $d\sigma=\mu_a de$ exponentially in relation to the intrinsic time interval between these two instants, and Eq. (7.35) is described as follows:

$$S_{11}(s)=\frac{2}{3}\mu_a e^{-z_a(s)}\int_0^s e^{z_a(s')}\frac{de_{11}}{ds'}ds',\quad 0\leq s'\leq s. \tag{7.37}$$

Since the variations of the deformation property are reflected in the functions $z_a(s)$ and $z_a(s')$, the coefficient of the difference type may be applied to arbitrary value of s and s', and the above equation can formulate the experimental results with high accuracy.

7. 2. 2. 2. Second branch ($s_0 \leq s \leq s_0+s_1$)

When a point under consideration (s) lies in the second branch, the contribution of de at the preceding point (s') to the stress-increment $d\sigma$ at the point (s) is quite different from that in the previous Section 7. 2. 2. 1. For example, $de(de_{11}>0,\ de_{12}=0)$ on the first branch changes suddenly into $de(de_{11}=0,\ de_{12}>0)$ at the corner point $s=s_0$, while $|de|/dt(=\dot{s})$ is kept constant along the the trajectory, and S_{11} decreases quickly at first and slowly afterwards along the second branch. This trend may be attributed to a kind of instability in microscopic structure of materials at the corner $s_0=e_{11}$ besides the relaxation of S_{11} due to the sudden vanishment of de_{11}. The instability may correspond to a release of dislocation which has piled up during the deformation process along the first branch by a disturbance de_{12} applied after the corner in another direction[16] (release of locked potential energy). By taking account of these effects, the influence coefficient on

the second branch is distinguished as K_b which is different from K_a on the first branch. Moreover, for the same reason the intrinsic time scale should also be different according to whether the preceding point (s') lies on the first or second branch. Therefore the influence coefficient at the point (s) on the second branch may be selected as

$$K_b\{z_{b\alpha}(s),\ z_{b\alpha}(s')\}=\mu_b \exp\left[-\{z_{b\alpha}(s)-z_{b\alpha}(s')\}\right]$$
$$\text{for } z(s_0)\leq z(s)\leq z(s_0+s_1),\quad z(0)\leq z(s')\leq z(s_0),$$
$$K_b\{z_{b\beta}(s),\ z_{b\beta}(s')\}=\mu_b \exp\left[-\{z_{b\beta}(s)-z_{b\beta}(s')\}\right]$$
$$\text{for } z(s_0)\leq z(s)\leq z(s_0+s_1),\quad z(s_0)\leq z(s')\leq z(s), \tag{7.38}$$

and the stress-strain relations on the second branch are found from Eq. (7.34) in the following form:

$$S_{11}=\frac{2}{3}\int_0^{s_0}K_b\{z_{b\alpha}(s),\ z_{b\alpha}(s')\}\frac{de_{11}}{ds'}ds'=\frac{2}{3}\mu_b e^{-z_{b\alpha}(s)}\int_0^{s_0}e^{z_{b\alpha}(s')}\frac{de_{11}}{ds'}ds',$$
$$S_{12}=\frac{2}{3}\int_{s_0}^{s}K_b\{z_{b\beta}(s),\ z_{b\beta}(s')\}\frac{de_{12}}{ds'}ds'=\frac{2}{3}\mu_b e^{-z_{b\beta}(s)}\int_{s_0}^{s}e^{z_{b\beta}(s')}\frac{de_{12}}{ds'}ds', \tag{7.39}$$

because $de_{12}=0$ $(0\leq s\leq s_0)$ and $de_{11}=0$ $(s_0\leq s)$. The influence coefficient K_{21} is equal to 0 because there is no shear stress S_{12} on the first branch, and K_{12} is taken as 0 since the effect of torsional strain to S_{11} after the corner has been considered in the difference between K_a and K_b.

By using the expression $S_{11}(s_0)=\sigma_0$, σ_0 may be found from (7.37) and the following relation is obtained from (7.39).

$$\sigma_0=\frac{2}{3}\mu_b e^{-z_{b\alpha}(s)}\int_0^{s_0}e^{z_{b\alpha}(s')}\frac{de_{11}}{ds'}ds'.$$

In this way, we get

$$\int_0^{s_0}e^{z_{b\alpha}(s')}\frac{de_{11}}{ds'}ds'=\frac{3}{2\mu_b}\sigma_0 e^{z_{b\alpha}(s_0)}.$$

Consequently, the stress-strain relations on the second branch may be established as follows:

$$S_{11}(s)=\sigma_0 e^{-\{z_{b\alpha}(s)-z_{b\alpha}(s_0)\}},\quad S_{12}(s)=\frac{2}{3}\mu_b e^{-z_{b\beta}(s)}\int_{s_0}^{s}e^{z_{b\beta}(s')}\frac{de_{12}}{ds'}ds'. \tag{7.40}$$

7. 2. 2. 3. Third branch $(s_0+s_1\leq s)$

Since the method for deriving the stress-strain relation is almost the same as those in the previous section, only the results are described without detailed derivations. There are $de_{11}\neq 0$ and $de_{12}=0$ on the third branch, and thus the stress-strain relation may be expressed as follows:

$$S_{11}=\frac{2}{3}\mu_c e^{-z_{c\alpha}(s)}\int_0^{s_0} e^{z_{c\alpha}(s')}\frac{de_{11}}{ds'}ds'+\frac{2}{3}\mu_c e^{-z_{c\tau}(s)}\int_{s_0+s_1}^{s} e^{z_{c\tau}(s)}\frac{de_{11}}{ds'}ds',$$

$$S_{12}=\frac{2}{3}\mu_c e^{-z_{c\beta}(s)}\int_{s_0}^{s_0+s_1} e^{z_{c\beta}(s')}\frac{de_{12}}{ds'}ds'. \tag{7.41}$$

If the values of S_{11} and S_{12} at the second corner $s=s_0+s_1$ are denoted as σ_1 and τ_1, the following relations are obtained from (7.41):

$$\int_0^{s_0} e^{z_{c\alpha}(s')}\frac{de_{11}}{ds'}ds'=\frac{3}{2\mu_c}\sigma_1 e^{z_{c\alpha}(s_0+s_1)},$$

$$\int_{s_0}^{s_0+s_1} e^{z_{c\beta}(s')}\frac{de_{12}}{ds'}ds'=\frac{3}{2\mu_c}\tau_1 e^{z_{c\beta}(s_0+s_1)}.$$

Consequently, the stress-strain relation on the third branch may be established as follows:

$$S_{11}(s)=\sigma_1 e^{-\{z_{c\alpha}(s)-z_{c\alpha}(s_0+s_1)\}}+\frac{2}{3}\mu_c e^{-z_{c\tau}(s)}\int_{s_0+s_1}^{s} e^{z_{c\tau}(s')}\frac{de_{11}}{ds'}ds',$$

$$S_{12}(s)=\tau_1 e^{-\{z_{c\beta}(s)-z_{c\beta}(s_1+s_1)\}}. \tag{7.42}$$

7. 2. 3. Determination of the intrinsic time scale z and the coefficient μ

7. 2. 3. 1. First branch (μ_a, z_a)

The following equation may be obtained by the Taylor expansion of Eq. (7.37) in the vicinity of $s=0$ and after disregarding the infinitesimal terms higher than the second order:

$$\Delta S_{11}=S_{11}(\Delta s)-S_{11}(0)=\frac{2}{3}\mu_a\frac{de_{11}}{ds}\Delta s=\frac{2}{3}\mu_a\Delta s \quad (\Delta s=\Delta e_{11}). \tag{7.43}$$

By using (7.43), μ_a may be determined from the tensile stress response in the early stage of deformation.

The formula

$$dz_a=[(2/3)\mu_a de_{11}-dS_{11}]/S_{11} \tag{7.44}$$

to find dz_a may be obtained by tranforming Eq. (7.37) into a differential type. The values of $z_a(s)$ and $dz_a(s)$ may be calculated by using Eq. (7.44) from the experimental results obtained by uniaxial tension.

7. 2. 3. 2. Second branch (μ_b, $z_{b\alpha}$, $z_{b\beta}$)

The expression $(7.40)_2$ has the same form as Eq. (7.37). Thus the following formula may be found in the same way as that for Eq. (7.43):

$$\Delta S_{12}=S_{12}(s_0+\Delta s)-S_{12}(s_0)=\frac{2}{3}\mu_b\frac{de_{12}}{ds}\Delta s=\frac{2}{3}\mu_b\Delta s \quad (\Delta s=\Delta e_{12}). \tag{7.45}$$

By using Eq. (7.45), μ_b may be found from the relation between shear stress and strain measured just after the corner. After transforming $(7.40)_2$ into a

differential form, the following formula to find $dz_{b\beta}$ may be obtained:

$$dz_{b\beta}=[2/3)\mu_b de_{12}-dS_{12}]/S_{12}. \tag{7.46}$$

In the same manner, the formula

$$dz_{b\alpha}=-dS_{11}(s)/S_{11}(s)$$

may be found from Eq. $(7.40)_1$. By using these formulas, the values of $z_{b\alpha}(s)$ and $z_{b\beta}(s)$ as well as $dz_{b\alpha}(s)$ and $dz_{b\beta}(s)$ may be found from the experimental results on the second branch.

7. 2. 3. 3. Third branch (μ_c, $z_{c\alpha}$, $z_{c\beta}$, z_{cr})

By transferring the first term of the right hand side of Eq. $(7.42)_1$ to the other side, and indicating the left hand side as $X(s)$, the following formula may be obtained:

$$X(s)=S_{11}(s)-\sigma_1 e^{-\{z_{c\alpha}(s)-z_{c\alpha}(s_0+s_1)\}}=\frac{2}{3}\mu_c e^{-z_{cr}(s)}\int_{s_0+s_1}^{s} e^{z_{cr}(s')}\frac{de_{11}}{ds'}ds'.$$

Then the Taylor expansion of $X(s)$ in the vicinity of $s=s_0+s_1$ may derive the following relation:

$$\Delta X=X(s_0+s_1+\Delta s)-X(s_0+s_1)=S_{11}(s_0+s_1+\Delta s)-S_{11}(s_0+s_1)$$

$$-\sigma_0(e^{-\{z_{c\alpha}(s_0+s_1+\Delta s)-z_{c\alpha}(s_0+s_1)\}}-1)=\frac{2}{3}\mu_c\frac{de_{11}}{ds}\Delta s=\frac{2}{3}\mu_c\Delta e_{11}, \tag{7.47}$$

after disregarding infinitesimal terms higher than the second order.

If the condition $z_{c\alpha}(s)=z_{cr}(s)$ is assumed for simplicity, the formula

$$dz_{c\alpha}=dz_{cr}=[(2/3)\mu_c de_{11}-dS_{11}]/S_{11} \tag{7.48}$$

is found from Eq. $(7.42)_1$. The formula

$$dz_{c\beta}=-dS_{12}(s)/S_{12}(s) \tag{7.49}$$

is also obtained from Eq. $(7.42)_2$.

By using Eqs. (7.47), (7.48) and (7.49), the values of μ_c, $z_{c\alpha}(s)$ $(=z_{cr}(s))$ and $z_{c\beta}(s)$ as well as $dz_{c\alpha}(s)$ $(=dz_{cr}(s))$ and $dz_{c\beta}(s)$ may by obtained from the experimental results along the third branch.

7. 2. 3. 4. Values of μ and z found from the experimental results

The values of μ and z were determined by using the experimental results along the strain trajectories shown in Fig. 7.5. Since the stress-strain curve obtained from experimental result did not tend to straight line for large value of strain, the functional form $f(\zeta)=1+\beta\zeta$ used by Valanis[27] was not suitable to reproduce them. On the other hand, the functional form $f(s)=a(s+c)^b$ was ascertained to be able to approximate every stress-strain curve with high accuracy. The corresponding values of a, b and c for each branch differ from each other. Since the amounts $s_0=1.5$ percent$(=\text{const})$ and $s_1=0$, 0.25, 0.5, 1.0 and 2.0 percent have been assigned, the values of a, b and c on the third branch should be functions of s_1.

Moreover, there are remarkable differences between the trends in the values of a, b, c and μ_c along the third branches of the group G through J, in which the magnitude of stress vector continuously increases along the branch, and those along the third branches of the group F, N, P, Q and R, in which the magnitude of stress vector decreases in the early period of the third branch, shown in Fig. 7.5. The differences correspond to the experimental results in which a strain-anisotropy analogous to the Bauschinger effect appears along the third branch in the latter group and decreases with an increase of s_1. The functional relations for these characteristics relating to s_1 were obtained as follows:

$$z_{c\beta}: \quad a(s_1)=5.26\times10^{-1}(1-0.6067e^{-89.45s_1}),$$

and for the grop F, N, P, Q and R

$$\mu_c(s_1)/3=[9.8(1-e^{-314s_1})+14.7]-3106.6s_1e^{-250s_1} \quad \text{(GPa)},$$

$$z_{c\alpha}=z_{c\gamma}: \quad a(s_1)=(7.047e^{-s_1}+7.103)\times10^{-3},$$

$$b(s_1)=-0.4682s_1+2.611,$$

$$c(s_1)=-0.0341s_1+0.4297.$$

The values of μ and z obtained from the experimental results along the strain trajectories in the group G through J and the group F, N, P, Q and R are summarized in the following tables.

These values have been determined from the experimental results with $s_0=1.5$ percent. However, the values relating to the second and third branches may be functions of s_0 in general. On the other hand, it has been ascertained that the experimental results along the second branch for $s_0=1.17$, 2.2 and 3.2 percent obtained in the previous experiment[22] are approximated with high accuracy by using the values shown in Table 7.1. This verifies the well-known property that

Table 7.1 Values of μ and z for the first and second branches

μ (GPa)	z	a	b	c
$\mu_a=137.2$	z_a	3.38×10^{-3}	0.266	8.34×10^{-3}
$\mu_b=73.5$	$z_{b\beta}$	5.26×10^{-3}	0	0
	$z_{b\beta}$	5.98×10^{-3}	0.246	7.03×10^{-3}

Table 7.2 Values of μ and z for the third branch: Group G through J

μ_c (GPa)	z	s_1 (%)	a	b	c
98.1	$z_{c\alpha}=z_{c\gamma}$		4.64×10^{-3}	0.259	8.12×10^{-3}
	$z_{c\beta}$	0.25	2.71×10^{-3}	0	0
		0.5	3.47×10^{-3}	0	0
		1.0	3.92×10^{-3}	0	0
		2.0	4.76×10^{-3}	0	0

Table 7. 3 Values of μ and z for the third branch: Group F, N, P, Q and R

s_1 (%)	μ_c (GPa)	z	a	b	c
0	44.1	$z_{c\alpha}=z_{cr}$	13.92×10^{-3}	4.28×10^{-2}	2.59×10^{-2}
		$z_{c\beta}$	1.75×10^{-3}	0	0
0.25	47.53	$z_{c\alpha}=z_{cr}$	12.74×10^{-3}	4.20×10^{-2}	2.51×10^{-2}
		$z_{c\beta}$	2.71×10^{-3}	0	0
0.50	53.9	$z_{c\alpha}=z_{cr}$	11.32×10^{-3}	4.15×10^{-2}	2.39×10^{-2}
		$z_{c\beta}$	3.47×10^{-3}	0	0
1.0	64.68	$z_{c\alpha}=z_{cr}$	9.41×10^{-3}	3.98×10^{-2}	2.14×10^{-2}
		$z_{c\beta}$	3.92×10^{-3}	0	0
2.0	74.5	$z_{c\alpha}=z_{cr}$	8.03×10^{-3}	3.60×10^{-2}	1.67×10^{-2}
		$z_{c\beta}$	4.76×10^{-3}	0	0

the effect of pre-strain s_0 saturates for pre-strain of $s_0>1$ percent.

7. 2. 4. Comparison of theoretical results with experimental ones

By using characteristic values determined above, after the saturation of pre-strain s_0, stress-strain relations may be realized for arbitrary deformations of brass along the above-mentioned strain trajectories for any amount of s_1. Moreover, since the modification of the third invariant has been conducted on the stress value, the stress-strain relation thus obtained holds for any strain trajectory of the same geometry oriented in any direction in three-dimensional vector space $(e_{11},\ (2/\sqrt{3})(e_{11}/2+e_{22}),\ (2/\sqrt{3})e_{12})$.

Corresponding stress values expected to be measured in the experiment may be obtained by restoring the effect of third invariant from the stress value calculated by the above formulas. The stress-strain relations established above are compared with the corresponding experimental results by using the following figures.

The relation between the value $\sigma_{11}=(3/2)S_{11}$ or $\sqrt{3}\sigma_{12}=\sqrt{3}S_{12}$ and the arc length $\Delta s=s-s_0$ relating to $s_0\leq s$ for the group G through J is shown in Fig. 7.6

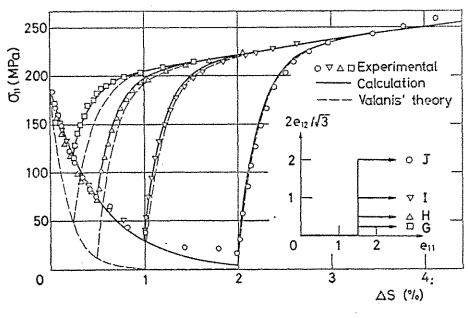

Fig. 7. 6 Comparison of calculated results with experimental ones for the trajectories G through J (stress component σ_{11}).

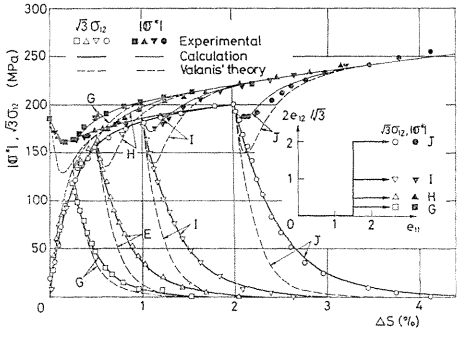

Fig. 7. 7 Comparison of calculated results with experimental ones for the trajectories G through J ($|\boldsymbol{\sigma}|$ and $\sqrt{3}\sigma_{12}$).

or 7.7. The thick solid curve corresponds to the calculated result, and the various kinds of point show the corresponding experimental ones along the trajectories indicated by the inserted figure. The thin solid curves in Fig. 7.7 show the relation between the resultant modified stress intensity $|\sigma^*|=\sqrt{\sigma_{11}^{*2}+3\sigma_{12}^2}$ and Δs found from the thick curves in Figs. 7.6 and 7.7. Figures 7.8 and 7.9 show analogous curves for the group F, N, P, Q and R as compared with the corresponding experimental results. As found from these figures, the calculated results may approximate the corresponding experimental ones with high accuracy.

The dashed curves in Figs. 7.6 and 7.7 show the restlts calculated by Valanis' method[27] mentioned above briefly. There are considerable differences between the solid and dashed curves.

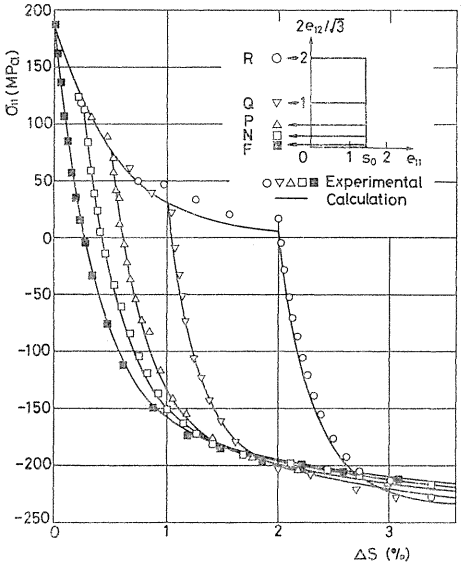

Fig. 7.8 Comparison of calculated results (σ_{11}) with experimental ones for the trajectories F, N, P, Q and R.

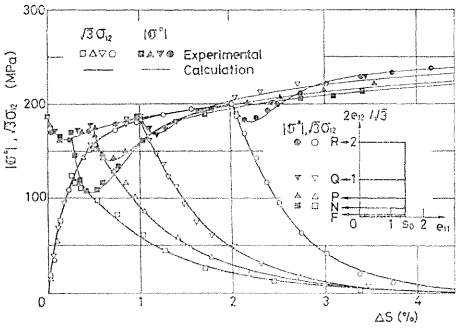

Fig. 7.9 Comparison of calculated results ($|\sigma|$ and $\sqrt{3}\sigma_{12}$) with experimental ones for the trajectories F, N, P, Q and R.

7. 2. 5. Relation between fading memory and limit of integration

As found from the experimental results, the stress-strain relations of materials just after the corner of the strain trajectory are subjected to a severe history effect and the effect decreases thereafter with an increase of deformation without severe history effect. In other words, the deformation property accompanying the preceding plastic deformation is altered by the change in microscopic structure of materials due to the succeding plastic deformation, and thus the memory of history effect declines with the succeeding plastic deformation. By taking this trend into account, Ilyushin proposed Eq. (7.25) instead of (7.24). Suitable choice of the length h (trace of delay) included in Eq. (7.25) has a significant meaning for effective use of the stress-strain relation obtained above in accurate analyses of plastic deformation of structures, thus a reasonable estimation of the length h will be discussed in the following.

When the trend of fading memory is assumed in a form of the exponential type, the effect of preceding disturbance to the instant considered, though it decreases with an increase of the interval between the relevant two instants, does

not vanish completely for any finite interval. Thus the concept of the "trace of delay" is an approximation and the length h may be regarded to depend on deformation history as well as on materials. The length h should be determined in complying with the accuracy required for the calculated results. On the other hand, this concept is very effective for simplifying calculations for complicated history, and thus the necessity to discuss the relation between h and the accuracy of corresponding calculation should be emphasized for establishing the general plastic theory.

In the following, the relation is discussed according to the examples mentioned above.

7. 2. 5. 1. Stress-strain relation within the length h along the orthogonal tri-linear strain trajectories in two-dimensinal vector space

The stress-strain relation within the length h may be expressed in the following manner.

Along the first branch:

$$S_{11}(s)=\frac{2}{3}\mu_a e^{-z_a(s)}\int_{s-h}^{s} e^{z_a(s')}\frac{de_{11}}{ds'}ds'. \tag{7.50}$$

Along the second branch:

$$S_{11}(s)=\begin{cases}\dfrac{2}{3}\mu_b e^{-z_{b\alpha}(s)}\displaystyle\int_{s-h}^{s_0} e^{z_{b\alpha}(s')}\frac{de_{11}}{ds'}ds' & (s-h\leq s_0),\\ 0 & (s_0\leq s-h)\ ;\end{cases}$$

$$S_{12}(s)=\begin{cases}\dfrac{2}{3}\mu_b e^{-z_{b\beta}(s)}\displaystyle\int_{s_0}^{s} e^{z_{b\beta}(s')}\frac{de_{12}}{ds'}ds' & (s-h\leq s_0),\\ \dfrac{2}{3}\mu_b e^{-z_{b\beta}(s)}\displaystyle\int_{s-h}^{s} e^{z_{b\beta}(s')}\frac{de_{12}}{ds'}ds' & (s_0\leq s-h).\end{cases} \tag{7.51}$$

When the value of S_{11} concerning h at $s=s_0$ is indicated by a symbol σ_0', σ_0' is known from Eq. (7.50), and the following expression

$$\int_{s_0-h}^{s_0} e^{z_{b\alpha}(s')}\frac{de_{11}}{ds'}ds'=\frac{3\sigma_0'}{2\mu_b}e^{z_{b\alpha}(s_0)} \tag{7.52}$$

may be found from the relation

$$\sigma_0'=\frac{2}{3}\mu_b e^{-z_{b\alpha}(s_0)}\int_{s_0-h}^{s_0} e^{z_{b\alpha}(s')}\frac{de_{11}}{ds'}ds'$$

obtained from Eq. $(7.51)_1$. By substituting Eq. (7.52) into (7.51), the following relations may be obtained:

$$S_{11}(s)=\begin{cases}\sigma_0' e^{-\{z_{b\alpha}(s)-z_{b\alpha}(s_0)\}}\left[1-\displaystyle\int_{s_0-h}^{s-h} e^{z_{b\alpha}(s')}\frac{de_{11}}{ds'}ds'\Big/\int_{s_0-h}^{s_0} e^{z_{b\alpha}(s')}\frac{de_{11}}{ds'}ds'\right] & (s-h\leq s_0),\\ 0 & (s_0\leq s-h)\ ;\end{cases}$$

$$S_{12}(s)=\begin{cases}\dfrac{2}{3}\mu_b e^{-z_{b\beta}(s)}\displaystyle\int_{s_0}^{s} e^{z_{b\beta}(s')}\frac{de_{12}}{ds'}ds' & (s-h\leq s_0),\\ \dfrac{2}{3}\mu_b e^{-z_{b\beta}(s)}\displaystyle\int_{s-h}^{s} e^{z_{b\beta}(s')}\frac{de_{12}}{ds'}ds' & (s_0\leq s-h).\end{cases}$$

(7.53)

In the same manner, the following relations are obtained along the third branch:

$$S_{11}(s)=\sigma_1' e^{-\{z_{c\alpha}(s)-z_{c\alpha}(s_0+s_1)\}}\left[1-\int_{s_0+s_1-h}^{s-h} e^{z_{c\alpha}(s)}\frac{de_{11}}{ds'}ds'\Big/\int_{s_0+s_1-h}^{s_0} e^{z_{c\alpha}(s')}\frac{de_{11}}{ds'}ds'\right]$$

$$+\frac{2}{3}\mu_c e^{-z_{c\tau}(s)}\int_{s_0+s_1}^{s} e^{z_{c\tau}(s')}\frac{de_{11}}{ds'}ds' \qquad (s-h\leq s_0),$$

$$S_{11}(s)=\frac{2}{3}\mu_c e^{-z_{c\tau}(s)}\int_{s_0+s_1}^{s} e^{z_{c\tau}(s')}\frac{de_{11}}{ds'}ds' \qquad (s_0\leq s-h\leq s_0+s_1),$$

$$S_{11}(s)=\frac{2}{3}\mu_c e^{-z_{c\tau}(s)}\int_{s-h}^{s} e^{z_{c\tau}(s')}\frac{de_{11}}{ds'}ds' \qquad (s_0+s_1\leq s-h);$$

$$S_{12}(s)=\tau_1 e^{-\{z_{c\beta}(s)-z_{c\beta}(s_0+s_1)\}} \qquad (s-h\leq s_0),$$

$$S_{12}(s)=\tau_1' e^{-\{z_{c\beta}(s)-z_{c\beta}(s_0+s_1)\}}\left[1-\int_{s_0+s_1-h}^{s-h} e^{z_{c\beta}(s')}\frac{de_{12}}{ds'}ds'\Big/\int_{s_0+s_1-h}^{s_0+s_1} e^{z_{c\beta}(s')}\frac{de_{12}}{ds'}ds'\right]$$

$$(s_0<s-h\leq s_0+s_1),$$

$$S_{12}(s)=0 \qquad (s_0+s_1\leq s-h),$$

(7.54)

where σ_1' and τ_1' are expressed as follows:

$$\sigma_1'=\frac{2}{3}\mu_c e^{-z_{c\alpha}(s_0+s_1)}\int_{s_0+s_1-h}^{s_0} e^{z_{c\alpha}(s')}\frac{de_{11}}{ds'}ds',$$

$$\tau_1'=\frac{2}{3}\mu_c e^{-z_{c\beta}(s_0+s_1)}\int_{s_0+s_1-h}^{s_0+s_1} e^{z_{c\beta}(s')}\frac{de_{12}}{ds'}ds'. \qquad (7.55)$$

The corresponding values of μ and z in the above formulas are the same as those shown in Tables 7.1 through 7.3.

7. 2. 5. 2. Relation between the range of integration and accuracy of calculation

It is necessary to shorten the arc length h for simplifying calculation whereas it is desirable to take h as long as possible for improving the accuracy of calculation. In order to determine the arc length h for general application by taking these two points of view into account, stress components were calculated along the trajectories of the group G through J in relation to four values of h (=0.5, 1.0, 1.5, and 2.0 %), for example. As examples of the results obtained, Figs. 7.10 and

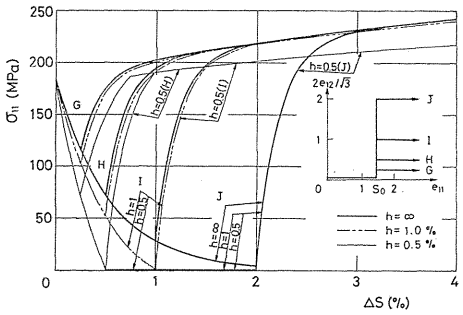

Fig. 7. 10 Relation between the range of integration and accuracy of calculation ($h = \infty$, 1.0 and 0.5% for σ_{11}).

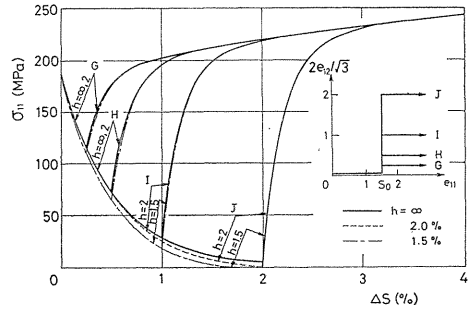

Fig. 7. 11 Relation between the range of integration and accuracy of calculation ($h = \infty$, 2.0 and 1.5% for σ_{11}).

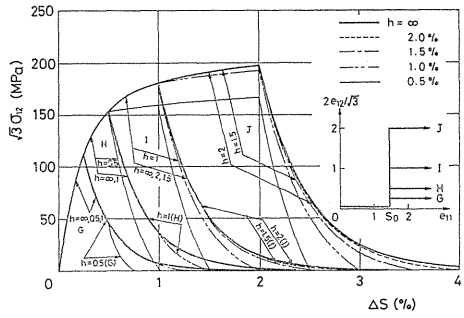

Fig. 7. 12 Relation between the range of integration and accuracy of calculation ($h=\infty$, 1.5, 1.0 and 0.5% for $\sqrt{3}\sigma_{12}$).

7.11 show the relations between $\sigma_{11}=(3/2)S_{11}$ and the arc length Δs after the first corner of the trajectories. Moreover, Fig. 7.12 shows analogous relations between $\sqrt{3}\sigma_{12}$ and Δs. In these figures, the results of calculation without considering the trace of delay ($h\to\infty$) are shown by the solid curves, and the results for $h=2.0$, 1.5, 1.0 and 0.5 percent correspond to the dashed curve, dash-dot curve, double-dot and dashed curve and thin solid curve, respectively. In Fig. 7.12, the results relating to $h=1.5$ and 2.0 percent almost coincide with those for $h\to\infty$ along the trajectories G and H for $s_1=0.25$ and 0.5 percent, and these results are not entered in the figure.

As found from Figs. 7.10 and 7.12, there is a considerable difference between the results relating to $h=0.5$ or 1.0 percent and $h\to\infty$. However, it is found from Figs. 7.11 and 7.12 that the results relating to $h=1.5$ and 2.0 percent agree well with the results relating to $h\to\infty$. Judging from these results, it may be concluded that the accuracy of calculation is not sufficient for practical use and depends on the geometry of trajectory for a length h less than 1.5 percent, but it is sufficient for estimating stress value independently of the geometry of the strain trajectory for a length h longer than 1.5 percent.

7. 3. Stress-sttain relation according to local determinability

As mentioned above, the stress-strain relation in the form of tensorial equation and that of integral type are very complicated for deformations along the strain

trajectories of complicated geometry. However, it is preferable to formulate the relation as simply as possible even for accurate defomation analyses of engineering structure, if it would be of sufficient accuracy to represent the complicated history effect on the deformation behaviour. The hypothesis of local determinability proposed by Lensky[29,30] is worth noting from this point of view.

7. 3. 1. Hypothesis of local determinability

The hypothesis of local determinability[29] has been formulated first for the strain trajectories consisting of straight segments as follows:

$$\frac{\partial}{\partial s}\theta_i=f_i(\theta_1,\ \cdots,\ \theta_5;\ s),\quad (\cos\theta_i)(\cos\theta_i)=1\quad (i=1,\ 2,\ \cdots,\ 5). \tag{7.56a}$$

As Lensky has pointed out, the hypothesis should be expressed in general in the form[30]

$$\frac{\partial}{\partial s}\theta_i=f_i(\theta_k,\ \kappa_m(s);\ s),\quad (\cos\theta_i)(\cos\theta_i)=1$$

$$(i,\ k=1,\ 2,\ \cdots,\ 5;\ m=1,\ 2,\ 3,\ 4) \tag{7.56b}$$

along the strain trajectory of arbitrary shape, where $\kappa_m(s)$ are the geometric parameters of the trajectory.

Lensky has confirmed experimentally that the relation

$$\frac{d\theta}{ds}=f(\theta,\ s),\quad \cos=\boldsymbol{\sigma}\cdot d\boldsymbol{e}/|\boldsymbol{\sigma}||d\boldsymbol{e}| \tag{7.57}$$

holds in the plastic deformation of an alloyed steel ХГСА along the orthogonal bi-linear strain trajectory[29]. Equation (7.57) is a simplest case of Eq. (7.56a). However, in order to confirm Eq. (7.57) may hold along the straight-line trajectory independently of the shape of preceding trajectory, it is necessary to discuss this experimentlly for a variety of deformation histories with preceding curved parts of arbitrary curvature or bi-linear ones with arbitrary corner-angle. For this purpose, the hypothesis is discussed by the experimental results obtained hereto. Figure 6. 23 obtained for the brass BsBM2 suggests a possibility of this hypothesis. Figure 6. 32 for the mild steel S10C also has a regularity in the relation between θ^*_σ and Δs. The hypothesis will be discussed in some detail in the following.

7. 3. 1. 1. Bi-linear strain trajectories with arbitrary corner-angle[31]

The relations between the angle of delay θ and the arc length Δs after the corner for the deformation of mild steel S10C along the bi-linear trajectories shown in the inset figure in Fig. 7. 13 are shown in Fig. 7. 14. As shown in Fig. 7. 14, the relations for $\theta_0=30°$ and $-30°$ (θ_0: corner angle measured clockwise) agree well with each other for $s_0=2$ and 3 percent. Such a feature may be observed also for $\theta_0=60°$ and $-60°$. Thus, it may be said that the relation $\theta\sim\Delta s$ for the complex loading is independent of the sequence of loading as well as the amount of pre-strain, and depends only on the value of corner-angle θ_0. Further, the relations for $\theta_0=\pm30°$ and $\pm60°$ shown in Fig. 7. 14 are transferred to those shown in Fig. 7. 13 so that the experimental point at the corner in each experiment may coincide with the corresponding experimental point on the solid curve showing the relation $\theta\sim\Delta s$ for

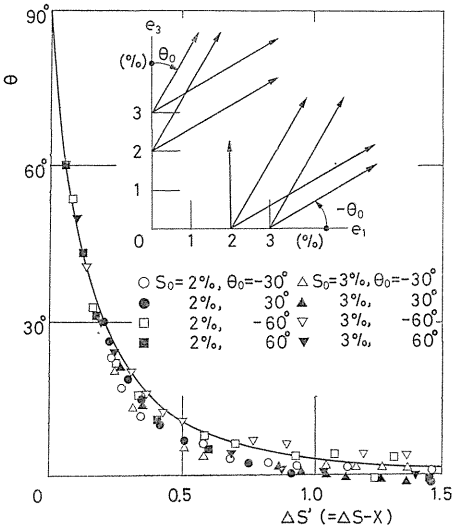

Fig. 7. 13 Relation $\theta\sim\Delta s'$ ($\Delta s'=s-x$; x: arc length transferred rightward) obtained by modifying the relation shown in Fig. 7. 14 (s_0: pre-strain).

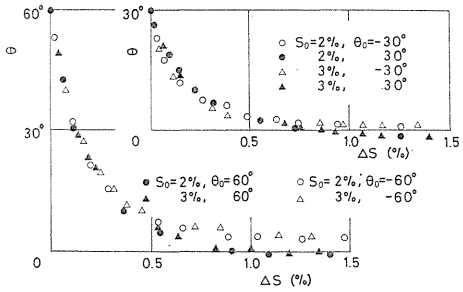

Fig. 7. 14 Relation $\theta\sim\Delta s$ after the corner on the bi-linear trajectories shown in the inset figure in Fig. 7. 13.

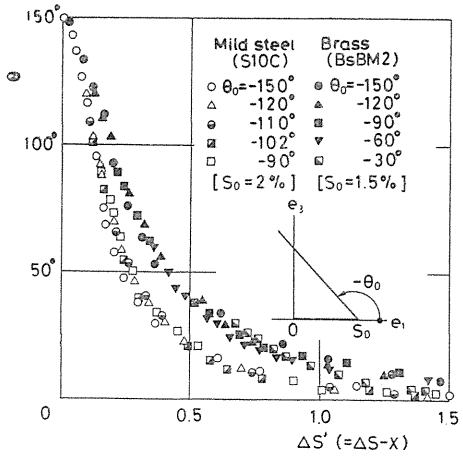

Fig. 7. 15 Relation $\theta\sim\Delta s'$ similar to that shown in Fig. 7. 13 for various corner-angles including obtuse angle.

$\theta_0=90°$. It is found from Fig. 7. 13 that the relations along the second branch agree well with each other and may be expressed by a unique curve, and the corner-angle θ_0 shows the beginning of the relevant part of this curve. In more detail, the relation $\theta\sim\Delta s$ is affected by the magnitude of s_0 for $s_0<2$ percent where the history effect is not yet saturated.

The feature found from Fig. 7. 13 has been obtained also for the case of $\theta_0>90°$. Figure 7. 15 shows the curves similar to those shown in Fig. 7. 13 obtained by the experiments for mild steel S10C and brass BsBM2. As shown in Fig. 7. 15, the above mentioned feature also appears clearly in these cases. Further, it is worth noting that the curve for mild steel appears lower than that for brass.

7. 3. 1. 2. Orthogonal bi-linear trajectories with rounded corner[31]

The relation $\theta\sim\Delta s$ for brass BsBM2 after the biginning point P_0 of circular arc has been shown in Fig. 6. 35. The similar relation for the mild steel S10C is shown in Fig. 7. 16 for the trajectories in the inset figure. As found from these figures, the magnitude of θ increases from the point P_0 along the circular trajectory, and the rate of increase is larger for larger value of curvature. Further, the value of θ turns to decrease at the end-point P_1 of the arc, decreases quickly at first, and

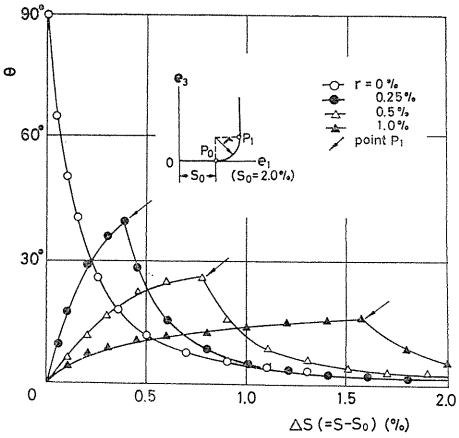

Fig. 7. 16 Relation $\theta \sim \Delta s$ after the point P_0 on the strain trajectory with rounded corner for mild steel S10C.

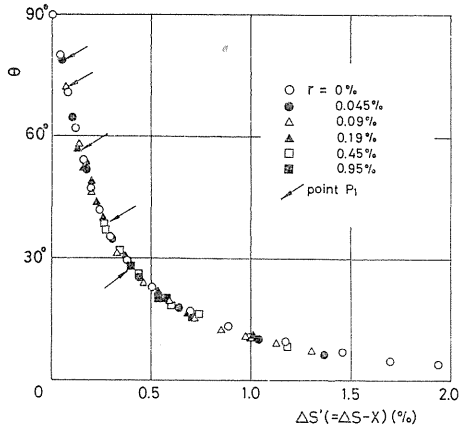

Fig. 7. 17 Relation $\theta \sim \Delta s'$ ($\Delta s' = s - x$; x: arc length transferred leftward) obtained by modifying the relation thown in Fig. 6. 35.

tends to zero slowly thereafter.

The part after the point P_1 of the curve for every value of radius r shown in Fig. 6. 35 is transferred in Fig. 7. 17 so that the value of θ at the point P_1 may coincide with that on the curve for $r=0$. As found from Fig. 7. 17, these parts agree well with each other and may express by a unique curve. In other words, the effect of the different shapes of the trajectories preceding the point P_1 on the plastic deformation along the straight-line trajectory after the point P_1 are expressed only by the magnitudes of θ at the point P_1 and are not transmitted to the relation $\theta \sim \Delta s$ after this point. This may be regarded as an important feature of the plastic deformation.

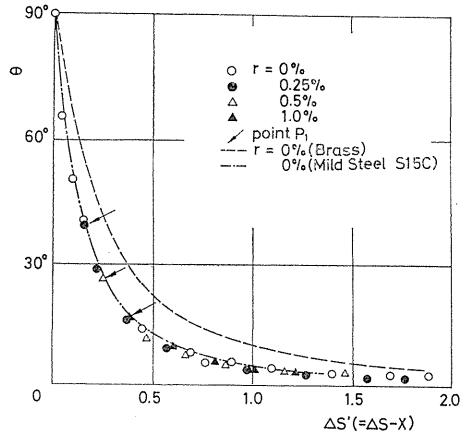

Fig. 7. 18 Relation $\theta \sim \Delta s'$ ($\Delta s' = s - x$; x: arc length transferred leftward) obtained by modifying the relation shown in Fig. 7. 16.

Figure 7. 18 shows the similar relation as mentioned above for the mild steel S10C derived from Fig. 7. 16. As found from this figure, a feature similar to that for brass may be observed also for mild steel. In Fig. 7. 18, the relation for brass shown in Fig. 7. 17 is indicated by the dashed curve. In comparing these relations, it is found that the decreasing rate of θ for mild steel is larger than that for brass. Further, it is found from the comparison of the relations shown in Figs. 6. 35 and 7. 16 that the magnitude of θ for mild steel appears smaller than that for brass. The dash-dot curve in Fig. 7. 18 shows the similar relation for the mild steel S15C in the case of $r=0$, which may be regarded as coinciding well with that for the mild steel S10C.

7. 3. 1. 3. Straight-line trajectories after a trajectory of arbitrary shape[31]

In order to confirm the hypothesis of local determinability from an opposite point of view, the feature of plastic deformation is discussed for the experimental result on the deformation of the mild steel S15C along the straight-line trajectory, after the trajectory is turned instantly so as to give the assigned values of θ ($\equiv \arccos[\boldsymbol{\sigma}\cdot d\boldsymbol{e}/|\boldsymbol{\sigma}||d\boldsymbol{e}|]$) with respect to the direction of the stress vector $\boldsymbol{\sigma}$ at an arbitrary point on an optional strain trajectory. In assigning the optional trajectory preceding the straight-line part, the arbitrariness was restricted as follows.

(i) In order to consider the strain-hardening range where the effect of pre-strain on the deformation behaviour is saturated sufficiently and the elastic strain-increment may be negligible in comparison with the plastic one, the arc length of the preceding optional part should have a sufficiently large value.

(ii) Unloading should not be included in the preceding optional part.

(iii) The value of $\boldsymbol{\sigma}$ should be sufficiently large at the end of the optional part.

Figure 7. 19 shows a strain trajectory of arbitrary shape selected in such a way. In this figure, the preceding part OP in the strain vector space (e_{11}, $2e_{12}/\sqrt{3}$; where e_{11} and e_{12} are the axial and shear strain deviators for the tubular specimen) consists of a circular arc with radius 1 percent concave upward starting at the origin ($s=s_a=2\%$, $s=\int\{(de_{11})^2+(2de_{12}/\sqrt{3})^2\}^{1/2}$) and a succeeding circular arc with radius 0.4 percent convex upward ($s_b=0.5\%$), and has a common pre-strain ($s=s_a+s_b=2.5\%$ at the point P) for every experiment.

The strain-increment vector $d\boldsymbol{e}(\equiv de_{11}\boldsymbol{n}_1+(2de_{12}/\sqrt{3})\boldsymbol{n}_3$, where de_{11} and de_{12} are the components of strain-increment, and $\boldsymbol{n}_1$ and $\boldsymbol{n}_3$ the orthonormal base vectors) is turned instantly at the point P so as to give the value shown in Table 7.4 (defined positive clockwise) with respect to the stress vector $\boldsymbol{\sigma}(\equiv\sigma_{11}\boldsymbol{n}_1+\sqrt{3}\sigma_{12}\boldsymbol{n}_3$, where σ_{11} and σ_{12} are the axial and shear stress components for the specimen) at the point P on the trajectory and goes forward in that direction. These cases are called experiments 1, 2, 3, 4, $\bar{2}$, $\bar{3}$ and $\bar{4}$, respectively. Further, an

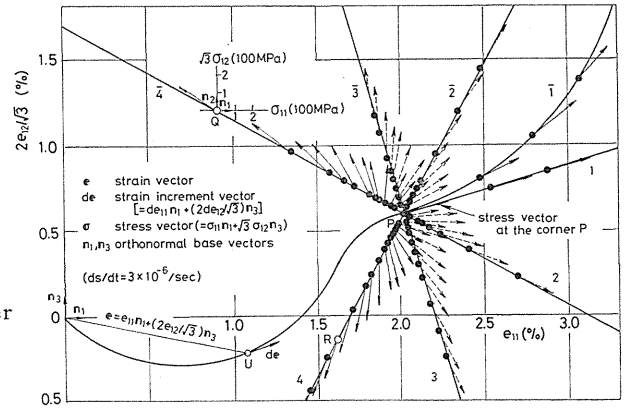

Fig. 7. 19 Strain trajectories after an optional part.

Table 7. 4 Assigned value of θ at the point P

Experiment No.	1	2	3	4	$\bar{2}$	$\bar{3}$	$\bar{4}$
θ	0°	45°	90°	135°	−45°	−90°	−135°

experiment $\bar{1}$ is supplemented to examine the deformation along the trajectory with a small curvature (a circular arc with radius 2% concave upward) after the direction of $d\boldsymbol{e}$ is turned to coincide with that of $\boldsymbol{\sigma}$ at the point P. The trajectories corresponding to these experiments are given in Fig. 7.19 by the solid lines. The strain-rate along these trajectories was selected as $ds/dt=3\times10^{-6}$/sec.

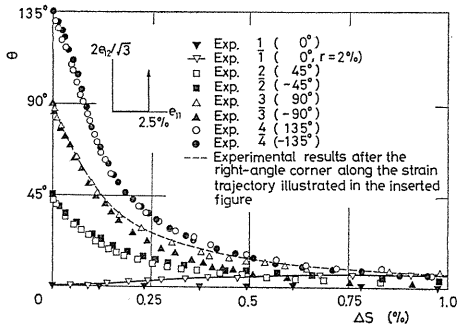

Fing. 7. 20 Relations $\theta\sim\Delta s$ along the straight part after the end point P of the optional part.

Figure 7.20 shows the relation $\theta\sim\Delta s$ (Δs: arc length after the point P) in the deformation along each trajectory after the point P. In the figure, the dashed curve corresponds to the relation for the deformation along the bi-linear trajectory shown in the inset figure. As found from the result of experiment 1, if the condition $\theta=0°$ is given at the point P, then the condition is maintained almost completely for the subsequent deformation along the straight-line part in that direction. Further, in the result of experiment $\bar{1}$, though the value of θ increses slightly with increase of Δs, it may be regarded as being saturated within the range $\theta<6°$. Therefore, it may be said that the effect of complex loading on the angle θ can be cancelled out with the condition $\theta=0°$.

As shown in Fig. 7.20, the relations $\theta\sim\Delta s$ for the experiments 2 and $\bar{2}$, 3 and $\bar{3}$ as well as 4 and $\bar{4}$ respectively agree well with each other. Thus, it may be said that the relation $\theta\sim\Delta s$ after the point P depends only on the absolute value of θ at the point P. Further, the relations $\theta\sim\Delta s$ for experiments 3 and $\bar{3}$ agree well with that for the orthogonal bi-linear trajectory. Thus, it may be concluded from the above-mentioned feature that the relation $\theta\sim\Delta s$ in the deformation along the straight-line trajectory after the point P depends only on the value θ at the point P, independently of the shape and the relative arrangement of the preceding trajectory. To make sure, it is necessary to note that the value of θ at the point P is related not only to the history effect of the preceding deformation but also the instant rotation of the vector $\boldsymbol{\sigma}$ or $d\boldsymbol{e}$ at that point, that is, an instant variation of the loading or deformation state.

As shown in Fig. 7.21, when the results of the experiments 2, $\bar{2}$ and 3, $\bar{3}$ shown in Fig. 7.20 are transferred rightward so that the experimental point at the point P in each experiment may coincide with the corresponding experimental point of the experiments 4, $\bar{4}$, these results are now found to coincide on the whole with the results of experiments 4 and $\bar{4}$.

From this experimental evidence, it may be said that the relation $\theta\sim\Delta s'(\Delta s'=\Delta s-x$, where x denotes an arc length transferred rightward) for the deformation along each subsequent straght-line trajectory can be expressed by a unique curve,

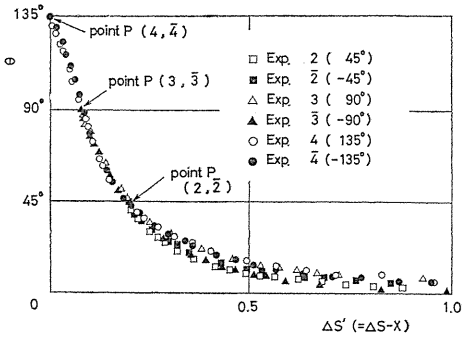

Fig. 7. 21 Relation $\theta\sim\Delta s'$ ($\Delta s'=s-x$; x: arc length transferred rightward) obtained dy modifying the relation shown in Fig. 7. 20.

and the corresponding part of the curve is determined by the value of θ at the beginning point P of the trajectory. From a comparison of the dash-dot curve shown in Fig. 7. 18 with the relation shown in Fig. 7. 21, it is found that the former is simply a part of the latter.

From the experimental results mentioned above, it may be concluded that the history effect due to the preceding inelastic deformation, whatever it may be complicated, is represented only by the amount of θ at each point on the trejectory, and the fading rate of the history effect is determined uniquely along the succeeding trajectory. This trend may be regarded as an important suggestion to systematize the complicated variation of microscopic structure in metals under inelastic deformation.

7. 3. 1. 4. Orthogonal tri-linear strain trajectory in three-dimensional vector space[26]

In order to express the trend in the relation $\theta\sim\Delta s$(Δs: arc length after the first corner point A in Fig. 6. 41) on the deformation of mild steel S15C along the orthogonal tri-linear strain trajecotry in the three-dimensional vector space, according to the results obtained from the experiments in Section 6. 5. 2, two kinds of angle ψ and χ are introduced. When an orthogonal coordinate system is established together with base vectors $\boldsymbol{t}$, $\boldsymbol{n}$ in the directions of the third and second branches and $\boldsymbol{b}$ in the direction perpendicular to a plane including these two branches, relations between these angles and the corresponding stress components σ_t^*, σ_n^* and σ_b^*, modified by using the coefficient R, may be determined as in the following.

$$\boldsymbol{t}=\cos\theta_e\boldsymbol{n}_3-\sin\theta_e\boldsymbol{n}_1,\quad \boldsymbol{n}=\boldsymbol{n}_2,\quad \boldsymbol{b}=\boldsymbol{n}\times\boldsymbol{t},$$

$$\sigma^*=\sigma_t^*\boldsymbol{t}+\sigma_n^*\boldsymbol{n}+\sigma_b^*\boldsymbol{b},$$

$$\tan\psi=\sigma_n^*/\sigma_t^*,\quad \tan\chi=\sigma_b^*/\sigma_t^*, \tag{7.58}$$

where $\boldsymbol{n}_1$, $\boldsymbol{n}_2$ and $\boldsymbol{n}_3$ are the base vectors in the directions of e_1–, e_2– and e_3–axes. Thus, the angles ψ and χ may be regarded as the angles showing the decreasing rates of stress components owing to the histories of the second and first branches with a development of deformation along the third branch, respectively.

As an example, the relations between the angle ψ and the length s_2 of the third branch measured from the point B are shown in Fig. 7. 22 for $s_1=0.25$ percent.

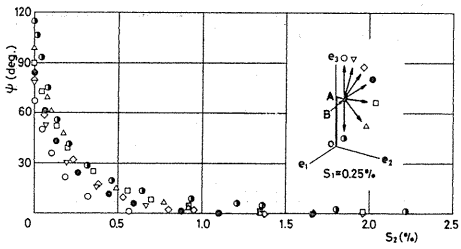

Fig. 7. 22 Relation between angle ψ and the arc length $s_2(s_1=0.25\%)$.

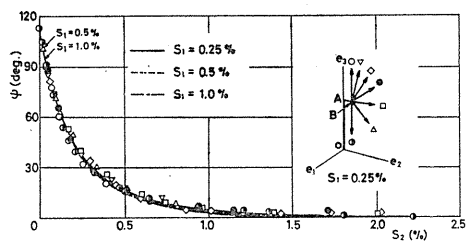

Fig. 7. 23 Relation between angle ψ and the arc length s_2 obtained by modifying the relation shown in Fig. 7. 22.

As found from the figure, though an angle ψ_I (ψ at the point B) appears larger for larger value of θ_e, the value of ψ seems to decrease in the same trend with an increase of s_2 for every case. Thus, if a relation $\psi\sim s_2$ for each value of θ_e is transferred with respect to that for $\theta_e=180°$ so that the value of ψ_I in the former coincides with the value of ψ on the relation $\psi\sim s_2$ for $\theta_e=180°$, Fig. 7. 23 may be obtained. As found from the figure, various symbols corresponding to the values of θ_e may be found on a unique solid curve. From this fact, it may be regarded as that the angle θ_e affects only on the value of ψ_I, and the decreasing rate of ψ with an increase of s_2 is not affected by θ_e. In Fig. 7. 23, curves for $s_1=0.5$ and 1. 0 percent obtained by the above-mentioned procedure are entered with the dashed and dash-dot curves so that the value of ψ_I in these curves coincide with the value of ψ (shown with the arrows) on the solid curve. The curves for various values of s_1 agree well with each other, and thus it may be concluded that the decreasing property of ψ with the increase of s_2 is affected by neither the angle θ_e nor the length s_1. As the value of ψ tends to a certain value different from zero for sufficiently large value of s_2, such a deviation will be taken into account in the following formulation.

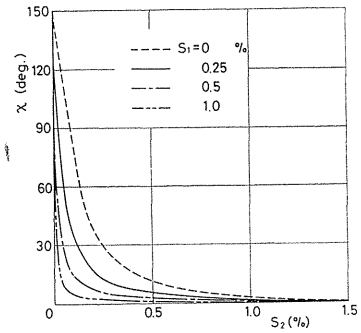

Fig. 7. 24 Relation between the angle χ and the arc length s_2 after modification.

Also for the angle χ, the relations $\chi\sim s_2$ for various values of θ_e may be confirmed to agree well with each other for each assigned value of s_1, by using the procedure mentioned above for the angle ψ. Curves obtained in such a way are shown in Fig. 7. 24 for each value of s_1. As found from the figure, a decreasing rate of χ with an increase of s_2 becomes more quickly for large value of s_1, and the curve $\chi\sim s_2$ may be supposed to tend to the coordinate axes for sufficiently large value of s_1. Furthermore, it is found that the curve $\chi\sim s_2$ for $s_1=0$ percent coincide with the curve $\psi\sim s_2$. Thus, each of the curves $\chi\sim s_2$ forms a group varying from the curve $\psi\sim s_2$ to the coordinate axes with the variation of s_1.

The following relations may be selected as those satisfying the features of experimental results mentioned above.

$$\psi=\operatorname{arccot}\{A(0)s_2+\cot(\psi_I+\psi_\infty)\}-\psi_\infty,$$
$$\chi=\operatorname{arccot}\{A(s_1)s_2+\cot(\chi_I+\chi_\infty)\}-\chi_\infty. \tag{7.59}$$

In Eq. (7.59), $\cot(\varphi+\psi_\infty)$ or $\cot(\chi+\chi_\infty)$ is expressed as a linear function of s_2. Thus the value of ψ_∞ or χ_∞ is estimated so that the value of $\cot(\psi+\psi_\infty)$ or $\cot(\chi+\chi_\infty)$ together with the value of ψ or χ found by the experiment may have a linear relation with respect to the value of s_2. In the result, it is found that ψ_∞ is related with s_1 and θ_e by means of the following relation.

$$\psi_\infty=\{90s_1\exp(-4.4s_1)+5.5\}\{1-(\theta_e/185)^2\}^{1/2}, \tag{7.60}$$

where s_1 and θ_e show numerals in percent and degree, respectively. Since the value of χ_∞ is found to be sufficiently small in comparing with that of ψ_∞, it is neglected in this formulation. A function $A(s_1)$ may be estimated from a gradient of straight line showing the relation between $\cot(\psi+\psi_\infty)$ or $\cot(\chi+\chi_\infty)$ and s_2, which may be approximated by the following relation.

$$A(s_1)=16.9\exp(2.26s_1)-11.2. \tag{7.61}$$

In the next, a relation between ψ_I or χ_I and the angle θ_e may be obtained from the relation between the directions of the modified stress vector $\boldsymbol{\sigma}^*$ and the third branch at the point B. Angles α and β expressing the direction of $\boldsymbol{\sigma}^*$ at the point B are defined as follows;

$$\alpha=\arctan(\sigma_3^*/\sigma_2^*),\quad \beta=\arctan\{\sigma_1^*/(\sigma_2^{*2}+\sigma_3^{*2})^{1/2}\}, \tag{7.62}$$

where σ_1^*, σ_2^* and σ_3^* are components of $\boldsymbol{\sigma}^*$ in the directions of $\boldsymbol{n}_1$, $\boldsymbol{n}_2$ and $\boldsymbol{n}_3$. It is found that the relation between α or β and the length s_1 of the second branch measured from the point A is approximated by the following relation with sufficient accuracy.

$$\alpha=\operatorname{arccot}(8.90s_1),\quad \beta=-109\exp(-5.5s_1)-2.37. \tag{7.63}$$

By using the angles α and β, the relation between the angle ψ_I or χ_I and the angle θ_e can be expressed in the following form:

$$\psi_I=\operatorname{arccot}(\cos\theta_e\tan\alpha-\sin\theta_e\sec\alpha\tan\beta),$$
$$\chi_I=\theta_e+\arctan(\tan\beta/\sin\alpha). \tag{7.64}$$

The values of ψ and χ may be calculated by using Eq.(7.59) together with the relations (7.60), (7.61), (7.63) and (7.64).

An example of comparison of the results calculated by using the above-obtained relations with the corresponding experimental ones is shown in Fig. 7.25 in the case of $\theta_e=90°$. In the figure, the experimental results are shown by the various symbols in the inset table, and the calculated results of angles ψ and χ are entered by the solid and dashed curves. It is found that both results agree well with each other. Such a good agreement has been ascertained in every value of the angle θ_e.

Finally, each relation in Eq. (7.59) corresponds to a solution of either one in the following differential equations.

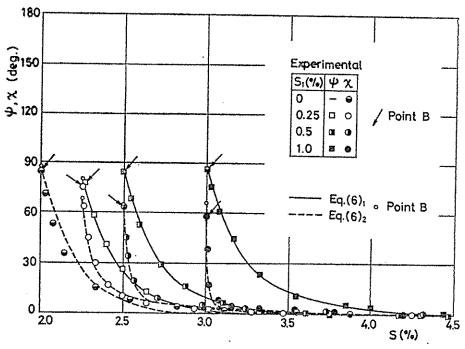

Fig. 7. 25 Comparison of calculated results with the corresponding experimental ones.

$$d(\psi+\psi_\infty)/ds=-A(0)\sin^2(\psi+\psi_\infty),$$
$$d(\chi+\chi_\infty)/ds=-A(s_1)\sin^2(\chi+\chi_\infty). \tag{7.65}$$

As found from Eq. (7.65), if the value of ψ or χ is measured from $-\psi_\infty$ or $-\chi_\infty$, the value of ψ or χ for $s_2\to\infty$, the former equation expresses the fact that the curve $\varphi\sim s_2$ may be determined by a function of the corresponding ordinate only, while the latter equation is a similar relation to that in the former for each value of s_1. If the small value ψ_∞ or χ_∞ is neglected in each of these equations, the following equations are obtained.

$$d\psi/ds=-A(0)\sin^2\psi,\quad d\chi/ds=-A(s_1)\sin^2\chi. \tag{7.66}$$

Each of these equations may be regarded as a specialized form of Eq. (7.56 a) along the orthogonal tri-linear strain trajectories in the three-dimensional space.

7. 3. 2. Estimation of the stress-strain relation using the hypothesis of local determinability

Experimental results mentioned above showed a regularity concerning the history effect and its fading property in the inelastic deformation of metals along the strain trajectories with complicated geometry. The regularity may be summarized as follows.

(i) The history effect on the deformation behaviour of metals arises from the geometry of strain trajectory, and its variation is represented by the geometric parameter of the trajectory showing the variation rate of deformation state.

(ii) The intensity of history effect at any point on the trajectory is represented by the angle of delay of the direction of stress vector from that of the strain trajectory at that point, whatever the geometry of the preceding part may be complicated, and the fading rate of history effect depends only on the angle of delay for the deformation along the succeeding trajectory.

Such a trend corrobolates the relation

$$\frac{d\theta}{ds}=f(\theta,\ s)+\kappa(s),\quad \theta:\text{ argle of delay},\quad \kappa(s)\text{ ; curvature} \tag{7.67}$$

proposed by Lensky[29] as a simplest form of Eq. (7.56 b) for the trajectory with arbitrary shape in the space V_{2e}. Since the angle θ in the space V_{2e} or the angle

ϕ and χ in the space V_{3e} (ref. Section 7.3.1.4) may represent the relation between the components and the intensity of stress vector, the relation between the components of stress and strain-increment may be found by using the variations of these angles along the trajectory as functions of the arc length s of the strain trajectory, if the relation between the intensities of stress and strain-increment vectors is given as a function of s.

On the other hand, the fundamental equations in the deformation analysis include the components of stress and strain or strain increment deviators, and thus the relation obtained above may be used as a constitutive equation of materials in reflecting the complicated history effects to close the fundamental system to solve the deformation state. Though the relation between the intensities of stress and strain-increment vectors has a sufficient variety depending on the complicated history effect as recognized in the experimental results mentioned above, the range of variation with respect to the relation in the proportional deformation is not so remarkable in the deformation along the trajectories with mild values of geometric parameters, which may be expected in most of engineering practice.

Therefore, the constitutive equation is simplified so that the deformation analysis may be performed without appreciable complexity, if the relation in the proportional deformation is used as that between the intensities of stress and strain-increment vectors for the deformations along the trajectories of mild value of geometric parameter, even when the complicated history effect is reflected in the analysis. This conception is used in a new method of deformation analysis proposed recently by Lensky[30], which may be expected to be useful for the first step of accurate analysis of elasto-plastic deformation problems in engineering.

In the following, an accuracy of the stress-strain relation according to the hypothesis of local determinability will be estimated experimentally on the brass BsBM2 mentioned previously, for the case of orthogonal tri-linear trajectories in the space V_{2e} with two rounded corners[32], as shown in Fig. 7.26. In the experiment, values of pre-strain and strain rate are selected as $s_0=1.5\%$ and $ds/dt=3\times 10^{-6}$/sec, respectively. In the figure, five values of r are selected as $r=0.049$, 0.09, 0.19, 0.45 and 0.95 %. The length between the points P_1 and P_2 is selected so

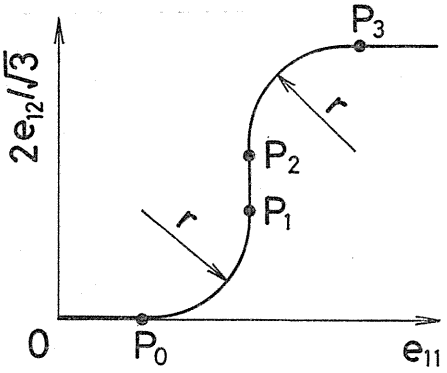

Fig. 7. 26 Orthogonal tri-linear strain trajectory with two rounded corners.

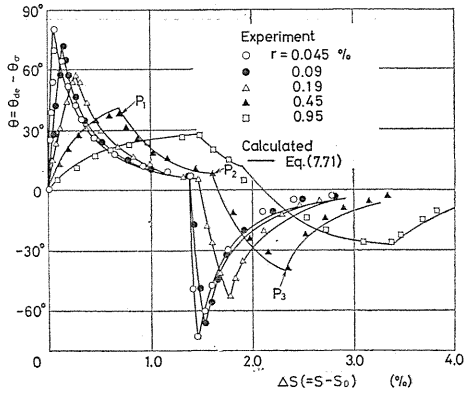

Fig. 7. 27 Relation between angle θ and the arc length Δs after the point P_0.

that the angle $\theta(=\theta_{de}-\theta_\sigma)$ at the point P_2 declines to less than 6° while the deformation develops during tht length, which means that the effect of deformation history obtained during the rounded corner P_0P_1 almost vanishes at the point P_2.

Figure. 7.27 shows the relation between θ and $\Delta s(=s-s_0)$ after the pnint P_0. As found in the figure, the angle θ increases after the start P_0 of the rounded corner, attains its maximum at the end point P_1 of the corner, and declines to tend to zero along the succeeding straight part. After the start P_2 of the second rounded corner, the angle θ decreases quickly to the end point P_3 of the second corner, and increases to tend to zero afterwards. In the figure, the experimental points corresponding to the points P_1, P_2 and P_3 are shown with the arrows, for the case of $r=0.45\%$(▲) as an example. The variation of angle θ after the point P_2 seems almost the same as that after the point P_0. This shows a weak dependence of the trend of variation in θ on the arc length s for $s\geq 1.5\%$.

Figures 7.28 through 7.32 show the stress components σ_{11}(●), $\sqrt{3}\sigma_{12}$(△) and their resultant value $|\sigma|$(○) after the point P_0 obtained by the experiment, in

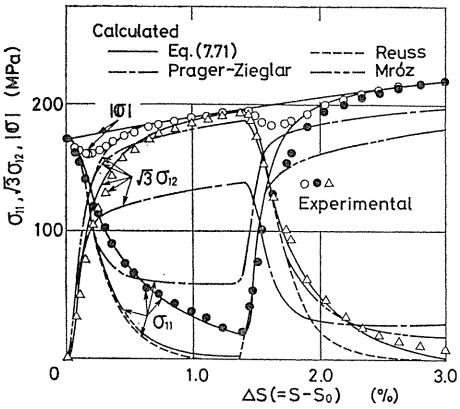

Fig. 7. 28 Variation of stress state along the trajectory ($r=0.045\%$).

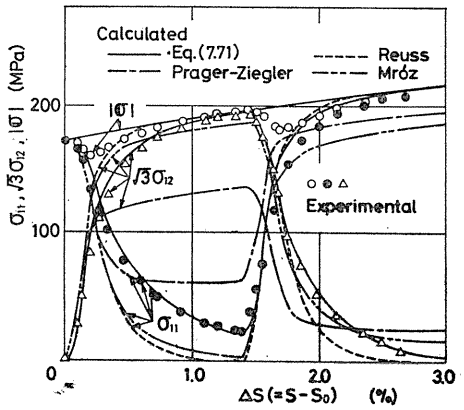

Fig. 7. 29 Variation of stress state along the trajectory ($r=0.09\%$)

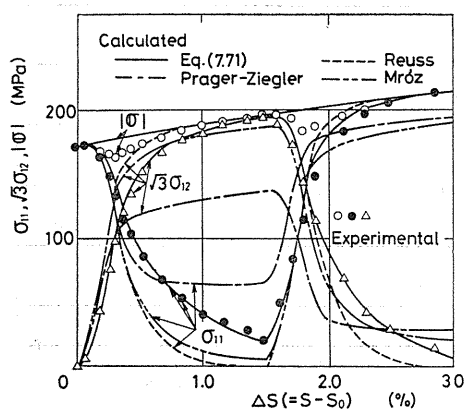

Fig. 7. 30 Variation of stress state alon the trajectory ($r=0.19\%$).

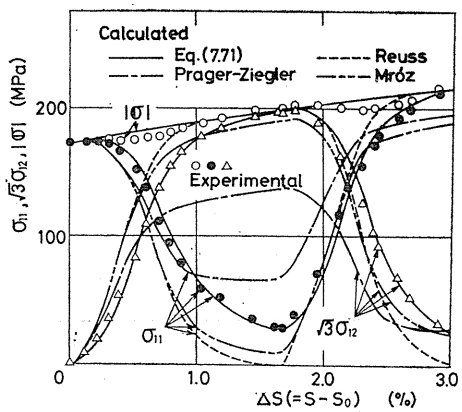

Fig. 7. 31 Variation of stress state along the trajectory ($r=0.45\%$).

relation to $\Delta s(=s-s_0)$ for the five values of r. As found in these figures, the magnitude $|\sigma|$ decreases just after the start of the rounded corner. This decrease almost disappears for $r>0.95\%$, while it is remarkable for small value of r(large curvature), as recognized in the experimental results in Section 6.4. For every value of r, the feature of decrease in $|\sigma|$ is almost the same for the first and second rounded corners having the same shapes. This trend is similar to that recognized in the experimental results for the orthogonal tri-linear trajectories in two dimensional space discussed in Section 6.5.1.

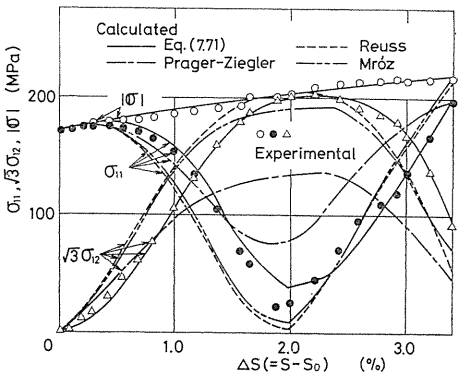

Fig. 7.32 Variation of stress state along the trajectory ($r=0.95\%$)

According to the weak dependence of the history effect on the arc length s for $s\geqq 1.5\%$, Eq. (7.67) may be simplified to

$$\frac{d\theta}{ds}=f(\theta)+\kappa(s), \tag{7.68}$$

where the function $f(\theta)$ showing the property of materials may be determined by the relation $d\theta/ds\sim\theta$ which is found from the curve $\theta\sim s$ obtained by experiment along the straight branch after the corner of orthogonal bi-linear strain trajectory. The relation $d\theta/ds\sim\theta$ obtained from the experimental results of brass BsBM2 along the second branch of orthogonal trajectory may be approximated by the following function.

$$f(\theta)=-2.78(\theta+0.14)^2, \tag{7.69}$$

from which the following epuation may be established.

$$\frac{d\theta}{ds}=-2.78(\theta+0.14)^2+\kappa(s). \tag{7.70}$$

Results of calculation by using Eq. (7.70) are eutered in Fig. 7.27 with the solid curves. As found in the figure, the solid curves approximate well the corresponding experimental ones. Thus, it may be said that Eq. (7.70) of the hypothesis of local determinability holds with a sufficiently high accuracy, together with the weak dependence of $d\theta/ds$ on the arc length s.

In the next, the magnitude of stress vector $|\sigma|$ as well as its components σ_{11} and $\sqrt{3}\sigma_{12}$ will be estimated with the use of the stress-strain relation under uniaxial tension. The latter relation for the brass BsBM2 obtained by experiment may be approximated with a sufficient accuracy by the following funciton.

$$\sigma=51.36\sqrt{\varepsilon}+106.7 \quad \text{(MPa)} \quad \text{for} \quad \varepsilon\geqq 1.0\%,$$

where σ and ε denote the stress and strain under tension. Thus the above mentioned values of $|\sigma|$, σ_{11} and $\sqrt{3}\sigma_{12}$ may be calculated by the following system.

$$\left.\begin{aligned} |\sigma| &= 51.36\sqrt{s}+106.7 \quad \text{(MPa)} \quad \text{for} \quad s \geq 1.0\,\%, \\ \frac{d\theta}{ds} &= -2.78(\theta+0.14)^2+\kappa(s). \end{aligned}\right\} \tag{7.71}$$

Results of calculation by using Eq. (7.71) are entered in Figs. 7.28 through 7.32 with the solid curves. In these figures, results of calculations by using the Prandtl-Reuss' incremental theory, the Prager-Zieglar's kinematic hardening theory[2] and the Mróz's theory[33] are entered also with the dashed, the dot-dash and the double-dot-dash curves, respectively, for comparison.

As found in these figures, it is said that the results of calculation using Eq. (7.71) may approximate the results of experiment with higher accuracy than that using any of the other three kinds of the existing theory, in reflecting well the trend in the experimental results.

Chapter VIII Conclusion

In order to perform precisely the inelastic deformation analysis of engineering structure or the theoretical analysis of plastic working, it is necessary to use the constitutive equation of materials in which the effect of deformation history is reflected with high accuracy in their deformation behaviour. Since mathematical difficulties have been eliminated with the appearance of electronic computer, and since the precise experiment of complex deformation under combined loadings becomes to be possible with the advance in testing apparatus with automatic control systems, present attentions are concentrated mainly to improve the constitutive equation in taking the history effects of complicated inelastic deformation on the deformation behaviour into account. Under such a back-ground, investigations are performing actively to formulate the inelastic deformation behaviour under complicated loading in taking account of the effect of deformation history.

In our laboratory, the above-mentioned investigation has been continued more than ten years at room temperature and elevated tempearature as well with the use of the corresponding automatic combined loading testing machines. The present paper reviews fundamental results of our investigations concerning the inelastic deformation behaviours of metals at room temperature.

Our experiments could be performed with high accuracy owing to the recent improvement in the performance and precision of testing apparatus so that a kind of phenomenon which had been regarded as a random scatter in experimental results could be arranged systematically. Furthermore, some effects in the response of combined deformation, which cannot be expected from simple combination of elemental deformation processes, could be discussed systematically.

According to the experimental results together with the theoretical foundation in continuum mechanics, a kind of stress-strain relation was formulated in a form of tensorial equation, which has a generality for a fixed sequence in deformation history. The history effects due to complex deformations having infinite varieties, however, are very difficult to be formulated systematically in a simple form. Though the history effects apparently have infinite varieties, the material response to disturbance should be due to the change in microstructure. Thus, a light would be thrown on the systematization of infinite varieties if the response of polycry-

stalline structure to the disturbance would be clarified.

In this kind of investigation, a method has been proposed in which the history effect is analysed as evolutions in the internal state variables, which are parameters representing in global the behaviour of microstructure of materials. As an example of application of this method, another kind of stress-strain relation was formulated according to the experimental results with the use of intrinsic time measure, which may be regarded as a kind of state variable. Two kinds of stress-strain relation formulated above have fairly complicated forms, whereas they reproduce with high accuracy the experimental results.

On the other hand, it was clarified by the experimental results that the hyporhesis of local determinability enables us to secure the trend of complicated history offects on the inelastic deformation behaviour with a simple conception. A formulation of the relations between the corresponding components of stress and strain-increment according to this hypothesis seems to have fairly simple forms.

References

1) Prager, W., Proc. Inst. Mech. Engrs., Vol. 169(1955), p. 41.
2) Ziegler, H., Quart. Appl. Mech., Vol. 17(1959), p. 55.
3) Baltov, A. and Sawczuk, A., Acta Mech., Vol. 1(1965), p.81.
4) Mrós, Z., J. Mech. Phys. Solids, Vol. 15(1967), p. 163.
5) Backhaus, G., Zeit. angew. Math. Mech., Vol. 48(1968), p. 99.
6) Eisenberg, A. A. and Phillips, A., Acta Mech., Vol. 5(1969), p. 1.
7) Williams, J. F. and Svenson, N. L., J. Strain Analysis, Vol. 5(1970), p. 128.
8) Truesdell, C. and Noll, W., The Non-Linear Field Theory of Mechanics(1965), Encyclopedia of Physics, Vol. Ⅲ/3.
9) Ильюшин, А. А., Прикладная математика и мехамика, том 18(1954), с. 641; Вопросы Теории Пластичности, Изд. АН СССР(1961), с. 1; Пластичность, основы общей математической теории, Изд. АН СССР(1963).
10) Lensky, V. S., Plasticity, Proc. 2nd Symp. Naval Struc. Mech., Pergamon Press(1960), p. 259.
11) Ивлев, Д. Д., Изв. АН СССР, ОТН, мех. и машиностр., том 2(1960).
12) Новожилов, В. В., Изв. АН СССР, ОТИ, мех. и машиностр., том 3(1961).
13) Kratochvil, J. and Dillon, O. W. Jr., J. Appl. Phys., Vol. 41, No. 1(1970), p. 1470.
14) Tokuda, M. et al., Paper Presented at 15th IUTAM Congress at Toronto(1980); Bulletine of the JSME, Vol. 25, No. 208(1982).
15) Ohashi, Y. and Tokuda, M., J. Mech. Phys. Solids, Vol. 21(1973), p. 241.
16) Ohashi, Y. et al., J. Mech. Phys. Solids, Vol. 23(1975), p. 295.
17) Ohashi, Y. et al., Trans. JSME, Vol. 43, No. 374(1977), p. 3732 (in Japanese).
18) Ohashi, Y. et al., Trans. ASME, J. Eng. Mat. Tech., Vol. 98(1976), p. 282.
19) Ohashi, Y. et al., J. Mech. Phys. Solids, Vol. 25(1977), p. 385.
20) Вакуленко, А.А., Исследования по упругости и пластичности, Изд. Ленингрдский Университета, том 8(1971), с. 3.
21) Качанов, Л. М., Основы теории пластичности. Изд. "Наука" (1969), москва.
22) Ohashi, Y. et al., Bulletin de l'Academie Polonaise des Science, ser. sci. tech., Vol. XXVI, No.5 (1976), p. 261.
23) Ohashi Y. and Kawashima, K., J. Mech. Phys. Solids, Vol. 25(1977), p. 409.
24) Ohashi, Y. et al., J. Mech. Phys. Solids, Vol. 29, No. 1(1981), 69.
25) Ohashi, Y. et al., Bulletion of the JSME, Vol. 23, No. 182(1980), p. 1305.

26) Ohashi, Y. and Tanaka, E., Paper presented at 15th IUTAM Congress at Toronto (1980).; Trans. ASME, J. Eng. Mat. Tech., Vol. 103, No. 3(1981), p. 287.
27) Valanis, K. C., Arch. Mech., Vol. 23, No. 4(1971), p. 517.
28) Ohashi, Y. et al., Arch. Mech., Vol. 32, No. 1(1980), p. 125.
29) Ленский, В. С., Изв. АН СССР, ОТН, мех. и машиностр., том 5(1962), с. 154.
30) Ленский, В. С., Вестн. москв. унверситета, сер. 1, математика, механика, No. 6(1979), с. 92.
31) Ohashi, Y. et al., J. Mech. Phys. Solids, Vol. 29, No. 1(1981), p. 51.
32) Tokuda, M. et al., Trans. JSME. Vol. 49, No. 437-A(1983), (in Japanese, to be published),
33) Mróz, Z., Acta Mech. 7(1969), p. 199.